

AERO-STRUCTURAL DESIGN AND ANALYSIS OF A JOINED-WING KIT

A THESIS SUBMITTED TO
THE GRADUATE SCHOOL OF NATURAL AND APPLIED SCIENCES
OF
MIDDLE EAST TECHNICAL UNIVERSITY

BY

BERKAN ALANBAY

IN PARTIAL FULFILLMENT OF THE REQUIREMENTS
FOR
THE DEGREE OF MASTER OF SCIENCE
IN
AEROSPACE ENGINEERING

DECEMBER 2015

Approval of the thesis:

**AERO-STRUCTURAL DESIGN AND ANALYSIS OF
A JOINED-WING KIT**

Submitted by **BERKAN ALANBAY** in partial fulfillment of the requirements for the degree of **Master of Science in Aerospace Engineering Department, Middle East Technical University** by,

Prof. Dr. Gülbin Dural Ünver
Dean, Graduate School of **Natural and Applied Sciences**

Prof. Dr. Ozan Tekinalp
Head of Department, **Aerospace Engineering**

Assoc. Prof. Dr. Melin Şahin
Supervisor, **Aerospace Engineering Dept., METU**

Examining Committee Members:

Prof. Dr. Yavuz Yaman
Aerospace Engineering Dept., METU

Assoc. Prof. Dr. Melin Şahin
Aerospace Engineering Dept., METU

Prof. Dr. Serkan Özgen
Aerospace Engineering Dept., METU

Assist. Prof. Dr. Ercan Gürses
Aerospace Engineering Dept., METU

Assoc. Prof. Dr. Erdem Acar
Mechanical Engineering Dept., TOBB ETU

Date: 01.12.2015

I hereby declare that all information in this document has been obtained and presented in accordance with academic rules and ethical conduct. I also declare that, as required by these rules and conduct, I have full cited and referenced all material and results that are not original to this work.

Name, Last Name: Berkan, Alanbay

Signature :

ABSTRACT

AERO-STRUCTURAL DESIGN AND ANALYSIS OF A JOINED-WING KIT

Alanbay, Berkan

M.Sc., Department of Aerospace Engineering

Supervisor: Assoc. Prof. Dr. Melin Şahin

December 2015, 147 pages

In this study, a multi-objective aero-structural multidisciplinary design optimization (MDO) of a joined-wing kit which is installed on a transonic free fall munition is performed. The main purpose of the joined-wing kit is to enable the munitions to extend their range and gain standoff attack capability. In order to fulfill these aims joined-wing kit configurations are generally investigated through various analyses. Each joined-wing configurations are determined through two geometric key parameters namely; the aft wing sweep angle and the location of the joint.

In the first part of the thesis, dynamic characteristics of the joined-wing configurations are investigated through series of finite element modelling and analyses. Thereafter, experimental validations of these finite element models are performed by classical modal analyses techniques comprising both impact hammer and shaker tests.

The second part of the thesis focuses on the high-fidelity multi-point aero-structural optimizations of the joined-wing configurations. In addition to the geometric design parameters, the effects of two aerodynamic design variables; namely speed and the angle of attack of the munition are also explored. The objectives of the optimization can be listed as maximizing lift-to-drag ratio, minimizing weight of the joined-wing

kit and increasing wing stiffness. For these purposes, loosely coupled MDO analyses are elucidated with a hybrid genetic algorithm and response surface methodology (RSM). In consideration of the 3D aerodynamic analyses, RANS (Reynold Averaged Navier Stokes) simulations with Spalart-Allmaras model are used for turbulence closure. Then, the structural analyses are performed under various the aerodynamic loads. In order to construct accurate response surfaces, both aerodynamic and structural analyses are repeated for required number of experimental design points which are chosen through design of experiments. Finally, candidate design points for the best design are extracted from the response surface models by using multi-objective genetic algorithms.

Keywords: Joined-wing, Multidisciplinary Design Optimization, Finite Element Modelling and Analysis, Aerodynamic Analysis, Modal Analysis and Testing, Design of Experiments, Response Surfaces, Genetic Algorithm

ÖZ

BİRLEŞİK KANAT KİTİNİN AERODİNAMİK-YAPISAL TASARIM VE ANALİZİ

Alanbay, Berkan

Yüksek Lisans, Havacılık ve Uzay Mühendisliği Bölümü

Tez Yöneticisi: Doç. Dr. Melin Şahin

Aralık 2015, 147 sayfa

Bu çalışmada transonik hızda itkisiz hareket eden bir mühimmata takılan birleşik kanat kitinin çok amaçlı multidisipliner optimizasyonu (MDO) yapılmıştır. Mühimmatlara birleşik kanat kiti takılmasının ana amacı, mühimmatların menzili artırmak ve emniyet mesafesinden atış olanağı sağlamaktır. Bu amaçları sağlayabilmek için birleşik kanat kiti konfigürasyonları çeşitli analizlere tabi tutulmuştur. Herbir birleşik kanat kiti konfigürasyonu iki önemli geometrik parametre olan arka kanat süpürme açısı ve bağlantı yeri ile belirlenmiştir.

Tezin ilk bölümünde, birleşik kanat kiti konfigürasyonlarının dinamik karakteristikleri bir dizi sonlu elemanlar modelleme ve analiz yöntemleri ile incelenmiştir. Bunu takiben, sonlu elemanlar modellerinin deneysel doğrulamaları için darbe çekici ve modal titreştirici uygulamalarını içeren klasik modal analiz testleri yapılmıştır.

Tezin ikinci bölümü birleşik kanat konfigürasyonlarının yüksek doğruluk dereceli, birden fazla uçuş koşulunu içeren aerodinamik-yapısal optimizasyonu üzerine yoğunlaşmıştır. Geometrik tasarım parametrelerine ek olarak, iki aerodinamik tasarım parametresi; mühimmatın hızı ve hücum açısının etkileri de incelenmiştir. Optimizasyonun amaçları, taşıma kuvvetinin sürüklenme kuvvetine olan oranını en üst düzeye çıkartılması, birleşik kanat kitinin ağırlığının en aza indirgenilmesi ve kanat direngenliğinin artırılması olarak sıralanabilir. Bu amaçlarla yönelik olarak, melez

genetik algoritma ve yanıt yüzey metodolojisi (RSM) kullanılarak ayırık MDO analizleri yapılmıştır. Üç boyutlu aerodinamik analizleri gerçekleştirirken, türbulans modellemesi için Spalart-Allmaras modeli ile RANS (Reynold Ortalamalı Navier Stokes) simülasyonları kullanılmıştır. Daha sonra yapısal analizler farklı aerodinamik yükler altında de tekrarlanmıştır. Hassas yanıt yüzeyleri oluşturabilmek için gerekli sayıda deneysel tasarım noktası deneysel tasarım yöntemleriyle seçilmiş, her bir seçilen nokta için aerodinamik ve yapısal analizler yapılmıştır. Son olarak en iyi tasarım için aday tasarım noktaları oluşturulan yanıt yüzeylerin çok amaçlı genetik algoritma aracılığıyla tespit edilmiştir.

Anahtar Kelimeler: Birleşik kanat, Multidisipliner Tasarım Optimizasyonu, Sonlu Elemanlar Modelleme ve Analizi, Modal Analiz ve Testi, Deneysel Tasarım, Yanıt Yüzeyleri, Genetik Algoritma

To My Family

ACKNOWLEDGEMENTS

The author would like to express his deepest gratitude to his thesis supervisor Assoc. Prof. Dr. Melin Şahin for his valuable advice, guidance, encouragement and wisdom throughout this challenging process.

The author has to express his appreciation to his examining committee members: Prof. Dr. Yavuz Yaman, Prof. Dr. Serkan Özgen, Assist. Prof. Dr. Ercan Gürses and Assoc. Prof. Dr. Erdem Acar for their invaluable suggestions and supportive criticism.

The author would like to give special thanks to Mr. İlke Aydıncağ for his suggestions, comments and guidance throughout the thesis.

The author also would like to thank to Mr. Yusuf Eldoğan for his valuable and beneficial support during the study.

The author wished to express his sincere appreciation to his colleague Dr. Güvenç Canbaloğlu for his assistance throughout the experimental modal analyses part.

The author would like to thank to Mr. Argün Katırcı, Dr. Bedri Yağız, Mr. Arif Cem Gözükara, Mr. Abdullah Emre Çetiner from aerodynamic design team of ASELSAN Inc. for their efforts and helpful criticism throughout the research.

The author also would like to thank to his managers Dr. İhsan Özsoy, Mr. Sabri Çetin, and Mr. Rafet Eroğlu for giving him the opportunity to use the computational and testing capabilities in ASELSAN.

Finally, the author wishes to offer his deepest thanks to his parents and brother for all of their emotional support.

TABLE OF CONTENTS

ABSTRACT.....	v
ÖZ.....	vii
ACKNOWLEDGEMENTS.....	x
TABLE OF CONTENTS.....	xi
LIST OF TABLES.....	xv
LIST OF FIGURES.....	xvii
CHAPTERS	
1 INTRODUCTION.....	1
1.1 Overview and Motivation of the Study.....	1
1.2 Objectives of the Study.....	2
1.3 Limitations of the Study.....	3
1.4 Outline of the Thesis.....	3
2 LITERATURE REVIEW.....	5
2.1 Introduction.....	5
2.2 The Joined Wing Concepts.....	5
2.3 Multidisciplinary Design Optimization Aspects.....	6
2.4 Multidisciplinary Design Optimization Architectures.....	9
2.5 Discussion and Conclusions.....	12
3 RESEARCH PROBLEM.....	15

3.1	Introduction.....	15
3.2	Structural Loads on the Joined-Wing Configurations	15
3.3	Variables for the Joined-Wing Configurations.....	17
3.4	Analyses and Experimental Tools	19
3.5	Discussion and Conclusions	21
4	FINITE ELEMENT MODELLING AND ANALYSES OF JOINED-WING CONFIGURATIONS.....	23
4.1	Introduction.....	23
4.2	Finite Element Modelling of the Selected Joined-Wing Configurations.....	23
4.3	Modal Analyses of the Selected Joined-Wing Configurations.....	28
4.4	Discussion and Conclusions	31
5	EXPERIMENTAL VALIDATION OF THE JOINED-WING CONFIGURATIONS.....	33
5.1	Introduction.....	33
5.2	Virtual Test on the Selected Joined-Wing Configurations	34
5.2.1	Optimum Driving Point (ODP) Technique	34
5.2.2	Non-optimum Driving Point (NODP) Technique	35
5.3	Modal Test Setup and Configurations	37
5.3.1	Test Instrumentation.....	38
5.4	Modal Tests of the Selected Joined-Wing Configurations	40
5.4.1	Impact Hammer Test.....	41
5.4.2	Shaker Tests with Random Excitation	51
5.5	Discussion and Conclusions	58

6	3-D AERODYNAMIC MODELLING AND ANALYSES OF THE JOINED-WING CONFIGURATIONS.....	59
6.1	Introduction	59
6.2	3-D CFD Analysis of Selected Joined-Wing Configurations	60
6.2.1	Mesh Generation	60
6.2.2	Fluent Setup	64
6.2.3	Convergence Monitoring	65
6.3	Analysis Results	65
6.4	Discussion and Conclusions.....	69
7	AERO-STRUCTURAL ANALYSES OF THE JOINED-WING CONFIGURATIONS	71
7.1	Introduction	71
7.2	Finite Element Analyses of the Joined-Wing Configurations under Aerodynamic Loads	71
7.3	Discussion and Conclusions.....	77
8	MULTIDISCIPLINARY DESIGN OPTIMIZATION OF THE JOINED-WING CONFIGURATIONS	79
8.1	Introduction	79
8.2	Optimization Problem Formulation	81
8.2.1	Design Variables and Operating Conditions.....	81
8.2.2	Objective Function.....	82
8.2.3	Standard Formulation.....	84
8.3	Design of Experiments	86

8.3.1	Design of Experiment Types	87
8.4	Response Surface (RS) Methodology	89
8.4.1	Response Surface Types	90
8.5	Accuracy Assessments of Response Surfaces	92
8.5.1	Comparisons of Different DOE Types	95
8.5.2	Comparisons of Different RS Methods	95
8.6	Response Surface Results	98
8.7	Response Methodology for Dynamic Characteristics of the Joined-Wing	108
8.8	Application of a Genetic Algorithm	113
8.9	Optimization Results for the Joined-Wing Configurations	115
8.10	Discussion and Conclusions	117
9	CONCLUSIONS	119
9.1	General Conclusions	119
9.2	Recommendations for Future Work	120
	REFERENCES	121
	APPENDICES	
	APPENDIX A	125
	APPENDIX B	127
	APPENDIX C	133
	APPENDIX D	137
	APPENDIX E	145
	APPENDIX F	147

LIST OF TABLES

TABLES

Table 1.1. Some of the today's smart munitions	1
Table 3.1. Definition of design parameters and variables of the joined-wing.....	18
Table 3.2. Upper and lower bounds	18
Table 4.1 Natural frequencies of the joined-wing for Design Point 1 and their descriptions	29
Table 4.2. Natural frequencies of the joined-wing for Design Point 2 and their descriptions	30
Table 5.1. Instrumentation and software information.....	38
Table 5.2. The first six vibration modes of the Design Point 1 from impact hammer test.....	46
Table 5.3. Comparison of FEA and impact hammer test results for the Design Point 1	47
Table 5.4. First six vibration modes of the Design Point 2 from impact hammer test	50
Table 5.5. Comparison of FEA and impact hammer test results for the Design Point 2	51
Table 5.6. First six vibration modes of the Design Point 1 from shaker test.....	54
Table 5.7. Comparison of FEA and shaker test results for the Design Point 1	55
Table 5.8. First six vibration modes of the Design Point 2 from shaker test.....	57
Table 5.9. Comparison of FEA and shaker test results for the Design Point 2	58
Table 6.1. Boundary conditions	64
Table 8.1. Operating conditions.....	81
Table 8.2. Input design variables	81
Table 8.3. Guideline for design selection [50].....	86
Table 8.4. Accuracy of response surfaces based on DOE types.....	95
Table 8.5. Accuracy of response surfaces created by different RS modelling types.	96
Table 8.6. Accuracy of response surfaces created by different RS modelling types.	96

Table 8.7. Accuracy of response surfaces created by different RS modelling types .	97
Table 8.8. DOE- LHS points for modal analyses	109
Table 8.9. Goodness of fit of natural frequency RS for verification points	110
Table 8.10. Description of the free vibration modes	110
Table 8.11. MOGA analysis scheme	114
Table 8.12. MOGA results for 1g load condition.....	114
Table 8.13. MOGA results for 2.5 g load condition.....	115

LIST OF FIGURES

FIGURES

Figure 1.1. Pictorial illustrations of some of the today's smart munitions	2
Figure 2.1. Pictorial illustrations of joined-wing configurations [3]	6
Figure 2.2. Varying levels of fidelity in modelling for fluids and structure [5]	8
Figure 2.3. A framework for automatic implementation of MDO architectures [24]	12
Figure 3.1. Typical mission profile of the munition	16
Figure 3.2. Velocity-Load diagram of the munition	16
Figure 3.3. Munition rack unit (dimensions in mm)	17
Figure 3.4. Design parameters and variables of the joined-wing	18
Figure 3.5. Pictorial illustrations of upper and lower bounds	19
Figure 3.6. Flowchart for MDO process	20
Figure 4.1. Isometric view of the joined-wing geometry.....	24
Figure 4.2. Exploded view of joined-wing geometry	24
Figure 4.3. General dimensions of joined-wing assembly [mm].....	25
Figure 4.4. General dimensions of the front wing [mm]	25
Figure 4.5. General dimensions of the aft wing [mm].....	26
Figure 4.6. Body to body contact types of the joined-wing connections.....	27
Figure 4.7. Fixed boundary condition of joined-wing	27
Figure 4.8. Mesh of the sample joined-wing geometry	28
Figure 4.9. Corresponding mode shapes of the of joined-wing for Design Point 1 ..	29
Figure 4.10. Corresponding mode shapes of the of joined-wing for Design Point 2	30
Figure 5.1. ODP of the Design Point 1	35
Figure 5.2. ODP of the Design Point 2	35
Figure 5.3. NODP of the Design Point 1	36
Figure 5.4. NODP of the Design Point 2	36
Figure 5.5. Test setup for modal analysis of the Design Point 1	37
Figure 5.6. Impact hammer [29]	38
Figure 5.7. Triaxial accelerometer [29]	39

Figure 5.8. Data acquisition system [30].....	39
Figure 5.9. Power amplifier [31].....	40
Figure 5.10. Sample screen of PULSE Labshop	41
Figure 5.11. Measurement mesh of the Design Point 1	42
Figure 5.12. Test setup for the Design Point 1	43
Figure 5.13. Impact excitation and measurement points of the Design Point 1	43
Figure 5.14. FRF plots of impact hammer test for the Design Point 1	44
Figure 5.15. Sample stability diagram for the first two modes of impact hammer test for the Design Point 1 with zoom view	45
Figure 5.16. The first four mode shapes of the Design Point 1 from impact hammer test	46
Figure 5.17. Measurement mesh of the Design Point 2	48
Figure 5.18. Impact excitation and measurement points of the Design Point 2.....	48
Figure 5.19. Test setup for impact hammer test of the Design Point 2	49
Figure 5.20. FRF plots of the impact hammer test for the Design Point 2.....	49
Figure 5.21. The first six mode shapes of the Design Point 2 from impact hammer test	50
Figure 5.22. Shaker excitation and measurement points of the Design Point 1	52
Figure 5.23. Test setup for shaker test of the Design Point 1	53
Figure 5.24. FRF plots of the shaker test for the Design Point 1	53
Figure 5.25. The first six mode shapes of the Design Point 1 from shaker test.....	54
Figure 5.26. Shaker excitation and measurement points of the Design Point 2.....	55
Figure 5.27. Test setup for shaker test of the Design Point 2.....	56
Figure 5.28. FRF plots of the shaker test for the Design Point 2	56
Figure 5.29. The first six mode shapes of the Design Point 2 from shaker test.....	57
Figure 6.1. Surface meshes on joined-wing surfaces and symmetry plane (a) Design Point 1 (b) Design Point 2	61
Figure 6.2. Detailed mesh view around wing cross-sections (a) Design Point 1 (b) Design Point 2	62
Figure 6.3. Inflation layers around front wing	63
Figure 6.4. Typical mesh for fluid domain.....	63

Figure 6.5. Change of scaled residuals vs. iteration number for pressure based solver	65
Figure 6.6. Upper surface static pressure contours of the Design Point 1 [Pa]	66
Figure 6.7. Lower surface static pressure contours of the Design Point 1 [Pa]	66
Figure 6.8. Upper surface static pressure contours of the Design Point 2 [Pa]	67
Figure 6.9. Lower surface static pressure contours of the Design Point 2 [Pa]	67
Figure 6.10. Symmetry surface path lines for the Design Point 1	68
Figure 6.11. Symmetry surface path lines for the Design Point 2	69
Figure 7.1. Structural mesh of the Design Point 1	72
Figure 7.2. Structural mesh of the Design Point 2	72
Figure 7.3. The transferred static pressure distribution in ANSYS® Mechanical for the Design Point 1	73
Figure 7.4. The transferred static pressure distribution in ANSYS® Mechanical for Design Point 2	73
Figure 7.5. Displacement of the Design Point 1 [mm]	74
Figure 7.6. Displacement of the Design Point 2 [mm]	74
Figure 7.7. Equivalent stress distribution of the Design Point 1 [Pa]	75
Figure 7.8. Zoomed view of the equivalent stress distribution of the Design Point 1 on the defined plane [Pa]	76
Figure 7.9. Equivalent stress distribution of the Design Point 2 [Pa]	76
Figure 7.10. Zoomed view of the equivalent stress distribution of the Design Point 2 on the defined plane [Pa]	77
Figure 8.1. The framework of the ANSYS® Design Exploration	79
Figure 8.2. Gliding platform illustration	83
Figure 8.3. Face centered central composite designs (FCCCD) of three factors [45]	87
Figure 8.4. Box-Behnken designs (BBD) of three factors [45]	88
Figure 8.5. LHS designs for two factors [45]	88
Figure 8.6. Optimum space filling designs for two factors [45]	89
Figure 8.7. NN architecture [45]	91
Figure 8.8. Summary of response surface optimization process	97

Figure 8.9. Total lift [N] response as a function of joint location and aft wing sweep angle (AOA: 0°, Mach: 0.7)	98
Figure 8.10. 2D slice response chart for total lift [N] as a function of joint location and aft wing sweep angle (AOA: 0°, Mach: 0.7)	99
Figure 8.11. Total lift [N] response as a function of Mach number and AOA (joint location: 350 mm, aft wing sweep angle: 0°)	99
Figure 8.12. Total drag [N] response as a function of joint location and aft wing sweep angle (AOA: 0°, Mach: 0.7)	100
Figure 8.13. 2D slice response chart for total drag [N] as a function of joint location and aft wing sweep angle (AOA: 0°, Mach: 0.7)	101
Figure 8.14. Total drag [N] response as a function of Mach number and AOA (joint location: 350 mm, aft wing sweep angle: 0°)	101
Figure 8.15. L/D response as a function of joint location and aft wing sweep angle (AOA: 0°, Mach: 0.7)	102
Figure 8.16. 2D slice response chart for L/D as a function of joint location and aft wing sweep angle (AOA: 0°, Mach: 0.7)	103
Figure 8.17. L/D response as a function of Mach number and AOA (joint location: 350 mm, aft wing sweep angle: 0°)	103
Figure 8.18. Tip deflection [mm] response as a function of joint location and aft wing sweep angle (AOA: 0°, Mach: 0.7)	104
Figure 8.19. 2D slice response chart for Tip Deflection as a function of joint location and aft wing sweep angle (AOA: 0°, Mach: 0.7)	105
Figure 8.20. Tip deflection [mm] response as a function of Mach number and AOA (joint location: 350 mm, aft wing sweep angle: 0°).....	105
Figure 8.21. Maximum equivalent stress [MPa] response as a function of joint location and aft wing sweep angle (AOA: 0°, Mach: 0.7).....	106
Figure 8.22. 2D slice response chart for Maximum Equivalent Stress as a function of joint location and aft wing sweep angle (AOA: 0°, Mach: 0.7)	107
Figure 8.23. Maximum equivalent stress [MPa] response as a function of Mach number and AOA (joint location: 350 mm, aft wing sweep angle: 0°).....	107
Figure 8.24. Mass of the joined-wing [kg] response as a function of joint location and aft wing sweep angle	108

Figure 8.25 Natural frequency responses corresponding to Mode 1 as a function of joint location and aft wing sweep angle.....	111
Figure 8.26. Natural frequency responses corresponding to Mode 2 as a function of joint location and aft wing sweep angle.....	111
Figure 8.27. Natural frequency responses corresponding to Mode 3 as a function of joint location and aft wing sweep angle.....	112
Figure 8.28. Natural frequency responses corresponding to Mode 4 as a function of joint location and aft wing sweep angle.....	113
Figure 8.29. Local sensitivity for MDO of joined-wing.....	116
Figure 8.30. Local sensitivity graph for the mode shapes of the joined-wings	116

CHAPTER 1

INTRODUCTION

1.1 Overview and Motivation of the Study

Ever since the dawn of military aviation, mankind seeks a way to strike their enemy from the air. Many variety of air vehicles have been designed in order to carry munitions. However, since the evolution of the smart munitions, the aircrafts have been falling from the popular esteem by considering their effective role in the war. As most of the today's aircrafts are capable of carrying a munition, once the munition released from the aircraft, the munition must hit the target. For this purpose, the wing kit is one of the essential part of the smart munitions. They enable munitions to gain standoff attack capability and extend their range. Some of the todays munitions are summarized and their pictorial presentations are shown in Table 1 and Figure 1 respectively.

Table 1.1. Some of the today's smart munitions

Weapon Name	Developer	Length (cm)	Diameter (mm)	Warhead	Total Weight
SDB-I	Boeing	180	190	-	93 kg
SDB-II	Raytheon	176	180	-	93 kg
JSOW	Raytheon	410	330	BLU-97/B BLU-108	483 to 497 kg
Long Shot	Lockheed Martin	Up to 233		MK-82 GBU-87 GBU-12	227 to 454 kg
SSW	Lockheed Martin	53	108	-	16 kg
KGK	Tübitak SAGE	Up to 222	275 355	MK-82 MK-83	227 kg
FT-2	CASC	300	377	-	500 kg
FT-4	CASC	-	-	-	250 kg



Figure 1.1. Pictorial illustrations of some of the today's smart munitions

With the developing technology, lots of wing concepts have been proposed. Among them, one of the most promising concept is the joined-wing concept. The joined-wing concept has been studied by many researchers early 1980's and some potential advantages have been highlighted as light weight, high stiffness and aerodynamic efficiency. Due to these potential advantages joined wing concept is also used in this study. To make these advantages more superior as much as possible, multidisciplinary design optimization is performed over it by considering both aerodynamic and structural parts separately. Experimental modal analyses are also implemented for the selected joined-wing configurations in order to validate finite element model.

1.2 Objectives of the Study

The objectives of this study can be listed as follows:

- Constructing high fidelity finite element models (FEM) of the joined-wing configurations.
- Performing experimental validations of the selected FEMs of the joined-wing configurations through experimental modal analysis.

- Conducting high fidelity 3D Computational Fluid Dynamic (CFD) analysis in order to have a better estimate in drag at different flight conditions and under aerodynamic loading.
- Performing multidisciplinary design optimization of joined-wing configurations to obtain the best possible configuration considering both aerodynamic and structural design aspects.

1.3 Limitations of the Study

The major limitations of this study can be listed as follows:

- Due to the production cost of the test prototypes, limited numbers of joined wing configurations were manufactured.
- Even though loosely coupled MDO analyses were performed, it took over a month with 2 separate workstations, each one has 32 Core and 64 GB RAM, for the simulations. In order to include aeroelastic effects, much more computational source is needed.
- Buckling is not considered throughout this study.
- The aeroelastic effects are also ignored.

1.4 Outline of the Thesis

The organization of the thesis is summarized below:

In Chapter 2, the literature survey about joined wings and multidisciplinary design aspects are given briefly. The advanced design methodologies for designing wing systems are also presented.

In Chapter 3, the design problem which includes design geometry and its design parameters, flight conditions, aerodynamic loads and the analyses tools is defined to provide better understanding on the research subject.

In Chapter 4, finite element models of the joined-wing configurations are constructed for modal analyses. The performed modal analyses are explained via two selected joined-wing configurations. These modal analyses are performed in order to obtain the vibration characteristics of the joined-wing configurations.

Chapter 5 provides the modal testing of the selected joined-wing configurations performed for the validation of the finite element models.

In Chapter 6, aerodynamic analyses are performed to calculate aerodynamic loads. Furthermore, the total drag (D) and the total lift (L) values and their ratio (L/D) are obtained and stored as aerodynamic output values in order to implement their optimizations by considering speed (i.e. Mach), angle of attack (AOA), joint location and aft wing sweep angle as input design variables to achieve range extension and maneuverability improvement at critical flight conditions in Chapter 8.

In Chapter 7, the calculated aerodynamic loads mapped into structural mesh and then structural analyses are performed.

In Chapter 8, multidisciplinary design optimization of the joined-wing configurations is performed. Design of experiment and surrogate modelling techniques are also introduced and the best candidate points for design objectives are criticized and validated.

In Chapter 9, the general conclusions and discussions are presented and the recommendations for future works are provided.

CHAPTER 2

LITERATURE REVIEW

2.1 Introduction

Today, in the aero-structural design, in addition to conceptual, preliminary and detailed design steps, multidisciplinary design optimization is becoming one of the primary part of aerodynamic design process. This chapter reviews past researches conducted on the design of the wings, their multidisciplinary analysis and the optimization processes.

2.2 The Joined Wing Concepts

The joined-wing is an innovative concept which may be defined as a wing system that incorporates tandem wings arranged to form diamond shape in both top and front views. The joined-wing is also commonly called as “Bi-diamond” and “Box-wing”. Pictorial illustrations of joined-wing configurations can be seen at Figure 2. The joined-wing is a well-known subject dated back to 1980s by the studies of Wolkovitch [1, 2]. Wolkovitch claims some of the advantages of the joined wings as light weight, high stiffness, low induced drag and good transonic area distribution. However, the advantages of joined-wings are not invariably outstanding than the conventional ones. In order to have superior advantages, the geometric parameters of the joined-wing such as sweep, dihedral, taper ratio and location of the joint should be chosen properly.

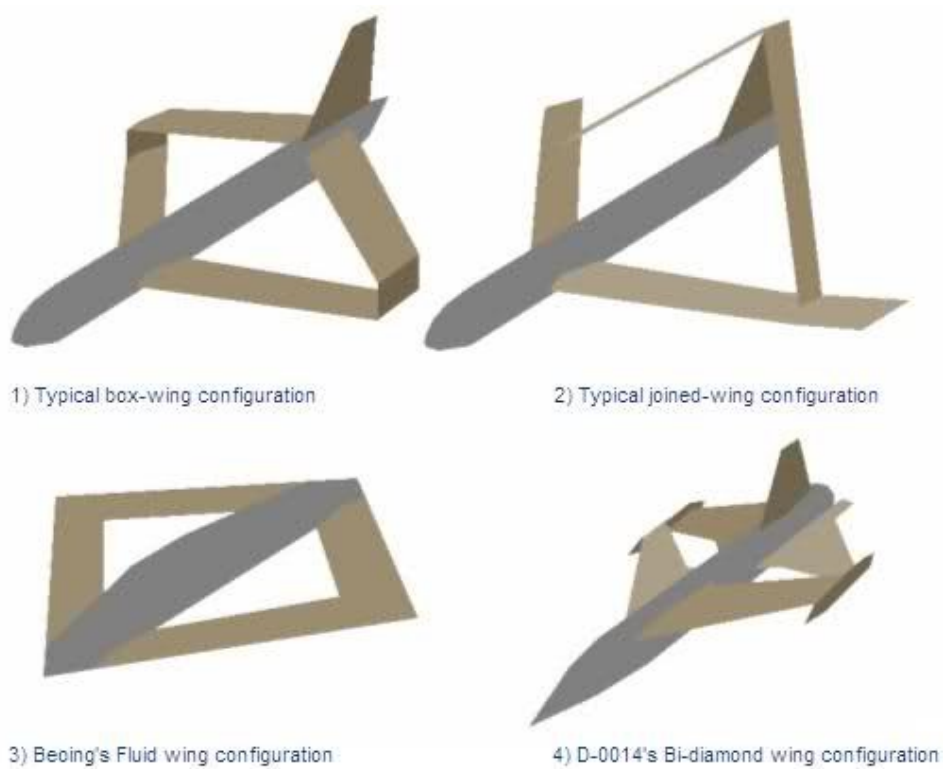


Figure 2.1. Pictorial illustrations of joined-wing configurations [3]

2.3 Multidisciplinary Design Optimization Aspects

In the design of joined-wings, the mentioned geometric parameters have great influence on the aerodynamic and structural efficiency of the system. Therefore effective designation of these parameters requires to include multidisciplinary design optimization (MDO). In particular, both the aerodynamic and the structural design of wings are the most important parts of the MDO in the wing design. Recently, the use of multidisciplinary design optimization is becoming a key element in the design of wing systems [4].

The multidisciplinary design optimization can be divided into three main categories [5]:

- 1st Category: Coupling occurs in both analysis and sensitivity levels.
- 2nd Category: Coupling occurs only in the analysis level.
- 3rd Category: Loosely coupled analysis (aeroelastic effects are ignored).

Here, the coupling means that first aerodynamic load will deform the structure then the deformed structure changes the aerodynamic load. If the coupling is considered only in the analysis level; after aerodynamic load is calculated in CFD, it is mapped into the finite element model. Then the deformation of the structure is calculated and the CFD mesh is regenerated to perform the aerodynamic analysis again for the renewed mesh. The procedure iteratively goes back and forth between CFD and CSD (Computational Structural Dynamics). Besides, the sensitivity level coupling requires the computation of the partial derivatives of interdisciplinary coupling terms between aerodynamic and structural equations, because of that, their evaluations are becomes computationally expensive. On the other hand, in the loosely coupled analysis, each discipline is considered independently, therefore, aerodynamic and structural analyses can be carried out in highest fidelity levels.

An example for the 1st category can be found in J.R.R.A. Martins et al. study [6]. The authors conducted a high fidelity sensitivity analysis with many design variables and proposed a new coupled adjoint method for performing sensitivity analysis. Furthermore, it is claimed that the proposed method has computational advantages over Global Sensitivity Equations (GSE) method [7].

An example for the 2nd category can be found in Y. Kim and et al [8] where they performed a multi-objective and MDO of supersonic fighter wing. In their study, aeroelastic deformations are considered in the analysis level by using tight coupling method. In the tight coupling method, the aeroelastic deformations are calculated for each iteration of flow solver without considering their convergence and they are transferred into structural mesh. The static aeroelastic analyses are continue until the flow solver is converged.

An example of 3rd category can be found in [9] as Blair and Canfield proposed an integrated design method for joined-wing configurations utilizing loosely coupled MDO process. They demonstrated a detailed weight minimization study using linear aerodynamic and non-linear 2D wing box structural modelling techniques.

Guruswamy and Obayashi conducted an elaborate review on the use of high fidelity methods in MDO [5]. They illustrated fidelity levels of fluid and structure modelling in Figure 2.2

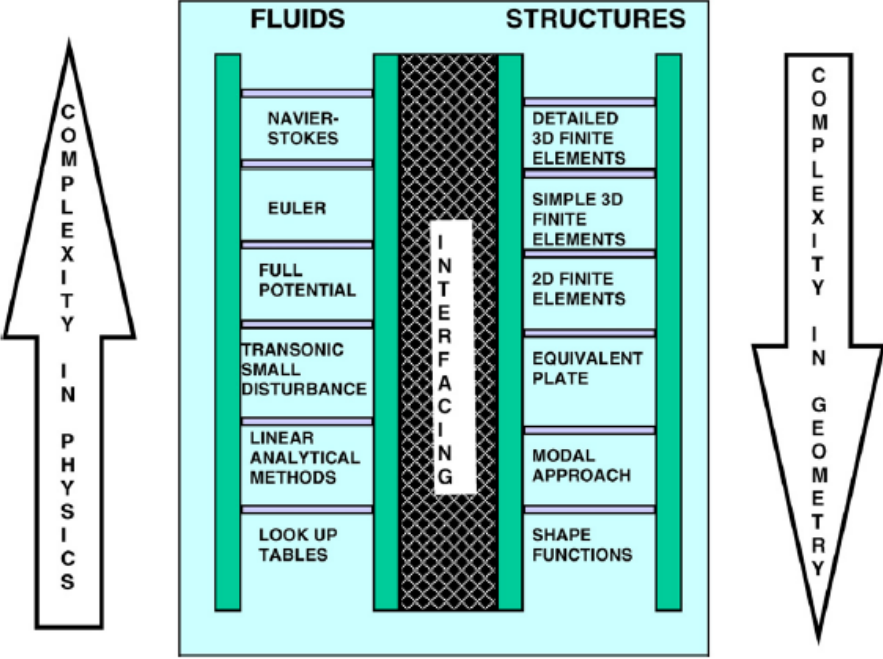


Figure 2.2. Varying levels of fidelity in modelling for fluids and structure [5]

Today, numerical modelling techniques based on the low fidelity methods is well advanced [10, 11]. Although, these low fidelity methods provide computational advantages, they are not adequate for capturing the flow nonlinearities especially in the transonic region [12]. In order to increase accuracy of the results, the use of nonlinear potential models such as Euler/Navier-Stokes are suggested [13]. Similarly, on the structure side, the use of high fidelity models are increasing parallel to the development in the computer technologies [14–16]. These models provide better understanding of structural failure behaviors and lead to optimize the structural weight efficiently.

With the advent of the developments in computer capabilities, higher level of complex simulations have been extensively applied to multidisciplinary applications. Indeed, as the development in realism makes the use of numerical analyses extremely

challenging, the level of complexity makes their evaluation computationally expensive. To overcome this computational cost, the use of design of experiment (DOE) techniques [17, 18] with meta modelling techniques (so-called surrogate models) such as response surface methodology (RSM) [19] is becoming routine for MDO optimization. Moreover, the use of RSMs in association with loosely coupled analyses fades out numerical noise which may lead erroneous evaluations [20]. In the optimization phase of response surfaces, the use of genetic algorithms have been used more and more in recent years due advantages of robustness in noisy design environments [21, 22].

2.4 Multidisciplinary Design Optimization Architectures

One of the essential considerations when performing MDO is how to organize the optimization problem including the discipline analysis, surrogate models (if any), and optimization software so that an optimal design is achieved. Such a combination of problem formulation and organizational considerations is called as MDO architecture [4]. There are two approaches in MDO architectures: monolithic and distributed. A monolithic approach considers different disciplines as a single optimization problem. On the other hand, in a distributed approach the same problem is decomposed into a set of smaller optimization problems. Before providing brief summary of particular MDO architectures, general definitions and goals of MDO is presented below.

The goal of an optimization is to achieve the best outcome of a given operation by finding the best combinations of variables while satisfying certain restrictions. The quantity to be improved and used as a measure of effectiveness is termed the objective function. In general notation; f holds for objective function, x holds for the design variables and c is used for the vector of constraints. Design variables can be local design variables, i.e., variables that affect only one discipline or shared desired variables, z , which are the variables shared by multiple disciplines. The coupling variables should also be considered and they are denoted by y .

There have been made numerous survey of MDO architectures over the last two decades. In this study, elaborate surveys of MDO architectures reviewed by Haftka et al. [23], Martins et al.[24], Kroo [25] and Martins et al [4] are analyzed. According to these reviews, some of the monolithic and distributed MDO architectures are summarized and discussed below.

Multidisciplinary –Feasible Design (MDF)

This approach considers different disciplines as a single monolithic analysis. It is conceptually very simple, first all disciplines are coupled to form one single multidisciplinary analysis, then the same techniques that are used in single design optimization are implemented. The optimization problem for the MDF architecture is;

$$\begin{aligned} &\text{minimize} && f(z, x, y(x, y, z)) \\ &\text{w.r.t.} && z, x \\ &\text{s.t.} && c(z, x, y(x, y, z)) \geq 0 \end{aligned}$$

Simultaneous Analysis and Design (SAND)

This monolithic approach optimizes the design and solves the governing equations at the same time. The optimization problem for the SAND architecture is;

$$\begin{aligned} &\text{minimize} && f(z, x, y) \\ &\text{w.r.t.} && x, y, z \\ &\text{s.t.} && c(z, x, y) \geq 0 \\ &&& \mathcal{R}(x, y, z) = 0 \end{aligned}$$

where R is the analysis constraint.

One of the advantages of the SAND is that there is no need to solve any discipline analysis explicitly or exactly at each iteration. The SAND is not restricted to multidisciplinary systems and can also be used for single discipline problems.

Individual Discipline Feasible (IDF)

In this approach, instead of solving the coupling variables between the disciplines, they are given by the optimizer as a guess, y^t . The optimization problem can be written as;

$$\begin{aligned}
& \text{minimize} && f(z, x, y(x, y^t, z)) \\
& \text{w.r.t.} && z, x, y^t \\
& \text{s.t.} && c(z, x, y(x, y^t, z)) \leq 0 \\
& && y_i^t - y_i(x, y^t, z) = 0.
\end{aligned}$$

The size of the optimization problem is increased due to added coupling term estimates. Although size of the problem is increased, all the analyses are decoupled, and therefore they can be solved in parallel without intercommunication.

Collaborative Optimization (CO)

The goal of this approach is to decouple design in various disciplines. Each subproblem is given control over its own set of local design variables, is responsible for satisfying its own set of local constraints and does not know about the other disciplines' design variables or constraints. The objective of each subproblem is to agree on the values of the coupling variables with the other disciplines. A system-level optimizer is used to coordinate this process while minimizing the overall objective. The optimization problem can be stated as;

$$\begin{aligned}
& \text{minimize} && f(z^t, y^t) \\
& \text{w.r.t.} && z^t, y^t \\
& \text{s.t.} && J_i^*(z_i^t, z_i^*, y^t, y_i^*(x_i^*, y^t, z_i^*)) = 0, \quad i = 1, \dots, N
\end{aligned}$$

where N is the number of disciplines, and the subscript * represents the results from the solution of ith discipline optimization subproblem.

Concurrent Subspace Optimization (CSSO)

In this distributed approach system decomposed to subproblems and in each subproblem, disciplinary analyses are replaced by surrogate models. Discipline subproblems are solved used by surrogate models for the other disciplines. The optimization formulation for CSSO is given in two step.

System level optimization problem is given;

$$\begin{aligned}
&\text{minimize} && f(z, x, \tilde{y}(z, x)) \\
&\text{w.r.t.} && z, x \\
&\text{s.t.} && c(z, x, \tilde{y}(z, x)) \leq 0
\end{aligned}$$

and the discipline i^{th} subproblem is;

$$\begin{aligned}
&\text{minimize} && f(z, x, \tilde{y}_j(z_i, x_i), y_i(x_i, \tilde{y}_j, z_i)) \\
&\text{w.r.t.} && z_i, x_i \\
&\text{s.t.} && c(x_i, z, \tilde{y}_j, (z_i, x_i), y_i(z_i, x_i, \tilde{y}_j)) \leq 0.
\end{aligned}$$

A framework for automatic implementation of MDO architectures [24] given in Figure 2.3.

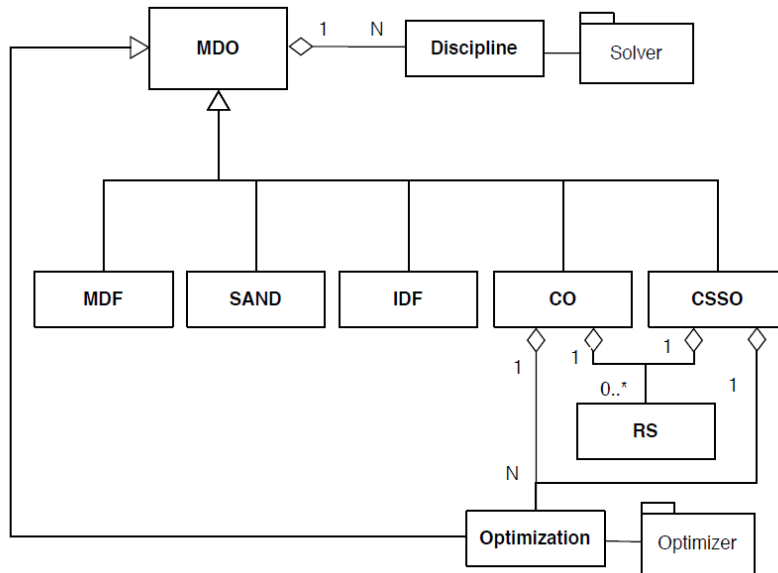


Figure 2.3. A framework for automatic implementation of MDO architectures [24]

2.5 Discussion and Conclusions

In this chapter, the joined-wings are briefly described and their advantages are introduced. Afterwards, the multidisciplinary design aspects came up to the attention and therefore they are then reviewed under the various subtopics, such as; the fidelity levels of fluid and structural modelling, numerical modelling techniques, meta-modelling techniques and optimization algorithms. The past and ongoing studies on the MDO and its architectures are also reviewed. In this case, the optimization problem

can be considered in the MDF MDO architecture. Regarding the various categories of the MDO [5], this thesis lies into the 3rd category as analyses for the joined-wings can be made independently for each discipline so that computationally intensive high fidelity level methods can be used individually and as the aeroelastic effects are ignored, the computational burden of coupled analyses are mainly reduced.

CHAPTER 3

RESEARCH PROBLEM

3.1 Introduction

In this chapter, the research problem is introduced and explained. First, external loadings are anticipated during a typical mission of the munition. Typical mission profile of the munition and the V-N diagram are presented. Then, the joined-wing geometric parameters are clarified. Finally, the tools used in design, optimization and verification are introduced.

3.2 Structural Loads on the Joined-Wing Configurations

The mission scenario of the munition is shown at Figure 3.1. After munition is separated from the aircraft, a guidance algorithm drives it to the target. When the munition approaches to the target area, final guidance algorithm arranges its target stroke angle and target stroke velocity.

In this thesis, cruise speed and maneuver flight conditions are considered. In the cruise speed condition, an aerodynamic lift distribution on the munition is equal to the total weight of the munition. On the other hand, in the maneuver flight condition, the net lift distribution is 2.5 times the total weight of the munition and this comes from the set value of 2.5g pull up maneuver. The maneuver load factor basically comes from the guidance requirements and safety considerations. Considering mission profile and the guidance requirements the flight envelope (V-N diagram) is constructed and showed in Figure 3.2.

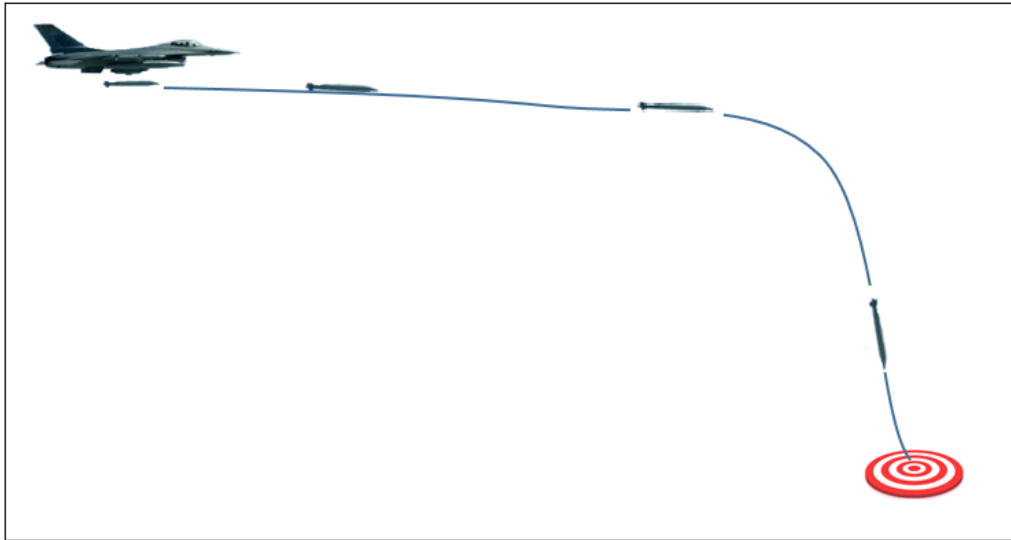


Figure 3.1. Typical mission profile of the munition

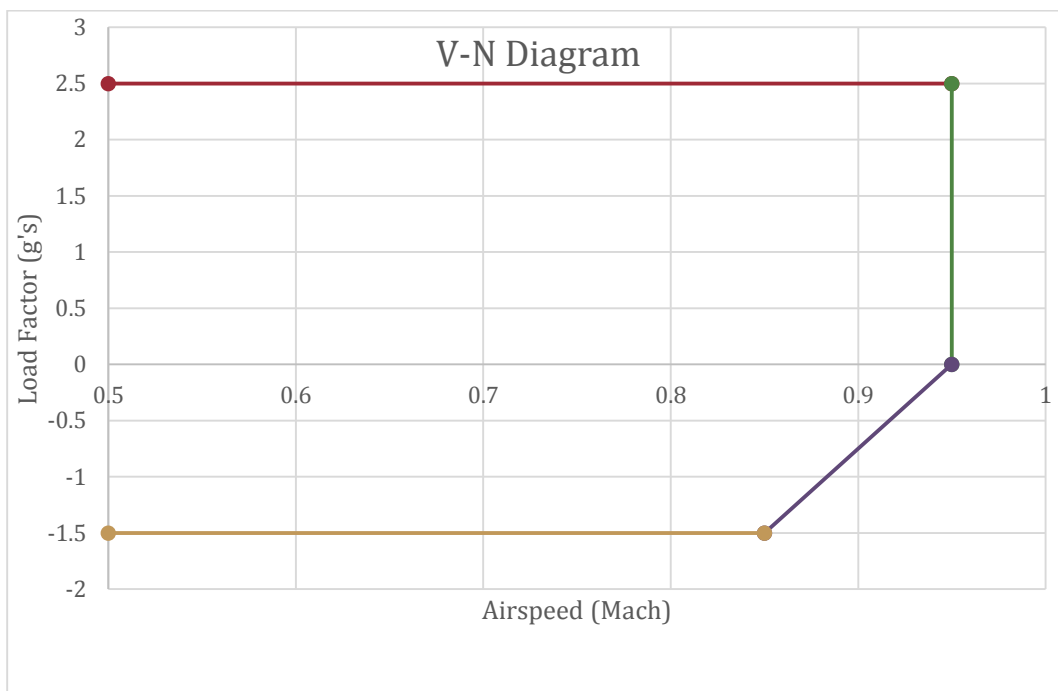


Figure 3.2. Velocity-Load diagram of the munition

3.3 Variables for the Joined-Wing Configurations

Each geometric configuration is defined by two key independent design variables; namely the aft wing sweep angle (Λ_a) and the joint location (S_{JL}). Figure 3.4 illustrates the typical joined-wing configuration used in this study and Table 3.1 summarizes the related geometric parameters and variables used in order to settle the range of configurations. In these configurations, the key parameters; the aft wing sweep angle (Λ_a) is defined as the angle the aft wing creates with fuselage and the joint location (S_{JL}) is defined as the parallel distance between axis of the intersection point where the front wing coincides with the aft wing and the intersection point where the front wing connected to fuselage. Since the munition will be mounted to the rack unit at the weapon station of the fighter, the wing kit's outer dimensions are dependent to the rack unit dimensions. The dimensions of chord at front wing (c_f) and aft wing (c_a) are defined by considering this limitation.

All chord lengths and thicknesses were set constant to meet limitations of munition rack unit dimensions. The dimensions of the munition rack unit are shown in Figure 3.3.

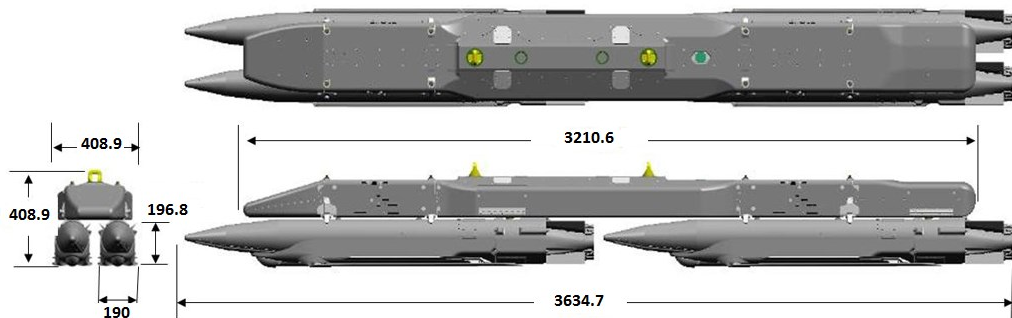


Figure 3.3. Munition rack unit (dimensions in mm)

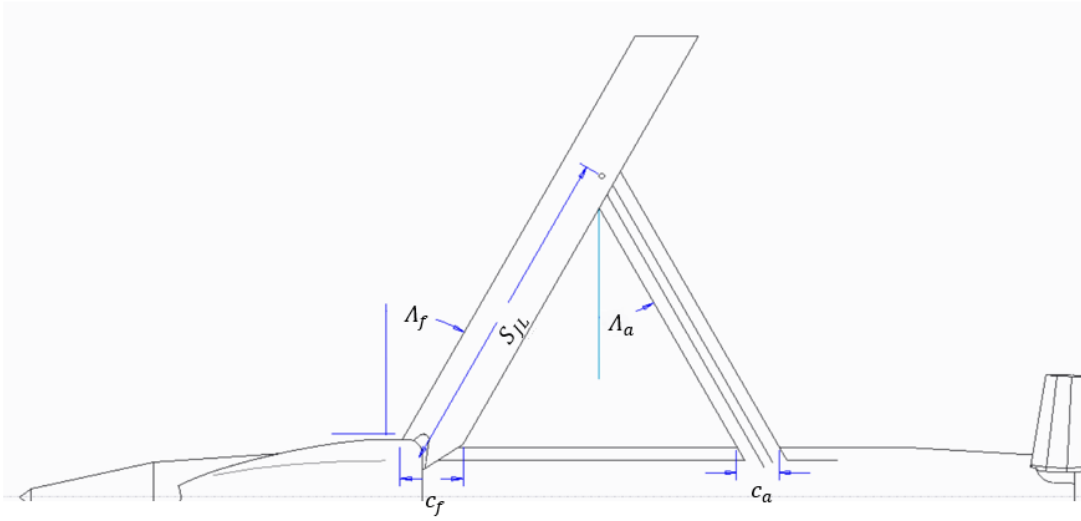


Figure 3.4. Design parameters and variables of the joined-wing

Table 3.1. Definition of design parameters and variables of the joined-wing

Variable	Name	Size
S_{JL}	Joint location	Varies
Λ_f	Front wing sweep	30°
Λ_a	Aft wing sweep	Varies
c_f	Chord at front wing	103.9 mm
c_a	Chord at aft wing	69.3 mm

In order to reduce the analysis domain within a conceivable scope, the “aft wing sweep angle” and the “joint location” are allowed to change from 0° to 30° and from 350 mm to 750 mm, respectively. The upper and lower bounds are listed in the Table 3.2. Also the pictorial illustrations of upper and lower bounds for the parameters are shown in Figure 3.5.

Table 3.2. Upper and lower bounds

Variable	Name	Lower bound	Upper bound
S_{JL}	Joint location	350 mm	750 mm
Λ_a	Aft wing sweep	0°	30°

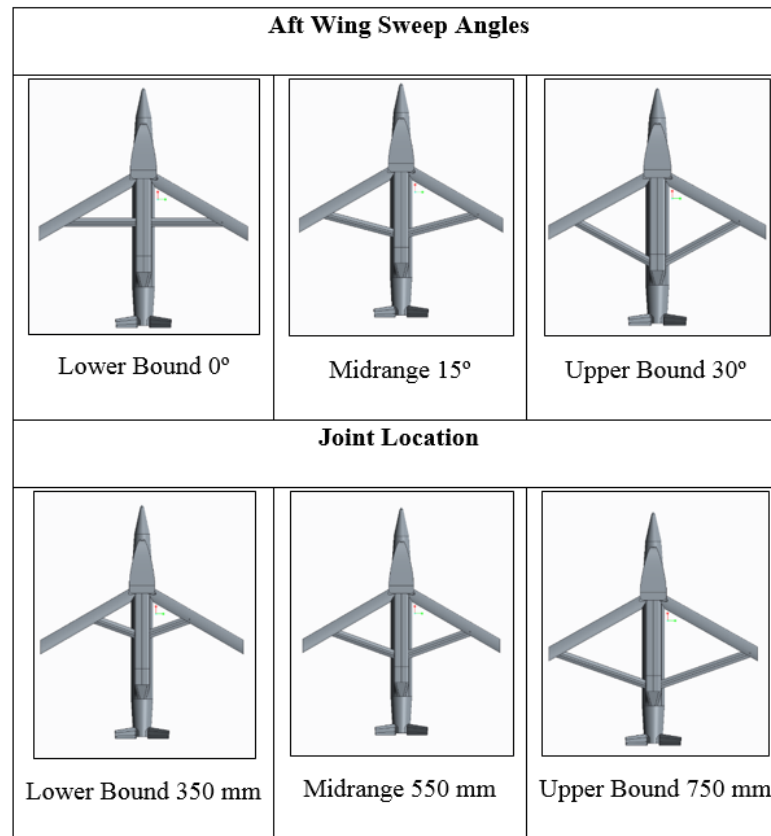


Figure 3.5. Pictorial illustrations of upper and lower bounds

3.4 Analyses and Experimental Tools

This thesis can be divided into 2 parts; in the first part, dynamic characteristics of the joined-wings are investigated and their experimental validations are performed through various modal tests. Finite element models for modal analyses are constructed in ANSYS® 15.0.7 software [26] . For the experiments PULSE Labshop 16.1.0 [27] is used. Post processes are done by using MEscape'VES [28] and MATLAB software. In the second part, multi-objective multidisciplinary design optimizations of the joined-wings are performed. In the Figure 3.6, the flowchart for MDO process is presented.

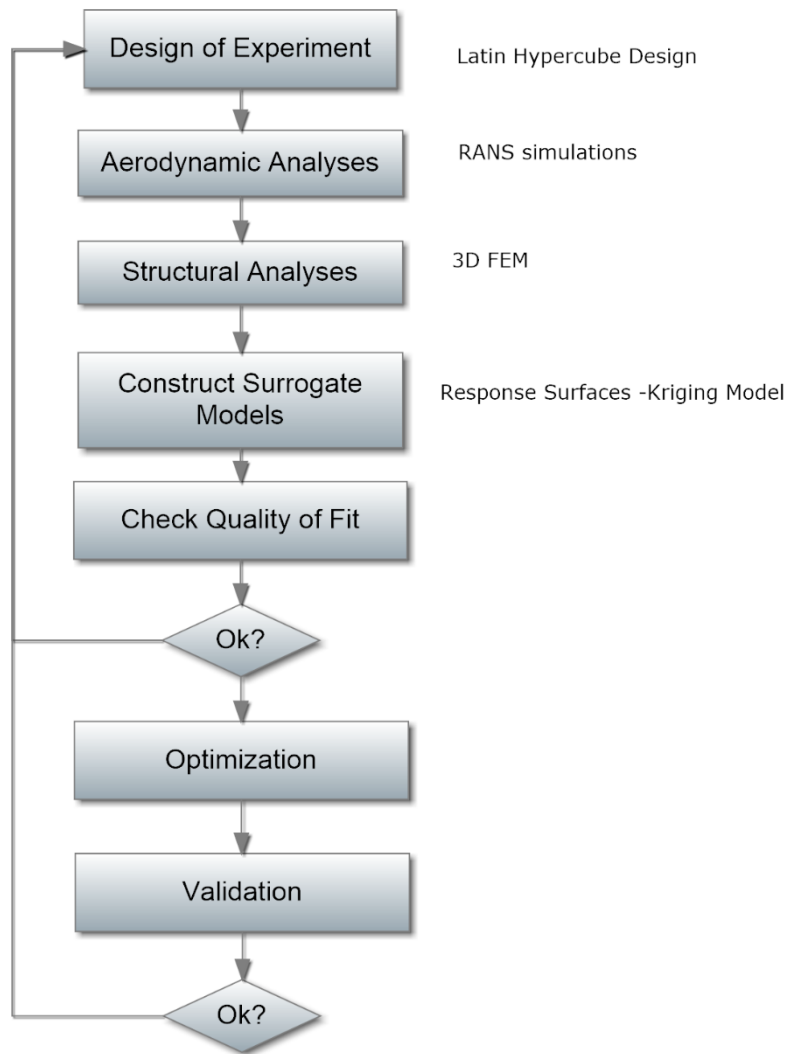


Figure 3.6. Flowchart for MDO process

In Chapter 6, aerodynamic analyses are explained in details. ANSYS Fluent is used as an aerodynamic analysis tool. The structural analyses are conducted by using ANSYS Mechanical and the details of these structural analyses can be found in Chapter 7. Surrogate modelling techniques, design of experiments, refinement and optimization procedure are introduced on the ANSYS Design Exploration tool in Chapter 8. For better understanding, henceforth; S_{JL} : 350mm , A_a : 0 degree and S_{JL} : 750mm , A_a : 20 degree will be called as “Design Point 1” and “Design Point 2” throughout this thesis. All illustrations and results in Chapter 4, 5, 6, 7 will be explained on these selected points. Although the extreme points are at the positions of S_{JL} : 350mm , A_a : 0 degree and S_{JL} : 750mm , A_a : 30 degree, considering experimental setup, S_{JL} : 750mm , A_a :

30 degree are not feasible to assemble due to available subparts. Therefore, Design Point 2 is selected at S_{JL} : 750mm , A_a : 20.

3.5 Discussion and Conclusions

In this chapter, research problem is briefly introduced and the design geometry is explained with its geometric parameters and design limitations. The mission profile and the corresponding V-N diagram is constructed. Finally, analyses performed during the study and the analyses tools are described.

CHAPTER 4

FINITE ELEMENT MODELLING AND ANALYSES OF JOINED-WING CONFIGURATIONS

4.1 Introduction

Modal Analysis can be defined as a process whereby a structure is described by in terms of its dynamic characteristics which are the natural frequencies, the corresponding mode shapes and the damping ratios. These natural characteristics affect the response of the structure when a force excites it. Understanding both the natural frequencies and the corresponding mode shapes and knowing their effects on the structure helps engineers to design better structures [29].

In this chapter, in order to determine the vibration effects on the joined-wing configurations, dynamic characteristics of them are investigated through modal analyses. All results are shown for the two aforementioned selected joined-wing configurations.

4.2 Finite Element Modelling of the Selected Joined-Wing Configurations

In order to investigate dynamic characteristics of the joined-wing configurations, finite element method is used. ANSYS® 15.0.7, commercial finite element code [26], is used for modelling the selected joined-wing configurations. 3D parametric computer aided design (CAD) model is constructed in Creo 2.0, an advanced CAD program [30]. Then ANSYS® and Creo are connected each other directly so that if the geometric parameters are changed in CAD model, finite element model is automatically updated. The parametric CAD model consists of two front wings, two aft wings, a sliding connection block, two guidance shafts and a front block. The isometric and the

exploded views of the joined-wing geometry can be seen in Figure 4.1 and Figure 4.2, respectively.

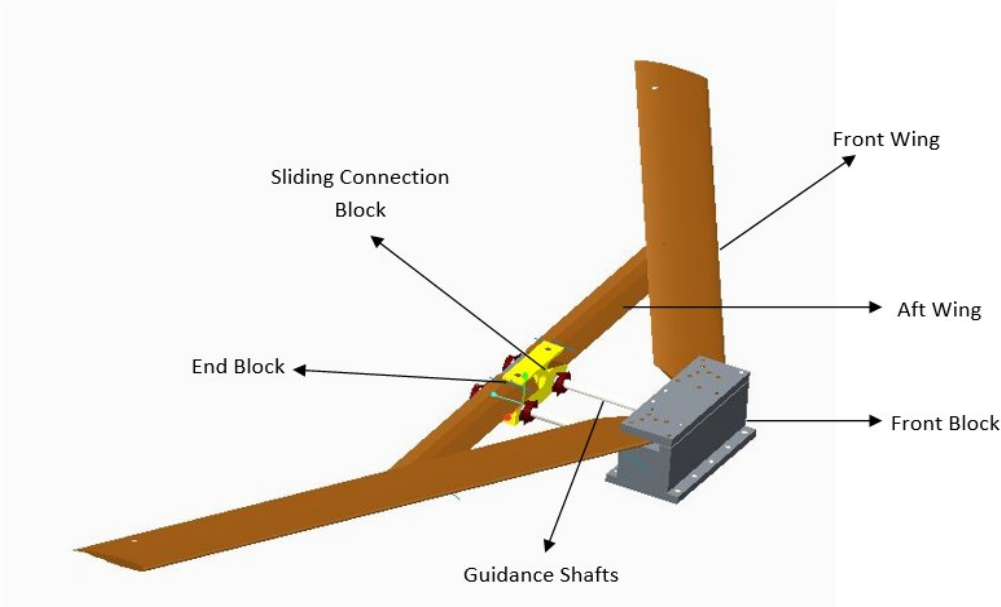


Figure 4.1. Isometric view of the joined-wing geometry

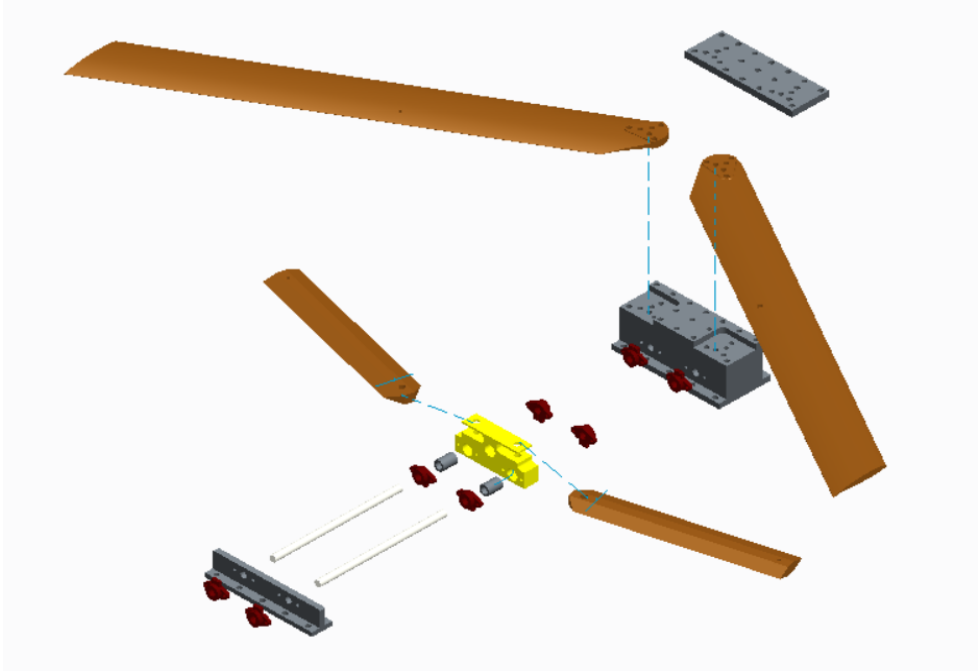


Figure 4.2. Exploded view of joined-wing geometry

In the design of the front and aft wing, NASA Super critical airfoil-SC(2) 1010 and hexagonal cross section are used. The general dimensions of the front wing, aft wing and the joined-wing assembly are displayed in Figure 4.3, 4.4 and 4.5

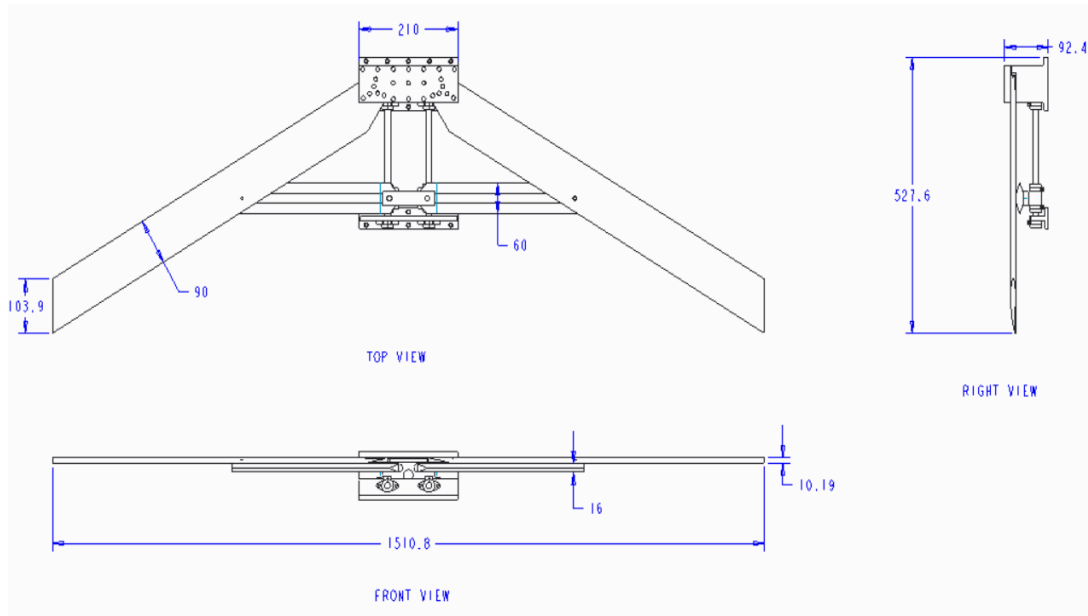


Figure 4.3. General dimensions of joined-wing assembly [mm]

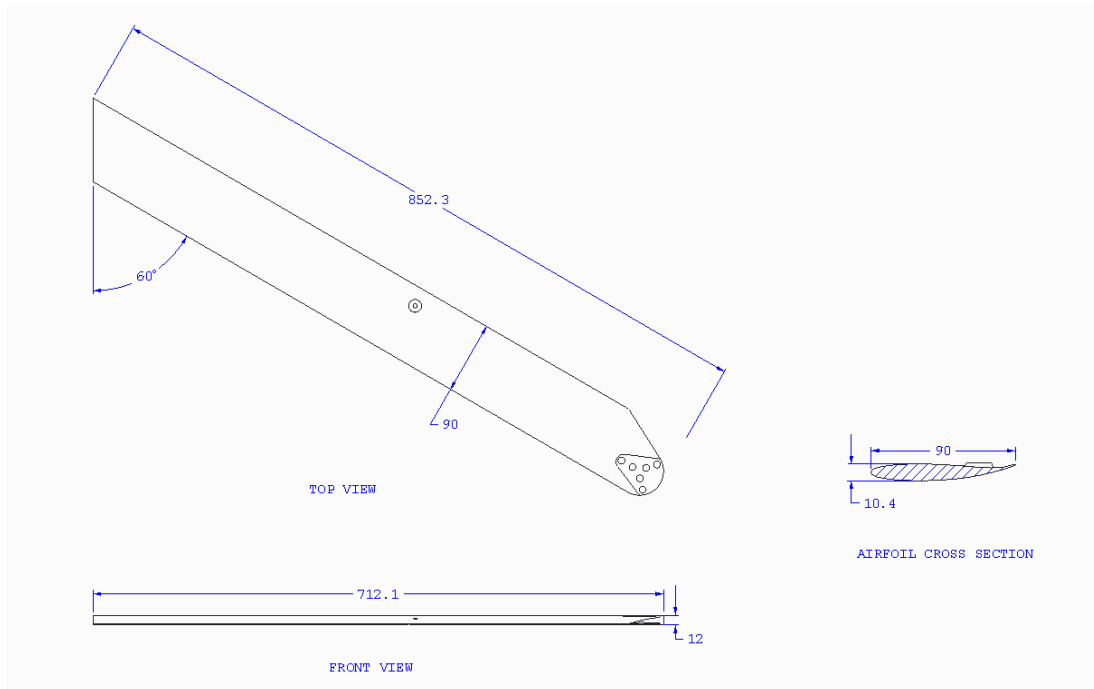


Figure 4.4. General dimensions of the front wing [mm]

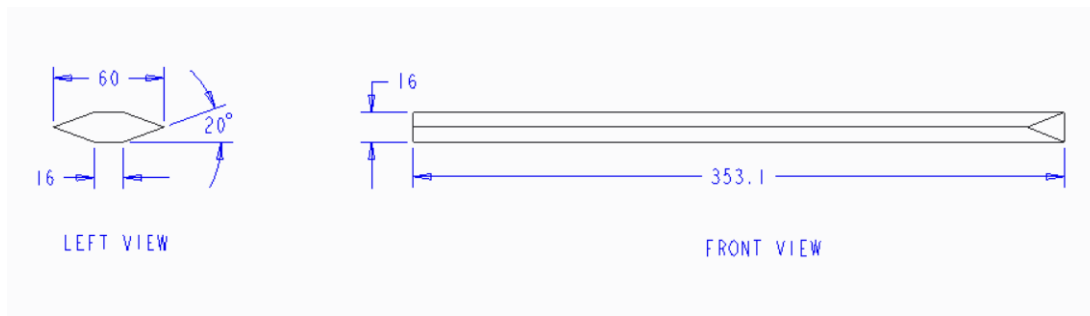


Figure 4.5. General dimensions of the aft wing [mm]

In the front and aft wings, aluminum 6061-T6 alloy and in the front block, the sliding connection block and guidance shafts, steel is used as a material. The properties of these materials are inserted from the material library of ANSYS. A twenty node hexagonal (Solid 186) and a ten node tetrahedron (Solid 187) higher order 3D solid elements that exhibits quadratic behavior are utilized. The mesh independency study is also performed and the results are given in Appendix A. According to mesh independence study, the global mesh sizing is used and it is determined as 4 mm. The total number of elements and nodes used in the finite element modelling of joined-wings are 275231 and 462653, respectively. All body to body contacts such as connection between front wing and front block is defined as bonded and in this contact type the two body is assumed rigidly connected to each other. The body to body contact regions of the joined-wing can be seen in Figure 4.6. In addition to the body to body contacts, in order to simulate the connection between the munition and joined-wing assembly, fixed boundary condition is designated to the bottom surfaces of front and aft blocks by fixing three degrees of freedom. The fixed boundary condition region is shown in Figure 4.7. The reason for defining all body to body connections and boundary conditions as rigidly fixed is from the fact that in the real life application there are locking mechanisms in order to keep the joined-wing kit in its desired position. Typical mesh for the joined-wings is displayed in Figure 4.8.

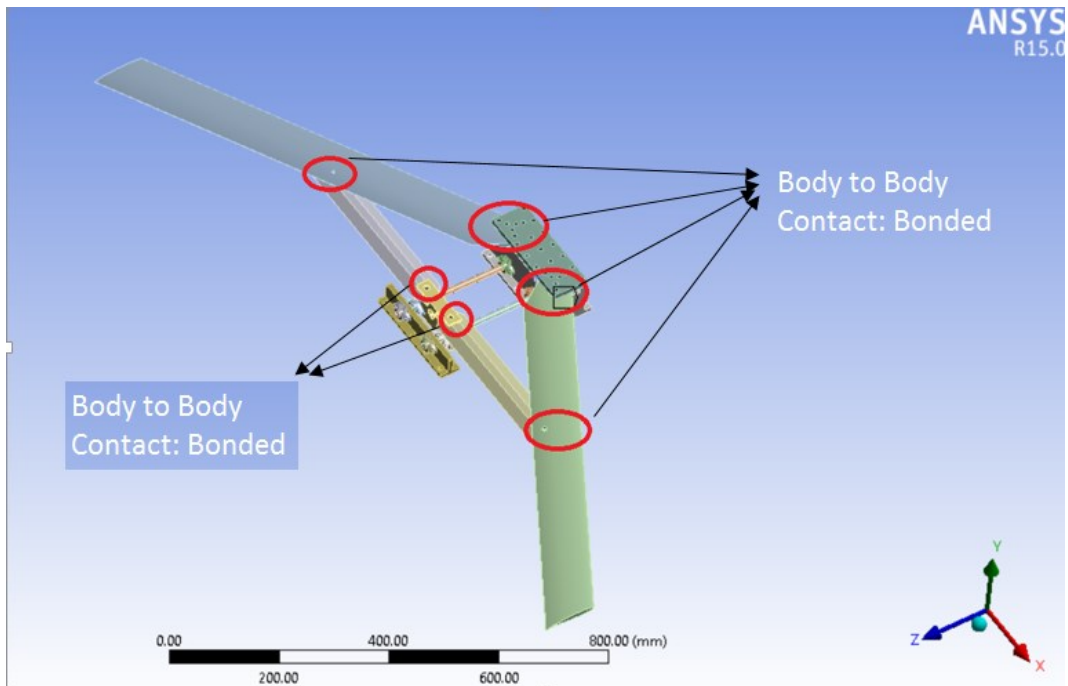


Figure 4.6. Body to body contact types of the joined-wing connections

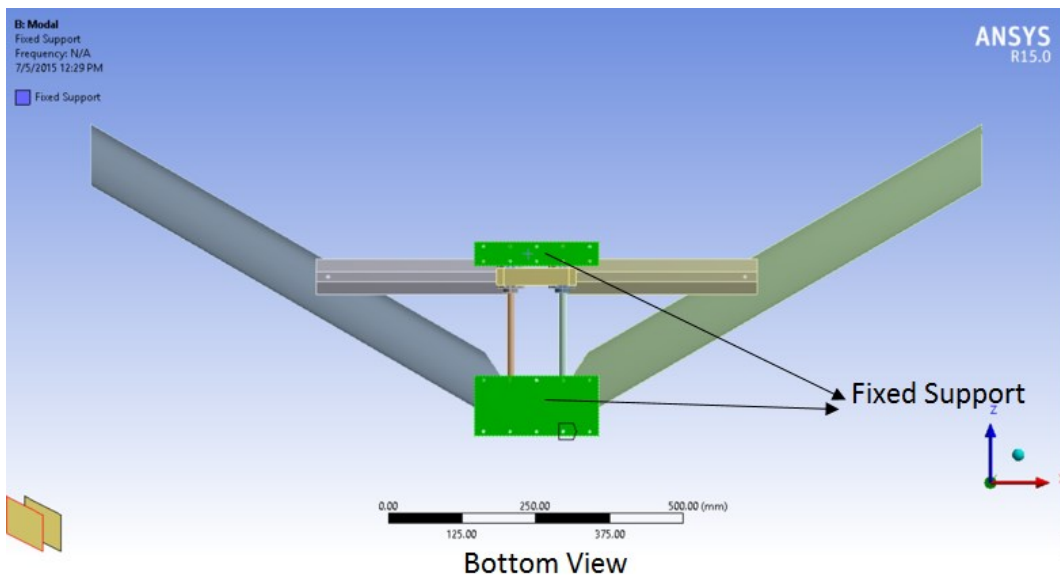


Figure 4.7. Fixed boundary condition of joined-wing

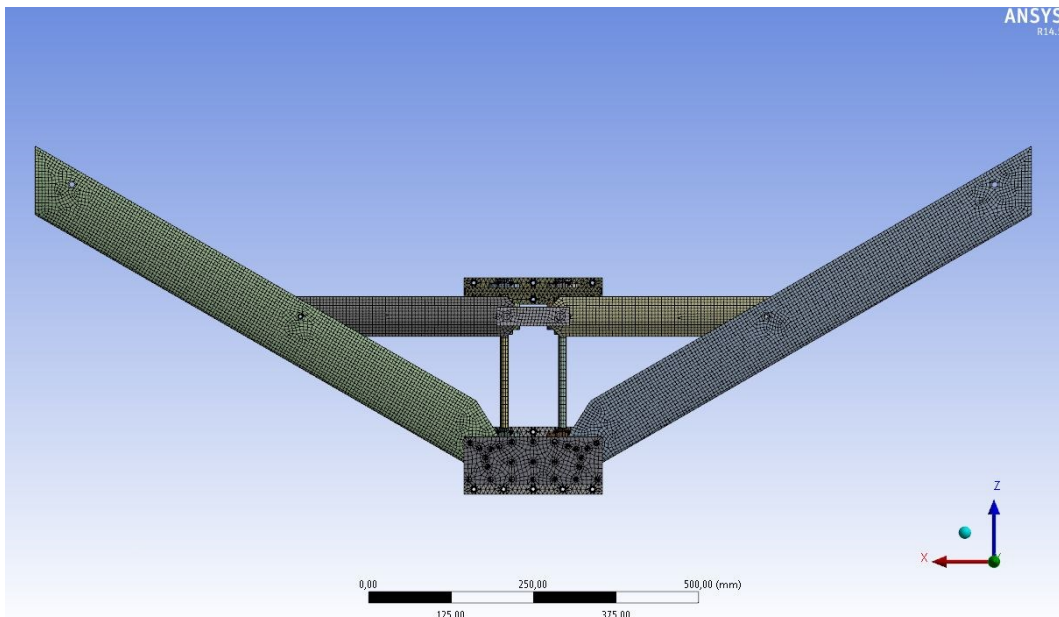


Figure 4.8. Mesh of the sample joined-wing geometry

4.3 Modal Analyses of the Selected Joined-Wing Configurations

After constructing finite element model, modal analyses are performed for the first six modes of the joined-wings. The first six natural frequencies and the corresponding mode shapes are then found for both the Design Point 1 and the Design Point 2. The natural frequencies are listed in the Table 4.1 and Table 4.2 and the corresponding mode shapes are showed in the Figure 4.9 and Figure 4.10.

Table 4.1 Natural frequencies of the joined-wing for Design Point 1 and their descriptions

Mode	Frequency (Hz)	Description of the free vibration modes
1	20.89	Front wing first anti-symmetric out-of-plane bending
2	20.98	Front wing first symmetric out-of-plane bending
3	84.84	Front wing second anti-symmetric out-of-plane bending, Aft wing first anti-symmetric out-of-plane bending
4	85.19	Front wing second symmetric out-of-plane bending, Aft wing first symmetric out-of-plane bending
5	192.95	Front wing first anti-symmetric in-plane bending, Aft wing second symmetric out-of-plane bending
6	197.25	Front wing first symmetric in-plane bending, Aft wing second anti-symmetric out-of-plane bending

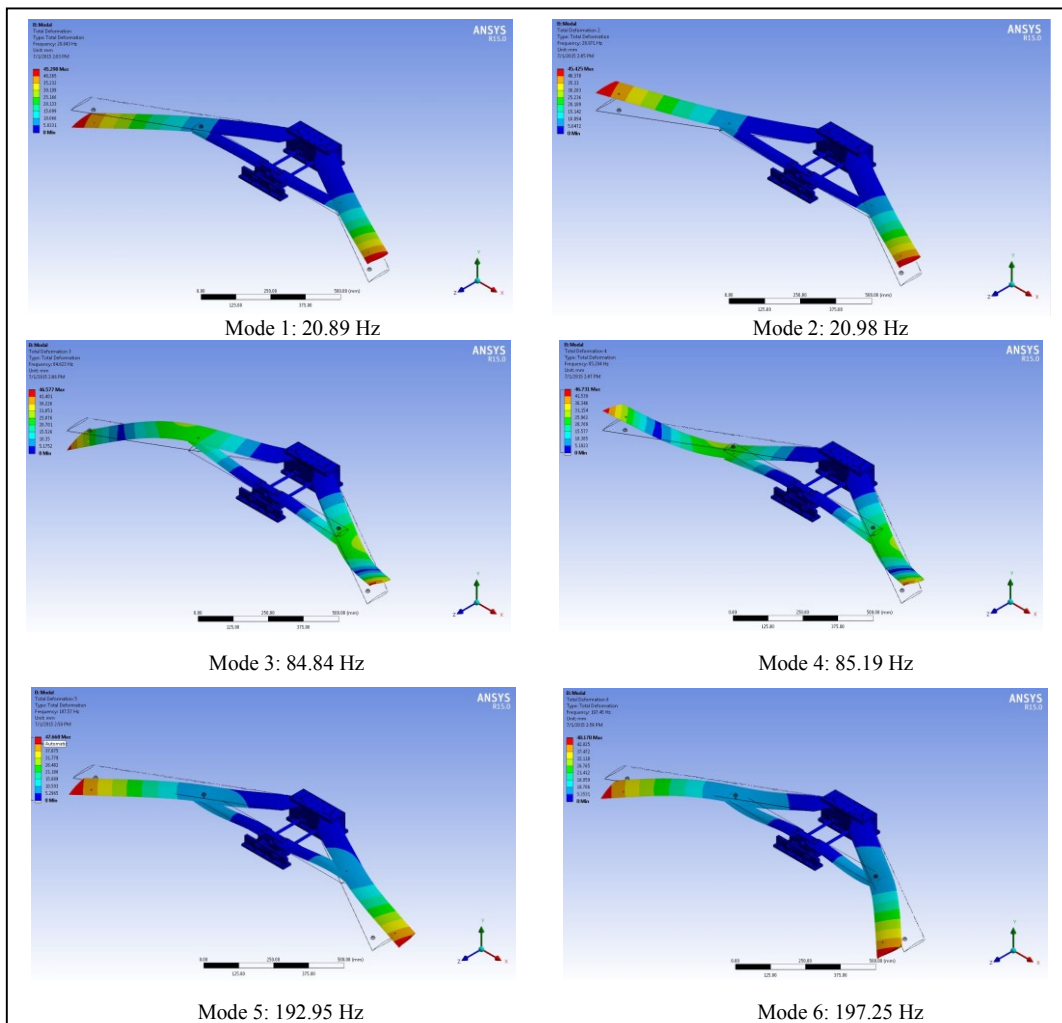


Figure 4.9. Corresponding mode shapes of the of joined-wing for Design Point 1

Table 4.2. Natural frequencies of the joined-wing for Design Point 2 and their descriptions

Mode	Frequency (Hz)	Description of the free vibration modes
1	17.99	Front wing first symmetric out-of-plane bending, Aft wing first symmetric out-of-plane bending
2	18.00	Front wing first anti-symmetric out-of-plane bending, Aft wing first anti-symmetric out-of-plane bending
3	78.86	Front wing second anti-symmetric out-of-plane bending, Aft wing mixed
4	78.89	Front wing second symmetric out-of-plane bending, Aft wing mixed
5	108.54	Front wing torsion-bending mixed, Aft wing second symmetric out-of-plane bending
6	114.60	Front wing torsion-bending mixed, Aft wing second anti-symmetric out-of-plane bending

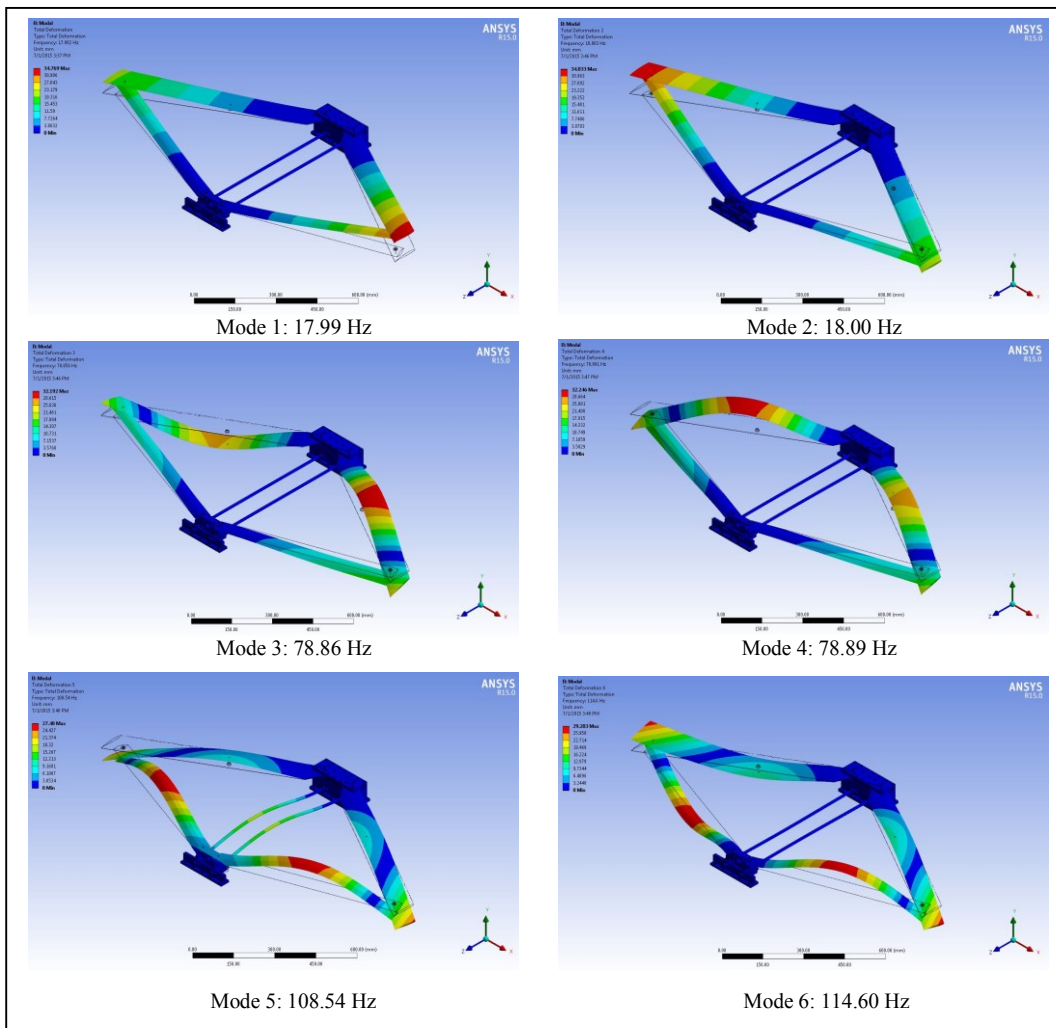


Figure 4.10. Corresponding mode shapes of the of joined-wing for Design Point 2

4.4 Discussion and Conclusions

In this chapter, after parametric CAD models of the joined-wings are created, finite element models of them are also constructed. The first six natural frequencies and the corresponding mode shapes of the selected design points are extracted in order to anticipate dynamic properties of the joined-wings. Here, as mentioned before, the Design Point 1 and the Design Point 2 represent the possible extremes of the upper and lower bounds. As it can also be seen from their mode shape illustrations from Figure 4.9 and 4.10 that they have the same shape for the first four modes however for higher order modes, the mode shapes show huge variety. Therefore, it can be concluded that the changes in the key parameters have strong impact on the structure's dynamic characteristics.

CHAPTER 5

EXPERIMENTAL VALIDATION OF THE JOINED-WING CONFIGURATIONS

5.1 Introduction

In the modal test, both the response of the structure and the excitation are measured in time domain simultaneously. The ratio of the response and applied force in frequency domain is called as Frequency Response Functions (FRFs). FRFs contain real and imaginary components. They can be shown in magnitude vs. frequency, phase vs. frequency, real and imaginary parts vs. frequency graphs. The usefulness of these FRF is that the modal data can be extracted from FRF graphs.

The modal test has wide range of application area. The most common application area is the validation of a finite element model. In other words, in the validation process, the dynamic behavior of the structure is obtained in order to compare the results with the corresponding data calculated from a finite element analysis (FEA). This application is needed in order to validate the theoretical model with the experimental results so that, the design engineer could get the proven theoretical model and then can use it safely in the analyses.

In this chapter, first, in order to determine the excitation points, virtual tests are planned, then the modal test setup and the software are introduced. Finally, impact hammer tests and shaker tests are performed for the selected joined-wing configurations.

5.2 Virtual Test on the Selected Joined-Wing Configurations

In order to ensure that a given mode is excited, it is necessary to know that an excitation point is not at or close to a nodal line.

Two Criteria are used for determining good or bad excitation points:

- Optimum Driving Point (ODP)
- Non-Optimum Driving Point (NODP)

5.2.1 Optimum Driving Point (ODP) Technique

The ODP technique is used to diagnose positions which are close to or at the nodal lines of any node within an interested frequency range [31]. The calculation procedure is simply done by multiplying all modal constants of each Degree of Freedom (DOF) for all selected modes and the value is appointed to a coefficient called the ODP parameter for each DOF. Mathematical formulation can be expressed as follows:

$$ODP(i) = \prod_{r=1}^m \|\phi_{i,r}\| \quad (5.1)$$

where;

ϕ : Mode shape matrix,

i: DOFs

r: Normal modes

m: Interested mode shapes

In order to calculate ODP parameters, mass normalized mode shape vectors of selected possible excitation positions for the first six mode are extracted via ANSYS APDL. After, ODP values are calculated in MATLAB, they are mapped to structure mesh in order to visualize ODP. The ODP values can be seen in Figure 5.2 and 5.3. The red color areas represent where the ODP are maximum.

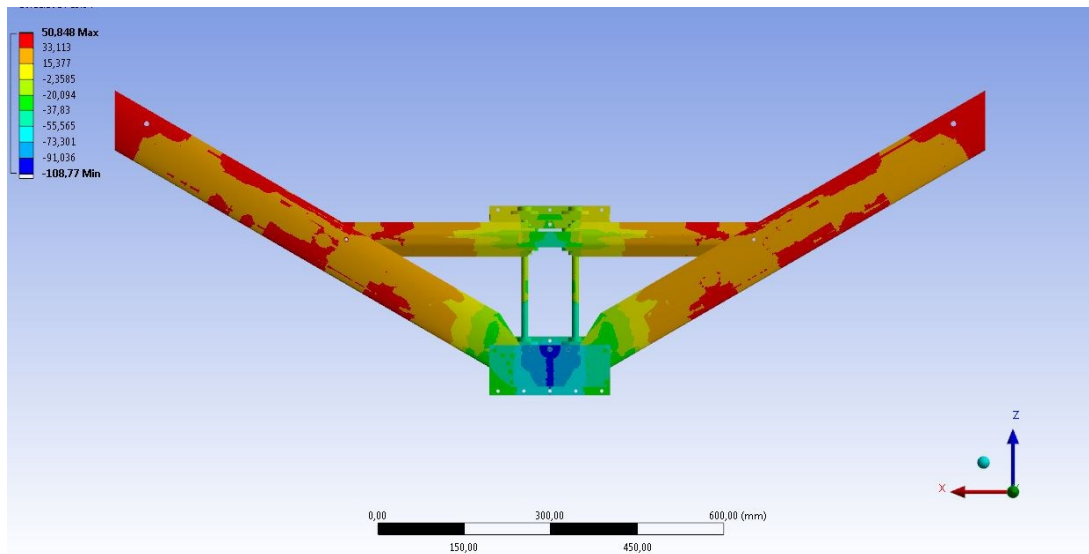


Figure 5.1. ODP of the Design Point 1

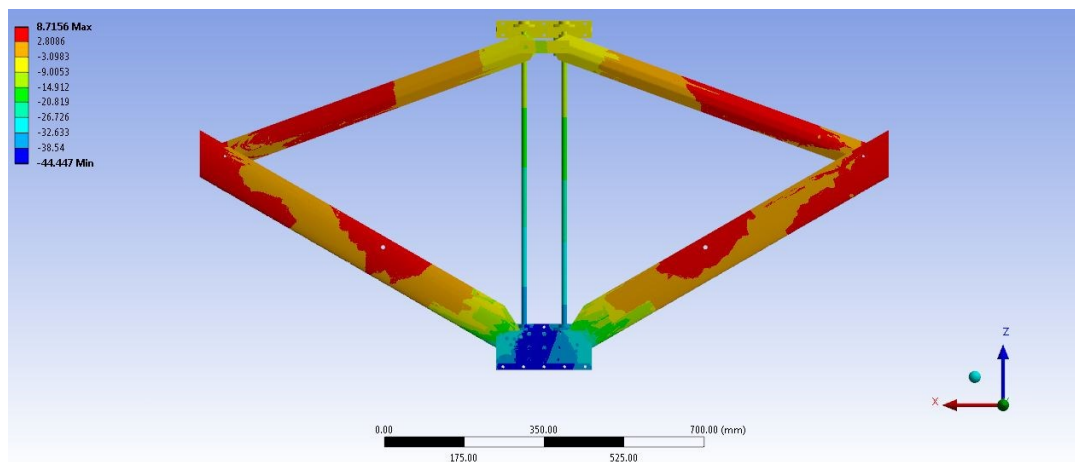


Figure 5.2. ODP of the Design Point 2

5.2.2 Non-optimum Driving Point (NODP) Technique

The NODP method defines a parameter for each DOF that identifies how close that DOF is to a nodal line of any mode within a prescribed frequency range [31]. This method selects the smallest absolute of the modal constants for all interested modes for a DOF and assigns that value as a NODP parameter for that DOF. Mathematical formulation can be expressed as follows:

$$NODP(i) = \min_r(\|\phi_{i,r}\|) \quad (5.2)$$

In order to calculate NODP parameters, mass normalized mode shape vectors of selected possible excitation positions for first six mode are extracted via ANSYS APDL. After, NODP values are calculated in MATLAB, they are mapped to the structure mesh in order to visualize NODP. In the Figure 5.3 and 5.4, the NODP values can be seen. The blue color represents the closest regions to the nodal lines of the all excited modes.

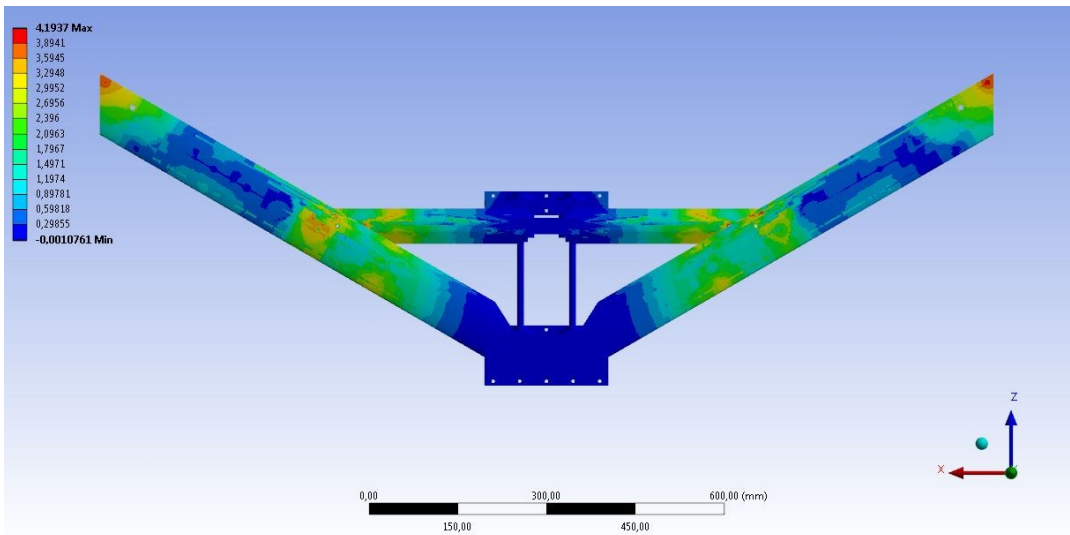


Figure 5.3. NODP of the Design Point 1

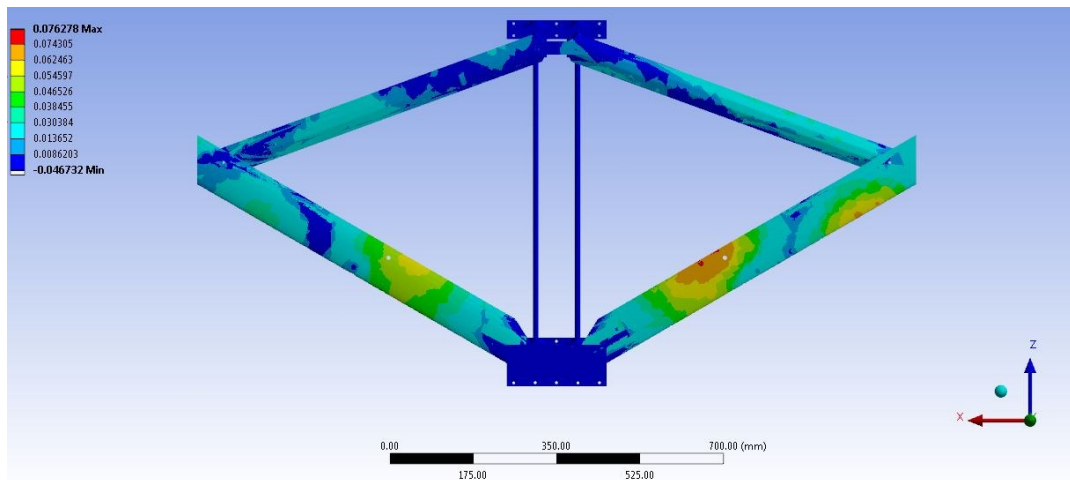


Figure 5.4. NODP of the Design Point 2

5.3 Modal Test Setup and Configurations

Designing of a test fixture has a significant role in modal testing. In order to get well matched results between FEA and modal test, all connections and the boundary conditions should be delicately simulated in the test setup. In this experiment, the connections at all joint locations are assumed as rigid since in the real life application there are locking mechanisms in order to fix the joined-wing geometry.

The test setup is manufactured by help of the ASELSAN Inc. Manufactured joined-wing configurations are rigidly connected to a fixed test table, which is constructed from aluminum sigma profiles. In order to increase stiffness of the test table and eliminate/reduce environmental disturbance as much as possible, 25 kg salt sacks are added on the each leg of the test table. The test setup for the Design Point 1 can be seen in the Figure 5.5.

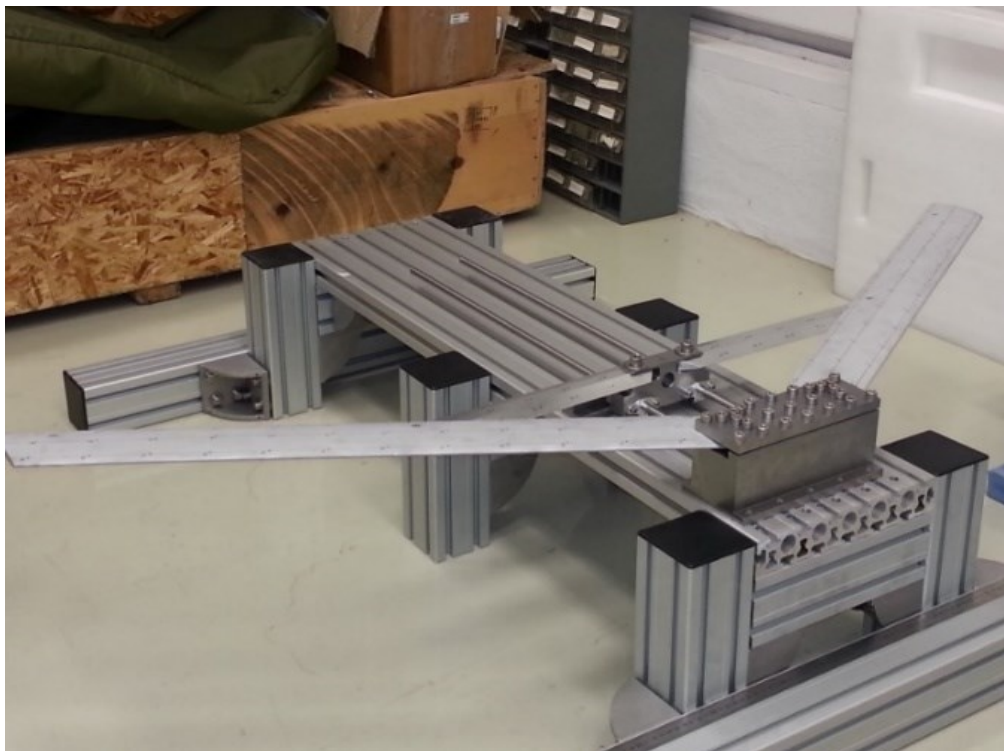


Figure 5.5. Test setup for modal analysis of the Design Point 1

5.3.1 Test Instrumentation

The main tools used in the modal test can be listed as; an accelerometer, a force transducer, an impact hammer, a shaker and a data acquisition system. In this study, experiments are performed by using Brüel and Kjaer vibration measurement systems, the details of the test equipment are listed in the Table 5.1 and their pictures are given in the Figure 5.6, 5.7, 5.8 and 5.9. Pulse Labshop 16.1.0 and ME’scopeVes are used as a main data acquisition and post-processing software respectively.

Table 5.1. Instrumentation and software information

Instrumentation and Software	
Accelerometer	Bruel & Kjaer 4524- Triaxial CCLD piezoelectric [32]
Impact Hammer	Bruel & Kjaer 8202+2646 [32]
Analyzer	Pulse Front-End 3560 [33]
Power Amplifier	Bruel & Kjaer Power Amplifier Type 2712 [34]
Software	Pulse 16.1.0



Figure 5.6. Impact hammer [29]



Figure 5.7. Triaxial accelerometer [29]



Figure 5.8. Data acquisition system [30]



Figure 5.9. Power amplifier [31]

5.4 Modal Tests of the Selected Joined-Wing Configurations

In the experimental part of the thesis, classical modal analyses techniques are applied on two different test configurations. Since the joined-wings are comparatively sophisticated than many basic geometries such as beam-like and plate-like geometries, extraction of modal parameters requires extra attention and due to the mixed modes, sometimes evaluation of mode shapes becomes challenging. For both configurations, first, impact hammer tests are performed then shaker tests are conducted. Modal Test Consultant of PULSE Labshop 16.0 software is used for all tests. In PULSE Labshop, first; test geometries are created, then measurement and excitation points are defined. After analysis setup (number of FFT lines, frequency span, and measurement lengths) is arranged, vibration measurements are completed. Finally, all measurement data is exported to the MeScopeVes software for post processing. Further details of the test procedures are given in the coming impact hammer and shaker test sections. A sample screen of PULSE Labshop is shown in Figure 5.10.

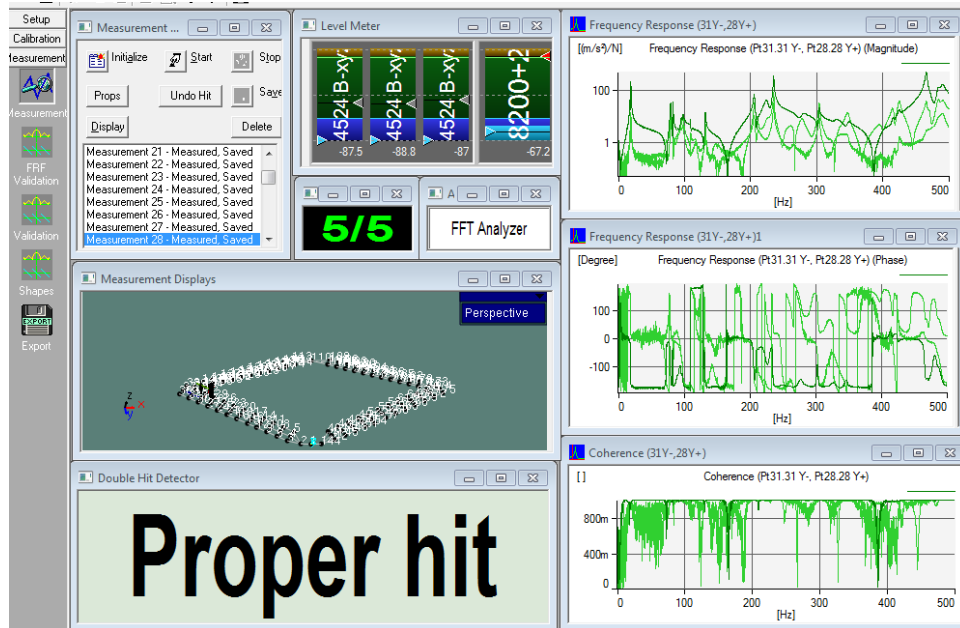


Figure 5.10. Sample screen of PULSE Labshop

5.4.1 Impact Hammer Test

The aim of impact hammer test is to replicate perfect impulse such that the duration of contact time is infinitely small so that all modes of vibration are being excited equally. Impact hammer test is most practical way of modal testing and it requires simple hardware and provides shorter measurement times. Furthermore, it does not affect structure's stiffness characteristics as there is no physical attachment, i.e. stringer of the shaker, between impact hammer and the structure.

In the impact hammer tests, a triaxial (B&K 4524) accelerometer is placed where the ODP levels are relatively higher in order detect all modes of vibration and then the impact hammer is roved on all the points. Since the joined-wings are made of aluminum, soft hammer tips results in double hit, therefore, aluminum tip is used as a hammer tip.

The details of impact hammer tests for selected design points are given below.

Impact Hammer Test for the Design Point 1:

Impact hammer test for the Design Point 1 is conducted between 0-500 Hz and excitation in each point is performed for 5 averages. The total measurement points in this configuration are 101. Figure 5.11 and 5.12 show the measurement mesh of the Design Point 1 in the Pulse Labshop and the corresponding test setup, respectively. The transducer is deliberately placed in the point 2 where the NODP values are relatively smaller. The excitation and the measurement points can be seen in Figure 5.13. In this figure, hammer illustrations represents the locations that will be excited by impact hammer during roving hammer test. The coordinate system, in which red, blue and black colored axes are shown, represents the transducer (i.e. an accelerometer) used during tests. In order to quickly see the measurement outputs, number of FFT lines kept as 1600; however, these arrangements leads to slightly noisy data.

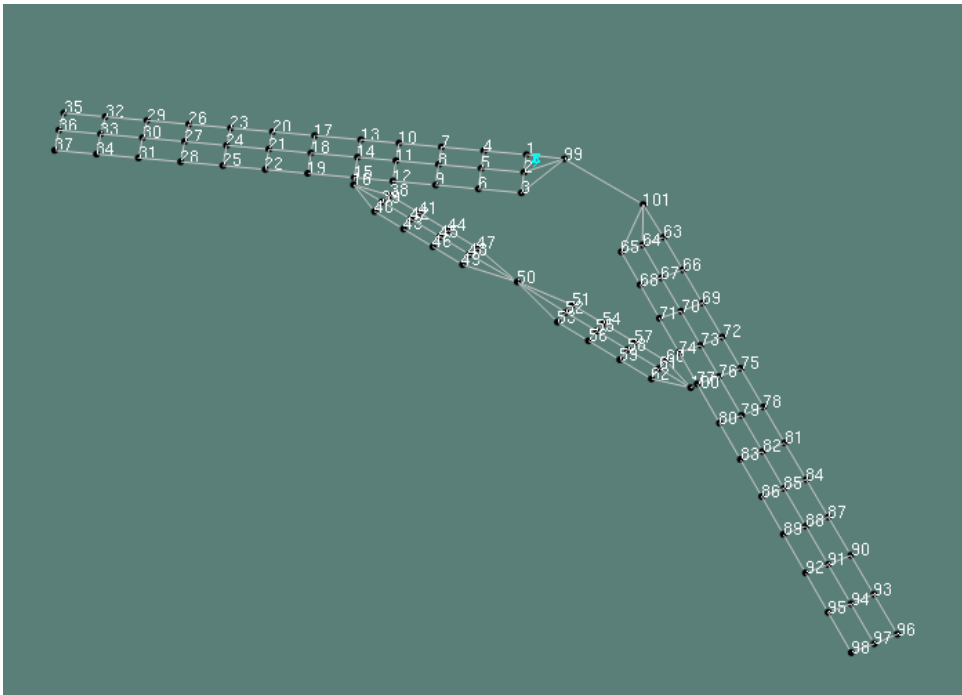


Figure 5.11. Measurement mesh of the Design Point 1

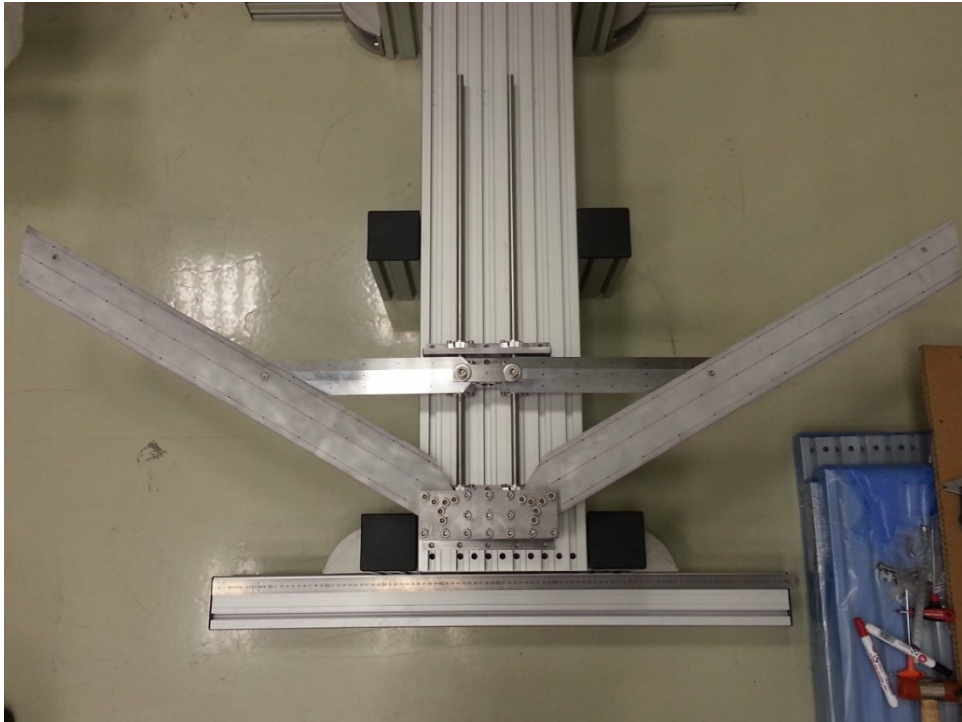


Figure 5.12. Test setup for the Design Point 1

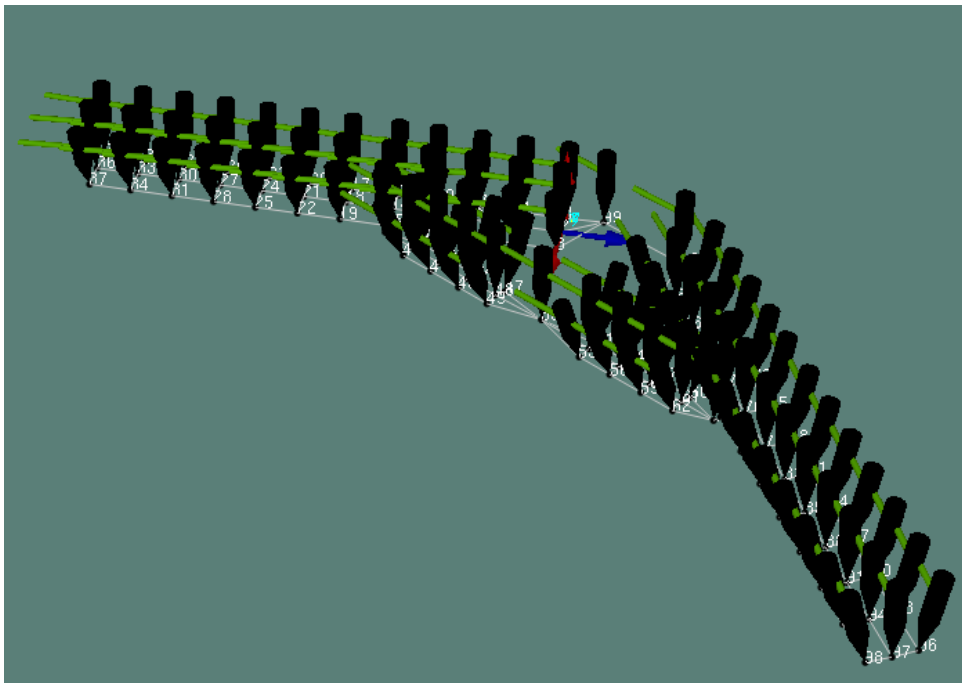


Figure 5.13. Impact excitation and measurement points of the Design Point 1

After the impact hammer test is performed in the Pulse platform, the measured data is exported to ME'scopeVES software for post processing. In the ME'scopeVES, modal parameter estimation is performed to estimate modal parameters of the structure from set of FRFs. For the calculation and plotting of receptance FRFs, a MATLAB script is used. Frequency response curves for 101 different measurements are displayed in Figure 5.14. As it can be seen the FRF curves, the data is noisy and there are many peaks. In order to evaluate whether these peaks belong to structure's modes or not, for each peak curve fitting process is performed. Stability diagrams are also used for locating stable poles. A sample stability diagram can be seen in Figure 5.15. Finally, all founded modes are animated to see the mode shapes. After eliminating local mode shapes, the identified global mode shapes and their definitions are given in the Figure 5.16 and Table 5.2, respectively. The comparison have been made between FEA and the impact hammer test results and presented in Table 5.3. The results corresponding to the first four mode are in good agreement with small deviations. However, the fifth and sixth modes could not be detected. The reason for this could be the fact that since these modes is in plane-modes, the modes could not excited with existing direction of the forcing.

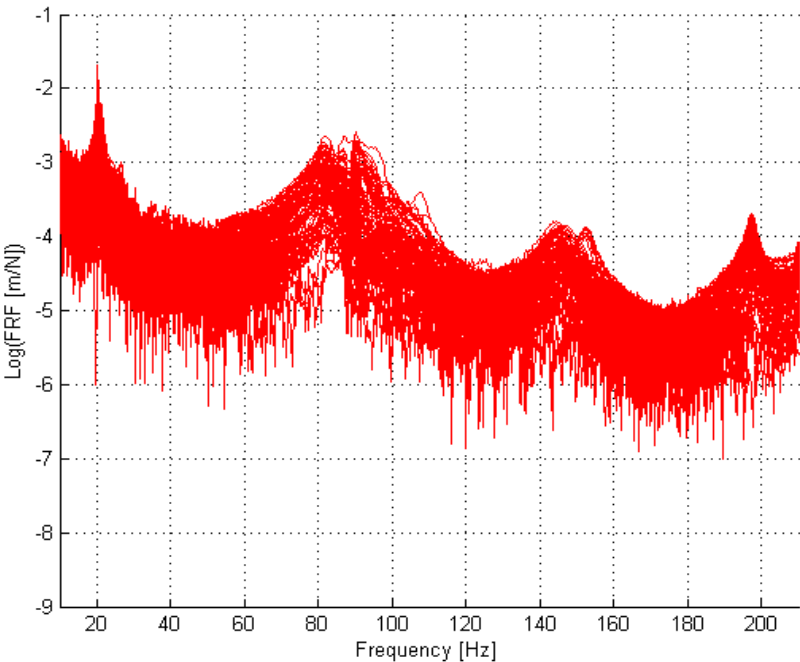


Figure 5.14. FRF plots of impact hammer test for the Design Point 1

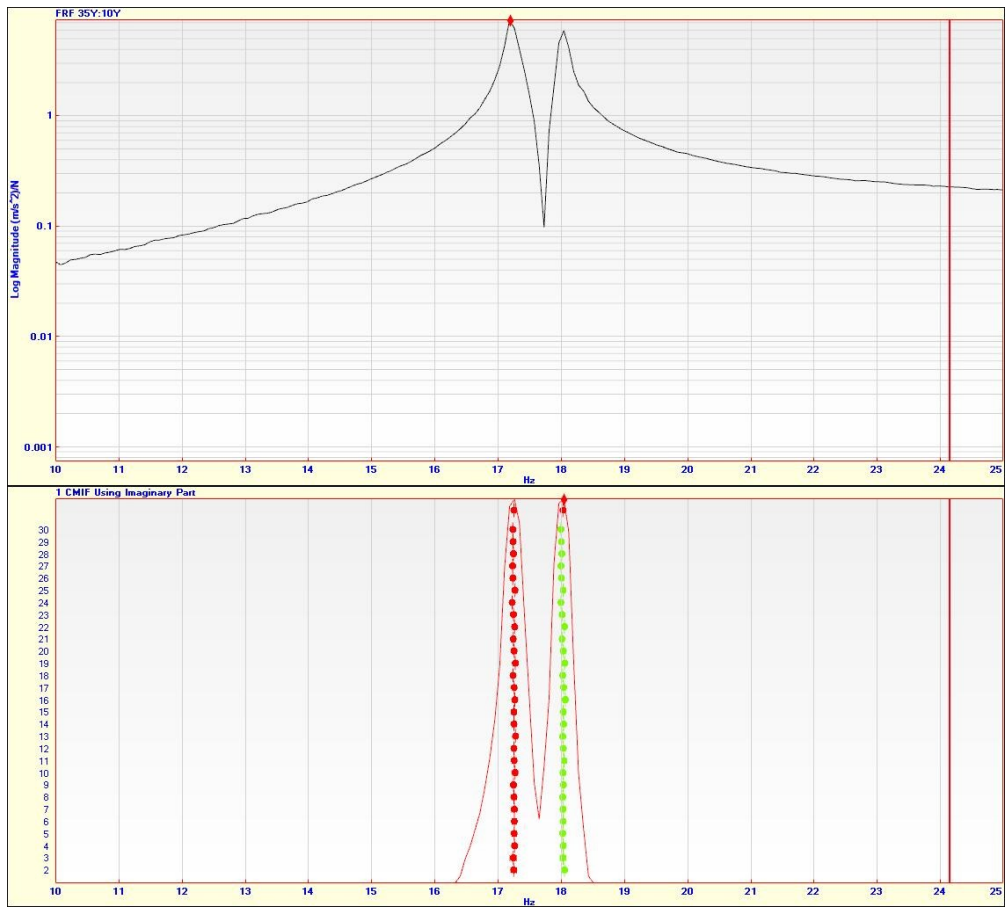


Figure 5.15. Sample stability diagram for the first two modes of impact hammer test for the Design Point 1 with zoom view

Table 5.2. The first six vibration modes of the Design Point 1 from impact hammer test

Mode	Frequency (Hz)	Description of the free vibration modes
1	20.20	Front wing first anti-symmetric out-of-plane bending
2	21.30	Front wing first symmetric out-of-plane bending
3	82.60	Front wing second out-of-plane anti-symmetric bending, Aft wing first out-of-plane anti-symmetric bending
4	89.90	Front wing second symmetric out-of-plane bending, Aft wing first symmetric out-of-plane bending
5	N/A	Front wing first anti-symmetric in-plane bending, Aft wing second symmetric out-of-plane bending
6	N/A	Front wing first symmetric in-plane bending, Aft wing second anti-symmetric out-of-plane bending

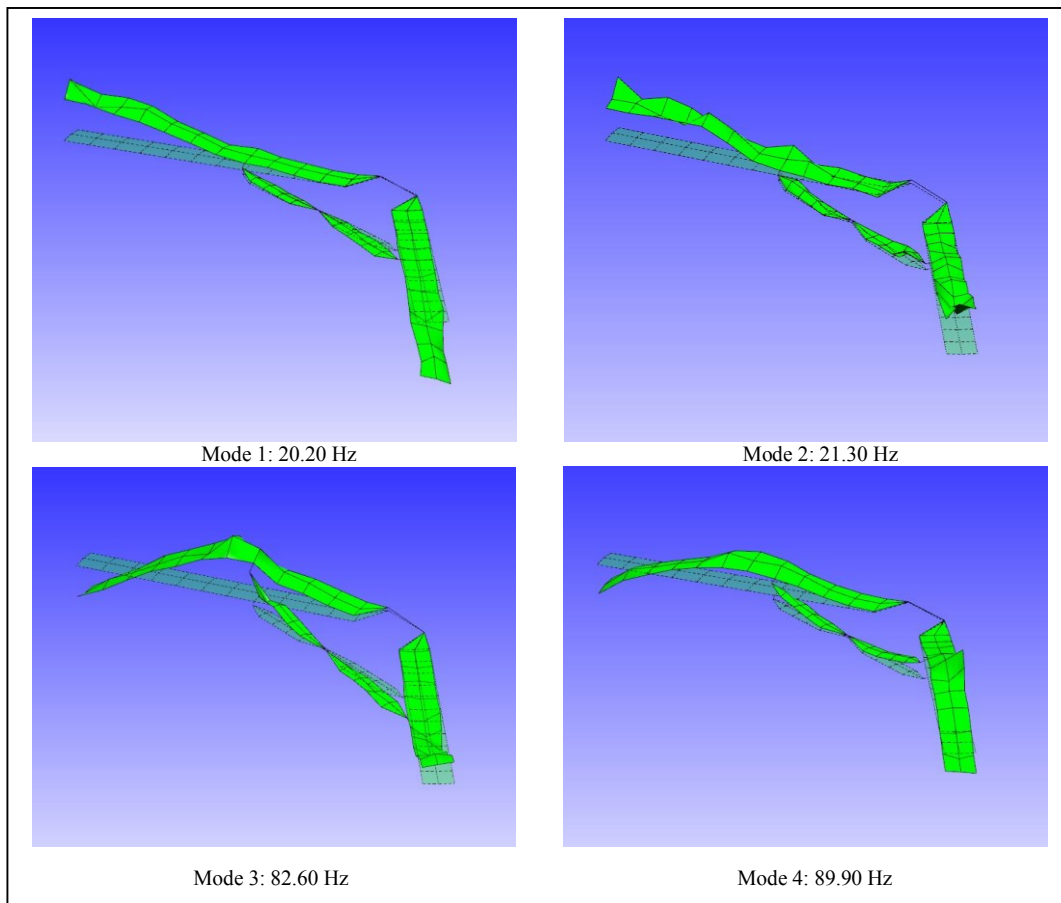


Figure 5.16. The first four mode shapes of the Design Point 1 from impact hammer test

Table 5.3. Comparison of FEA and impact hammer test results for the Design Point 1

Mode	Frequencies [Hz]		Difference [%]
	Finite Element Analysis	Impact Hammer Test	
1	20.89	20.20	-3.31
2	20.98	21.30	+1.54
3	84.84	82.60	-2.64
4	85.19	89.90	+5.53
5	192.95	-	-
6	197.25	-	-

Impact Hammer Test for the Design Point 2:

Impact hammer test procedure for the Design Point 2 is mainly similar to the previous test. The main difference between this test and the previous one comes only from the geometry change. This configuration consists of 144 measurement points which are shown in Figure 5.17. Another difference is that the transducer is placed at point number 31 where the ODP values are relatively higher. In order to increase the resolution of the measurement, numbers of FFT lines are also set as 6400. Illustrations for excitation and measurement points, corresponding test setup, the frequency response curves for 144 different measurements and the pictorial illustration of the mode shapes for Design Point 2 are given in Figure 5.18, 5.19, 5.20 and 5.21, respectively. The definitions of the first six modes are summarized in Table 5.4. The comparison has been made between FEA and the impact hammer test results and given in the Table 5.5. The comparison results point out that all the natural frequency values calculated from FEA and the ones from the impact hammer test are in close agreement except the “Front wing torsion-bending mixed, aft wing second symmetric out-of-plane bending” modes.

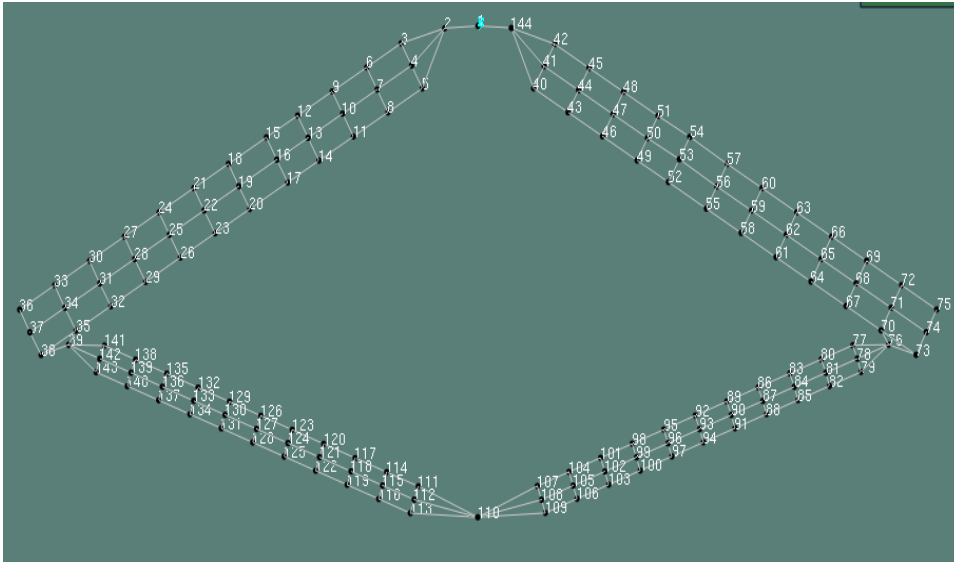


Figure 5.17. Measurement mesh of the Design Point 2

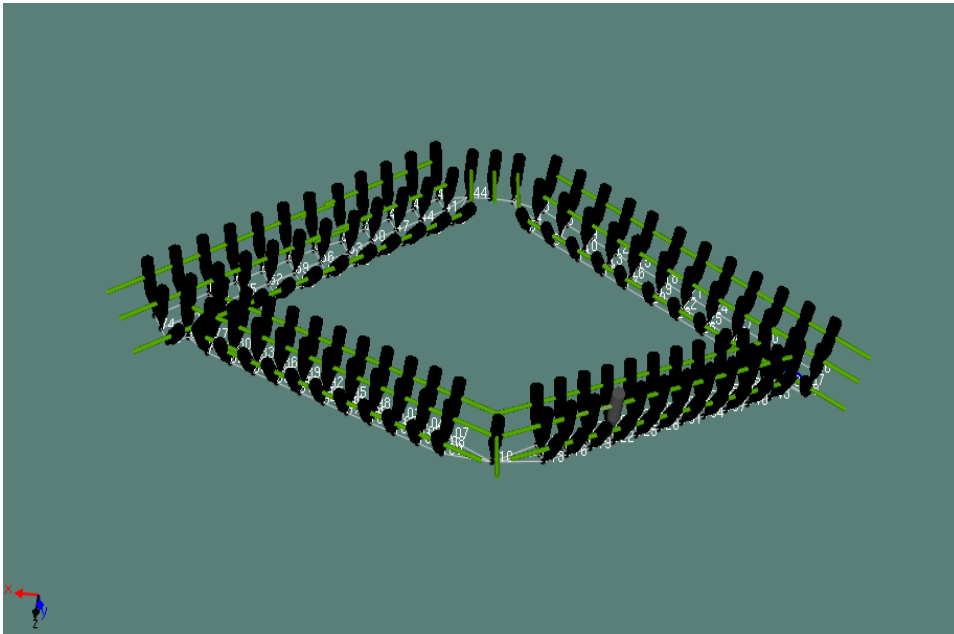


Figure 5.18. Impact excitation and measurement points of the Design Point 2

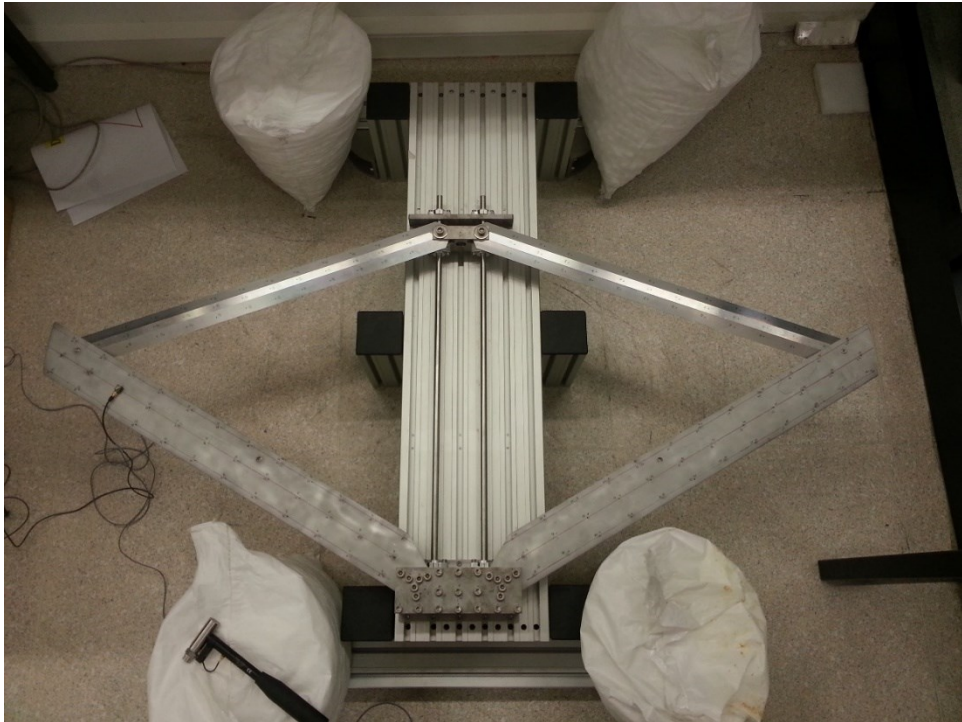


Figure 5.19. Test setup for impact hammer test of the Design Point 2

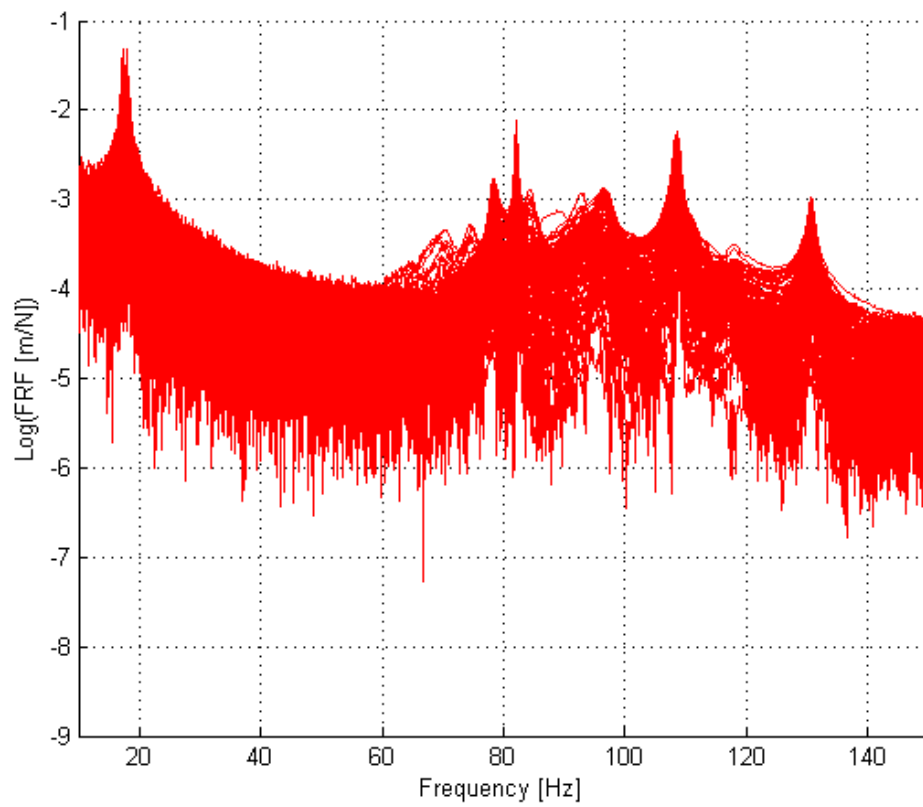


Figure 5.20. FRF plots of the impact hammer test for the Design Point 2

Table 5.4. First six vibration modes of the Design Point 2 from impact hammer test

Mode	Frequency (Hz)	Description of the free vibration modes
1	17.30	Front wing first out-of-plane anti-symmetric bending, Aft wing anti-symmetric bending
2	18.00	Front wing first symmetric bending, Aft wing symmetric bending
3	78.40	Front wing second anti-symmetric out-of-plane bending, Aft wing mixed
4	82.10	Front wing second symmetric out-of-plane bending, Aft wing mixed
5	109.00	Front wing torsion-bending mixed, Aft wing second anti-symmetric out-of-plane bending
6	131.00	Front wing torsion-bending mixed, Aft wing second symmetric out-of-plane bending

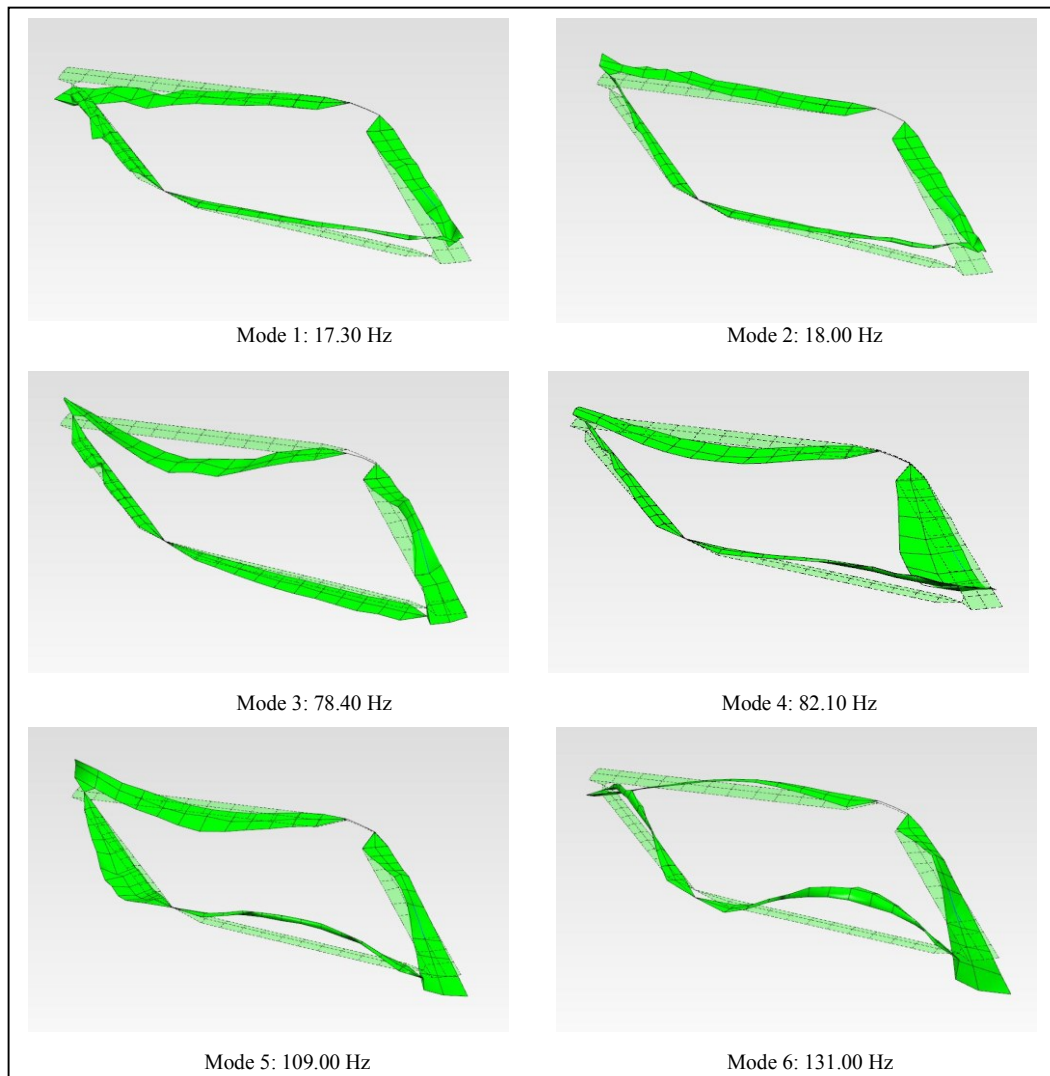


Figure 5.21. The first six mode shapes of the Design Point 2 from impact hammer test

Table 5.5. Comparison of FEA and impact hammer test results for the Design Point

2

Mode	Frequencies [Hz]		Difference [%]
	Finite Element Analysis	Impact Hammer Test	
1	18.00	17.30	-3.89
2	17.99	18.00	+0.06
3	78.86	78.40	-0.58
4	78.89	82.10	+4.07
5	114.60	109.00	-4.89
6	108.54	131.00	+20.69

5.4.2 Shaker Tests with Random Excitation

From the theoretical standpoint, it may seem that there is no difference between shaker and impact test. However in the practical standpoint there are some differences. The disadvantages of shaker test can be listed as the potential stiffening effects of the shaker/stringer arrangement, roving mass effect, etc.[35] However, in many cases shaker test has an advantage over an impact test such as reducing the effect of nonlinear response, providing better signal to noise ratio, eliminating overload problems, providing more consistent data, etc. [36] In the shaker tests, random signals are generated and given to the test structure. In order to reduce the potential stiffening effects of the stringer arrangements, it is attached to the point where the NODP values are relatively low.

Shaker Test for the Design Point 1:

Shaker test for the Design Point 1 is conducted between 0-500 Hz and measurement in each point is performed for 26 averages. Figure 5.23 shows the test setup with shaker arrangement. In this test, the measurement procedure is mainly similar to the impact hammer test, however, instead of impact hammer, a response transducer is roved to 101 points shown in Figure 5.22. Numbers of FFT lines are set as 6400. After the measurements are finished, the same post processing procedure as impact hammer

tests is followed and applied. The frequency response curves for 101 different measurement are presented in Figure 5.24. The definitions for the first six modes and their pictorial illustration are summarized and showed in Table 5.6 and Figure 5.25, respectively. Unlike the impact hammer test, for these configurations, the sixth mode “Front wing first symmetric in-plane bending, aft wing second anti-symmetric out-of-plane bending” is founded in this test with almost zero error. Furthermore, it can be seen from the Figure 5.24 that the noise level compared to the Figure 5.14 is highly reduced. Finally, a comparison has been made between FEA and the shaker test results and given in the Table 5.7 and as it can be seen from this table that the most of the natural frequency values calculated from FEA and impact hammer test are in close agreement.

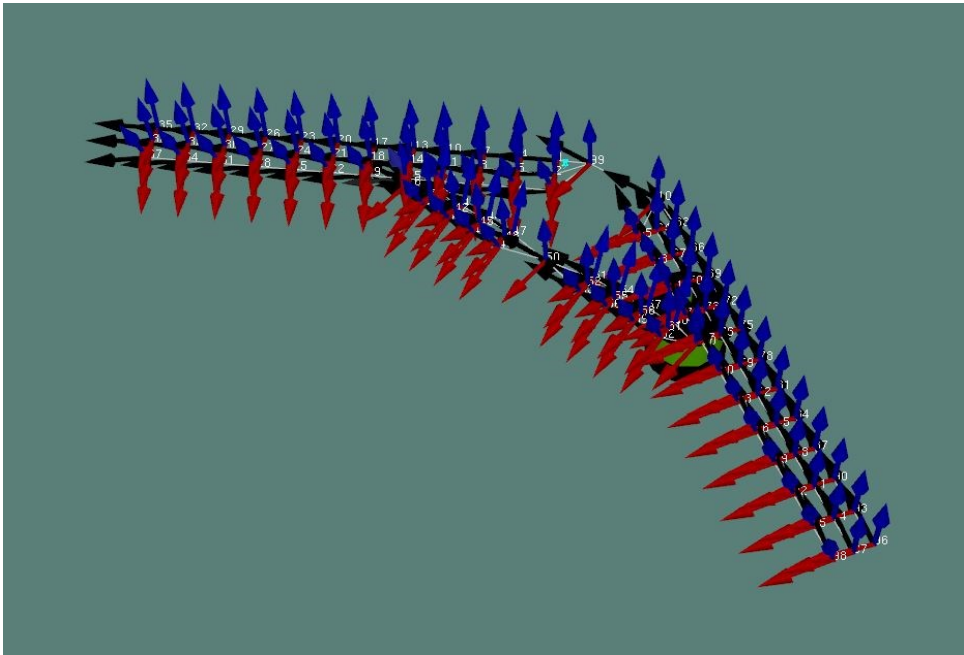


Figure 5.22. Shaker excitation and measurement points of the Design Point 1



Figure 5.23. Test setup for shaker test of the Design Point 1

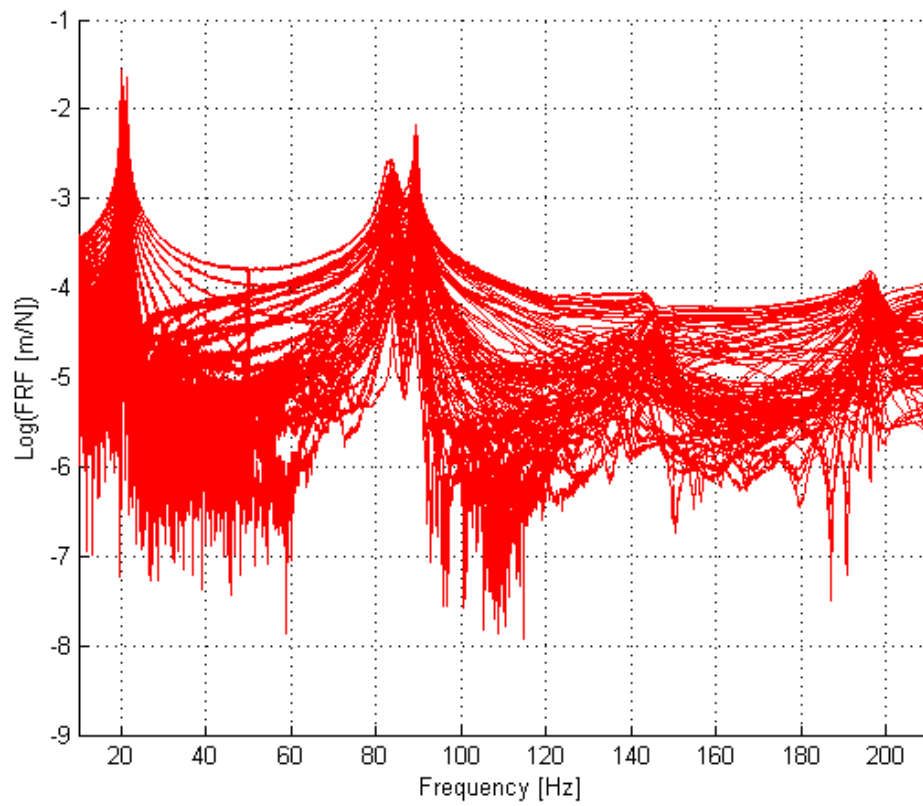


Figure 5.24. FRF plots of the shaker test for the Design Point 1

Table 5.6. First six vibration modes of the Design Point 1 from shaker test

Mode	Frequency (Hz)	Description of the free vibration modes
1	20.20	Front wing first anti-symmetric out-of-plane bending
2	21.40	Front wing first symmetric out-of-plane bending
3	83.40	Front wing second out-of-plane anti-symmetric bending, Aft wing first out-of-plane anti-symmetric bending
4	89.40	Front wing second symmetric out-of-plane bending, Aft wing first symmetric out-of-plane bending
5	-	Front wing first anti-symmetric in-plane bending, Aft wing second symmetric out-of-plane bending
6	197.00	Front wing first symmetric in-plane bending, Aft wing second anti-symmetric out-of-plane bending

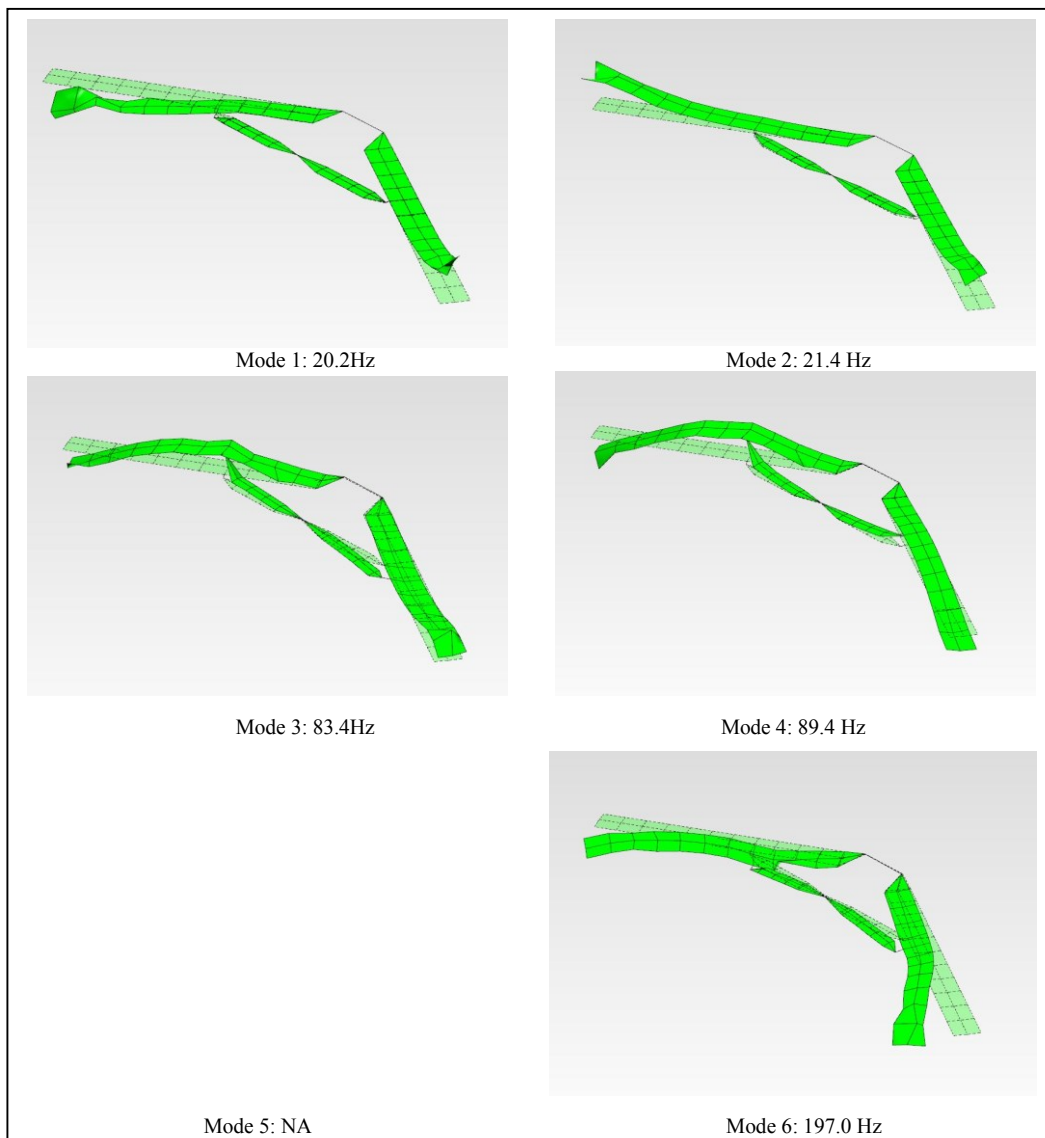


Figure 5.25. The first six mode shapes of the Design Point 1 from shaker test

Table 5.7. Comparison of FEA and shaker test results for the Design Point 1

Mode	Frequencies [Hz]		Difference [%]
	Finite Element Analysis	Shaker Test	
1	20.89	20.20	-3.31
2	20.978	21.40	+2.01
3	84.842	83.40	-1.70
4	85.189	89.40	+4.94
5	192.950	-	-
6	197.249	197.00	-0.13

Shaker Test for the Design Point 2:

Shaker test procedure and the analyses setup for the Design Point 2 is same as the previous shaker test. Pictorial illustrations for this configuration such as shaker excitation and measurement points, the test setup with shaker arrangement, the frequency response curves for 144 different measurements and first six mode shapes can be seen in Figures 5.26, 5.27, 5.28 and 5.29, respectively. The definitions of the first six modes are also summarized in Table 5.8. Lastly, a comparison has been made between FEA and the shaker test results and summarized in the Table 5.9. The comparison results show that the FEA and test outcomes are in close agreement.

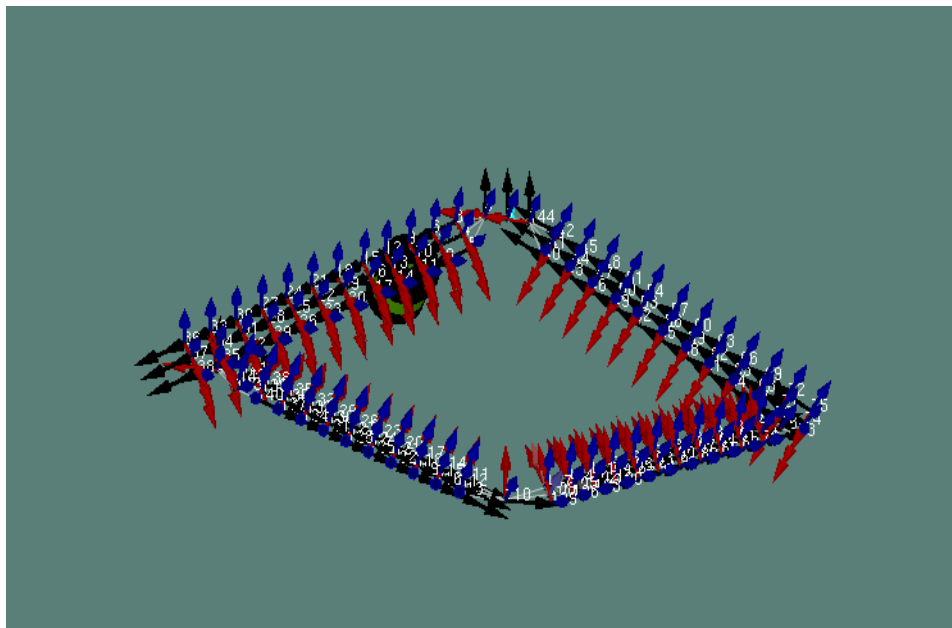


Figure 5.26. Shaker excitation and measurement points of the Design Point 2



Figure 5.27. Test setup for shaker test of the Design Point 2

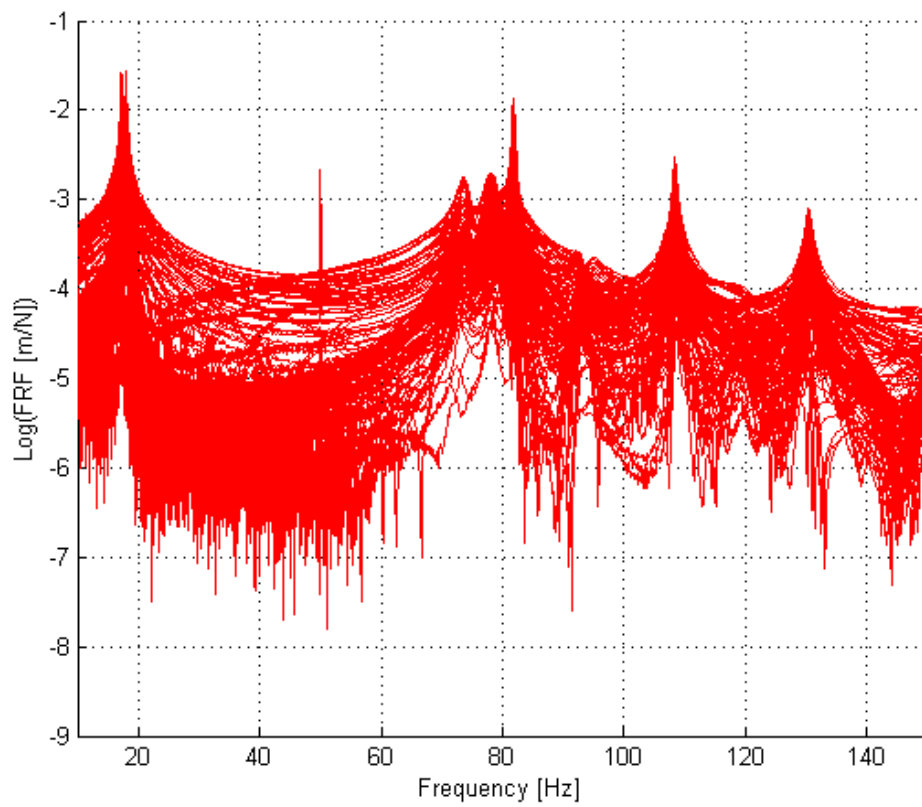


Figure 5.28. FRF plots of the shaker test for the Design Point 2

Table 5.8. First six vibration modes of the Design Point 2 from shaker test

Mode	Frequency (Hz)	Description of the free vibration modes
1	17.30	Front wing first out-of-plane anti-symmetric bending, Aft wing anti-symmetric bending
2	18.00	Front wing first symmetric bending, Aft wing symmetric bending
3	73.50	Front wing second anti-symmetric out-of-plane bending, Aft wing mixed
4	81.90	Front wing second symmetric out-of-plane bending, Aft wing mixed
5	108.00	Front wing torsion-bending mixed, Aft wing second anti-symmetric out-of-plane bending
6	131.00	Front wing torsion-bending mixed, Aft wing second symmetric out-of-plane bending

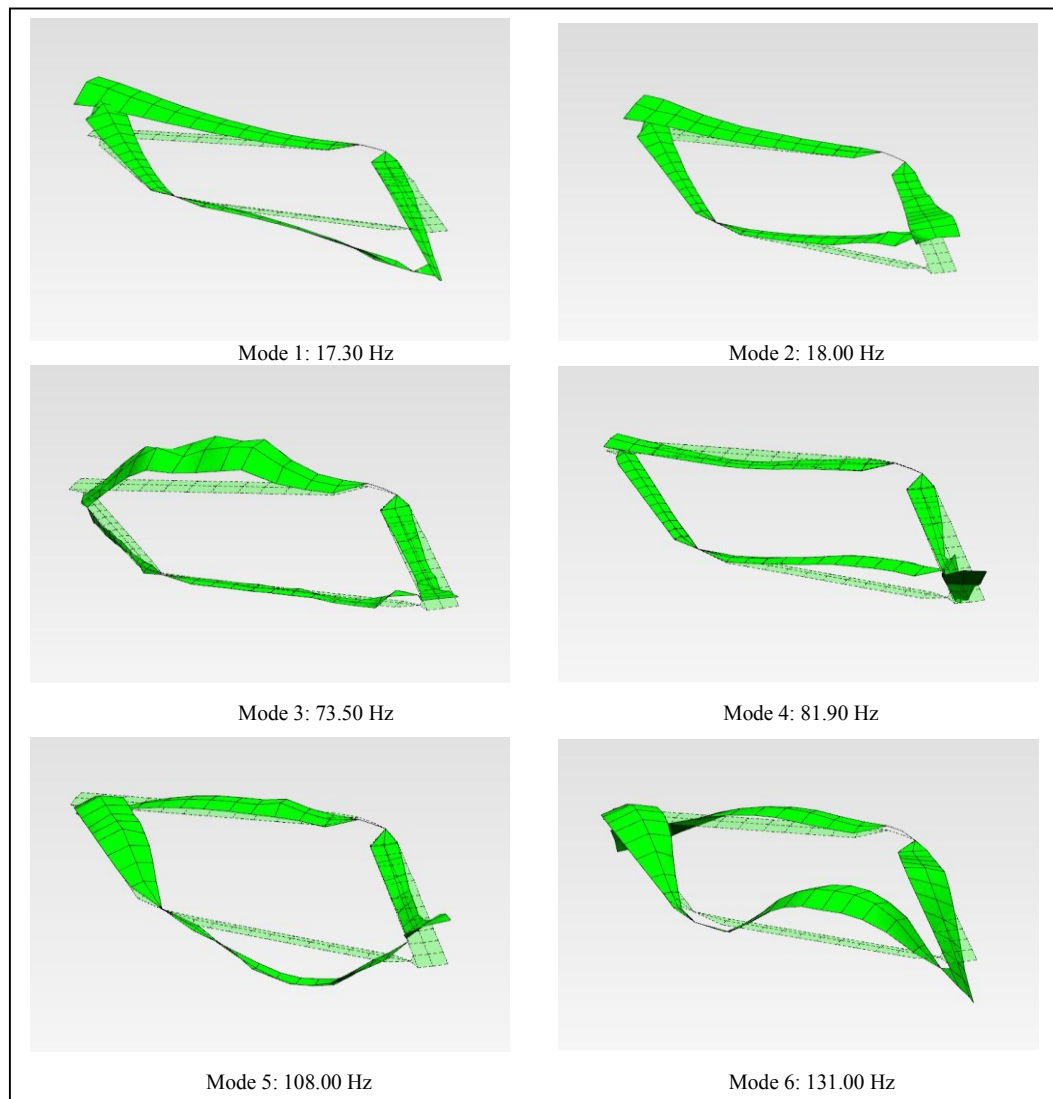


Figure 5.29. The first six mode shapes of the Design Point 2 from shaker test

Table 5.9. Comparison of FEA and shaker test results for the Design Point 2

Mode	Frequencies [Hz]		Difference [%]
	Finite Element Analysis	Shaker Test	
1	18.00	17.30	-3.89
2	17.99	18.00	+0.06
3	78.86	73.50	-6.80
4	78.89	81.90	+3.82
5	114.60	108.00	-5.76
6	108.54	131.00	+20.69

5.5 Discussion and Conclusions

In this chapter, in order to investigate dynamic characteristics of the two selected joined wing configurations, namely; selected Design Point 1 and selected Design Point 2, impact hammer and shaker tests are performed. In each test section, modal parameters of the related structure are extracted and these results are compared with FEA results calculated in the Chapter 4. In FRF plots, there are very sharp peaks at 50 Hz, the reason is the city electricity coupling since current is practically 50 Hz in Turkey. The comparisons show that FEA and modal test results are in close agreement. It can be also said that FEA results are validated via experimental modal analyses.

CHAPTER 6

3-D AERODYNAMIC MODELLING AND ANALYSES OF THE JOINED-WING CONFIGURATIONS

6.1 Introduction

In order not to model the lift and the drag forces by in terms of only single concentrated force, the aerodynamic analysis is performed. Thus, present chapter focuses on the aerodynamic simulations in order to efficiently calculate flight loads on the joined-wings. The application of Computational Fluid Dynamics (CFD) in static aero elastic simulations has the advantage of being more accurate over the linear methods such as the double lattice methods. The usage of CFD methods, coupled with a linear structural model, is currently the state-of-the-art for determining external loads with sufficient accuracy [12].

In the light of the mentioned advantages, 3D CFD analyses were carried out by using ANSYS® Fluent for half –symmetric models of the joined-wings. The joined-wing configurations are parametrically investigated for the outputs such as lift (L), drag (D), lift-to-drag ratio (L/D). In addition to the geometric design variables (joint location and aft wing sweep angle), Mach number and angle of attack are defined as input design variables. The Mach number and the angle of attack (AOA) are allowed to change from 0.60 to 0.95 and from -2° to 10° , respectively.

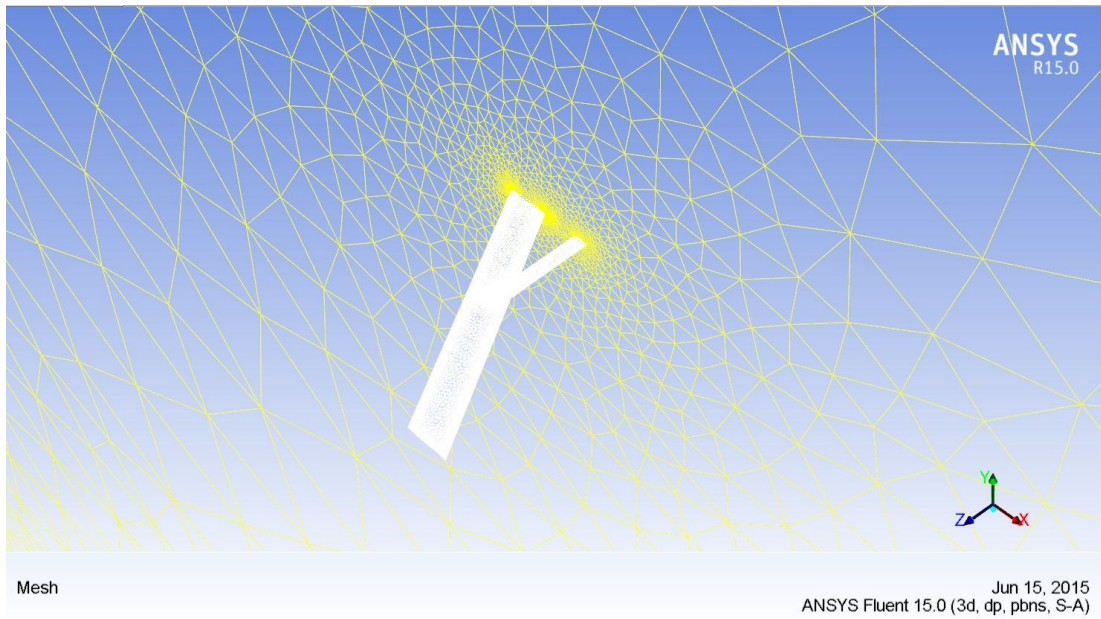
The details of the 3D aerodynamic analyses are explained and illustrated for the selected design configurations in the following sections.

6.2 3-D CFD Analysis of Selected Joined-Wing Configurations

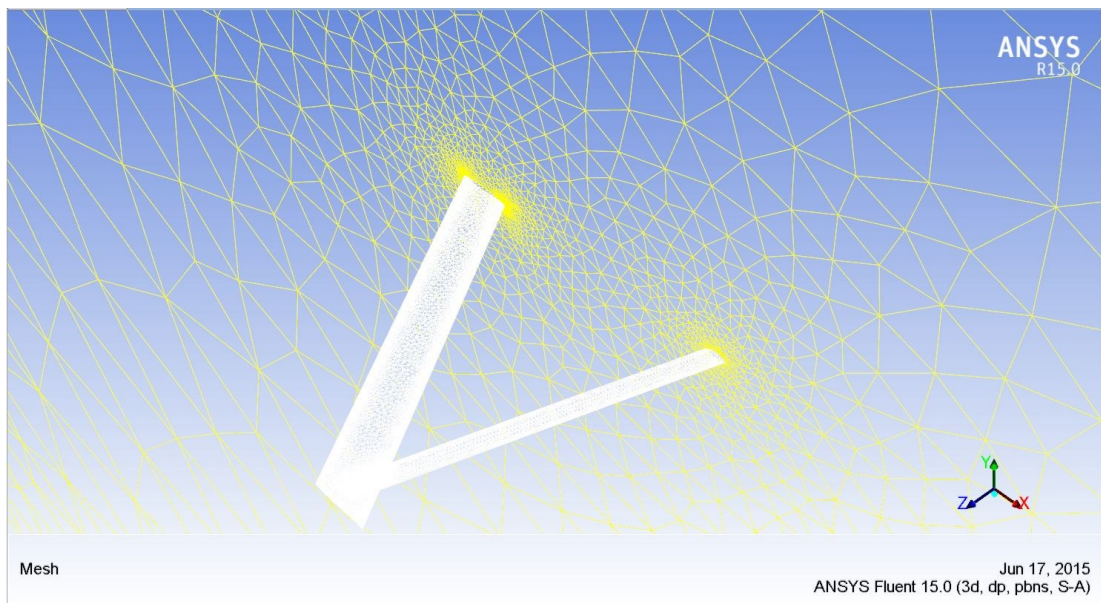
CFD simulations are performed to predict the aerodynamic loads on the structure. In order to capture flow nonlinearities and to predict associated drag in a transonic flow, a Reynolds-Averaged Navier-Stokes (RANS) model with a one-equation Spalart-Allmaras turbulence model [37], which commonly used for transonic aerodynamic applications for the turbulence closure [38], is used in the analyses. A commercial CFD code, Fluent [39], is used with implicit, upwind, second-order accurate, pressure-based solver. NASA Super critical airfoil-SC(2) 1010 (due to its high drag divergence Mach Number and good transonic behavior) [40] and a hexagonal cross section are selected for the front wing and the aft wing cross sections, respectively.

6.2.1 Mesh Generation

The half symmetric parametric 3D CAD models of the joined-wing configurations are created in ANSYS® Design Modeler [41]. To generate mesh for the flow field ANSYS Meshing [42], a commercial mesh generation tool, is used. The mesh quality has a considerable impact on the solution, because low quality meshes can induce; convergence difficulties, bad physic description and non-converged solution. To avoid these problems, the mesh quality has to be checked carefully. If the mesh characteristics and growth were not controlled, it is possible to get highly skewed elements. Hence, in order to tackle these problems the advance size functions are used. In this study, created meshes comprise tetrahedral and prismatic elements. Average number of elements used in the CFD computation is approximately 1.2 million. Inflation control is added to capture the boundary layer region for any wall-bounded turbulent flows. In the inflation grids, prismatic elements are used in the vicinity of the wing surfaces to increase the resolution and the mesh quality. Grid independence is tested by performing steady state computations with different number of elements. Furthermore, the orthogonal quality criterion is checked and if the orthogonal quality was less than 0.01, the grid is improved to increase it. Typical meshes for flow field are shown in Figures 6.1, 6.2, 6.3 and 6.4. Boundary condition zones are also summarized in the Table 6.1.

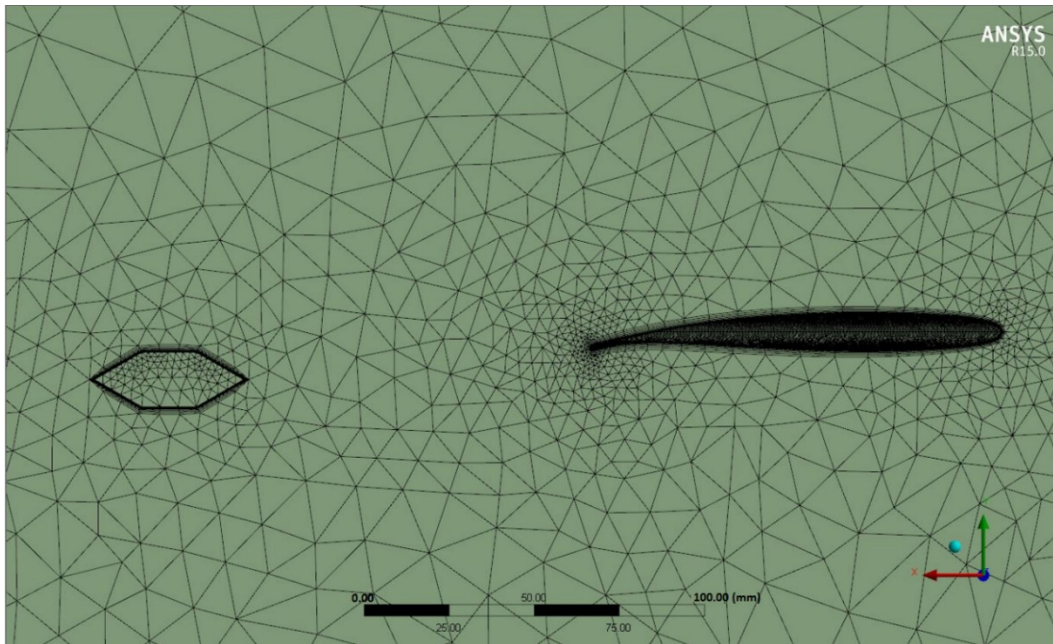


(a)

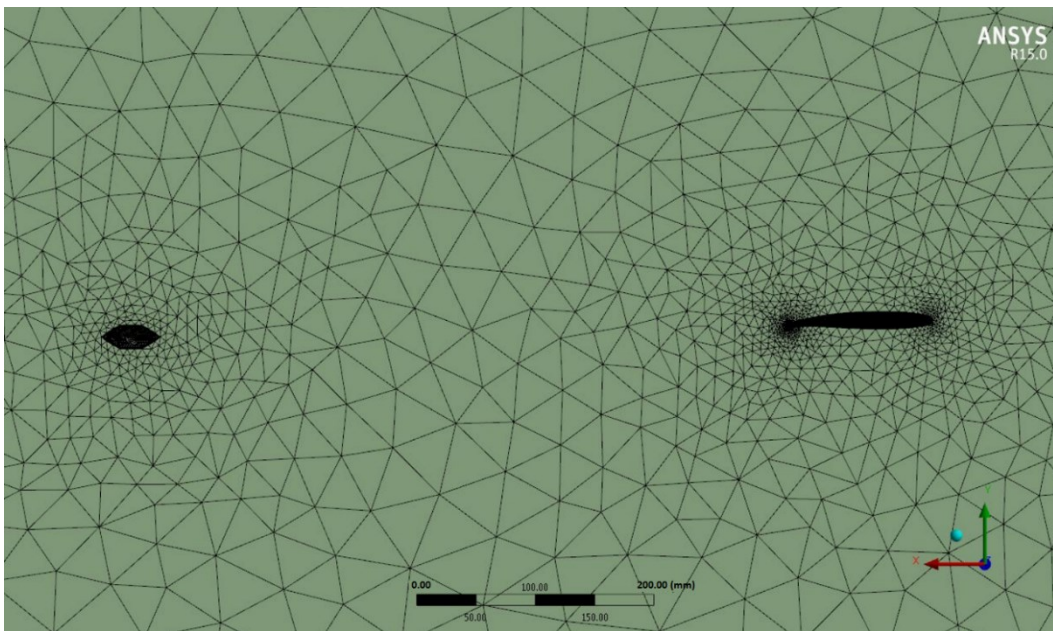


(b)

Figure 6.1. Surface meshes on joined-wing surfaces and symmetry plane (a) Design Point 1 (b) Design Point 2



(a)



(b)

Figure 6.2. Detailed mesh view around wing cross-sections (a) Design Point 1 (b) Design Point 2

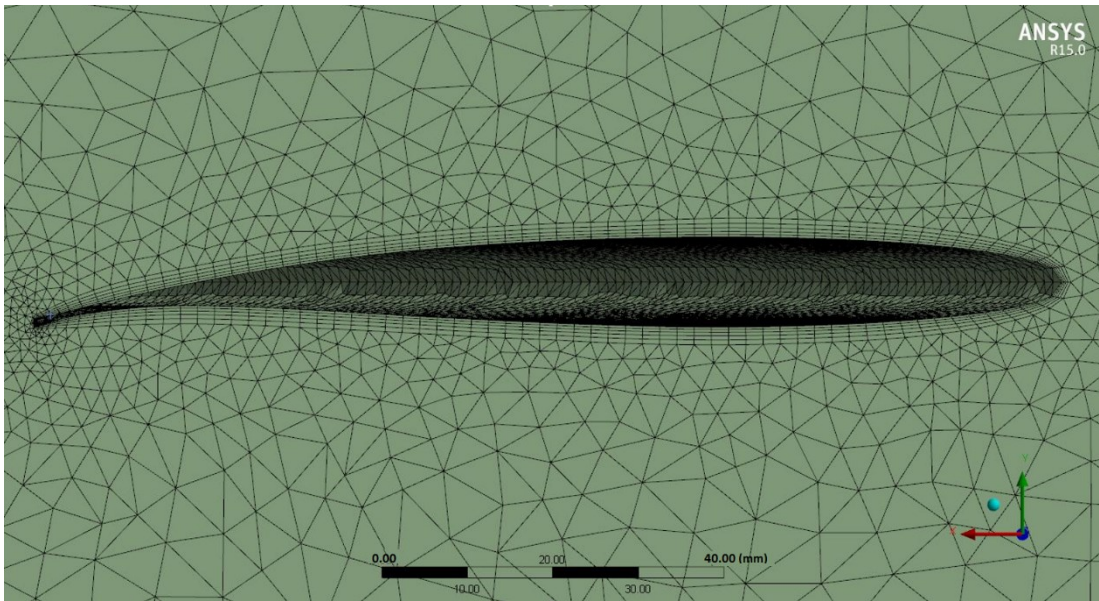


Figure 6.3. Inflation layers around front wing

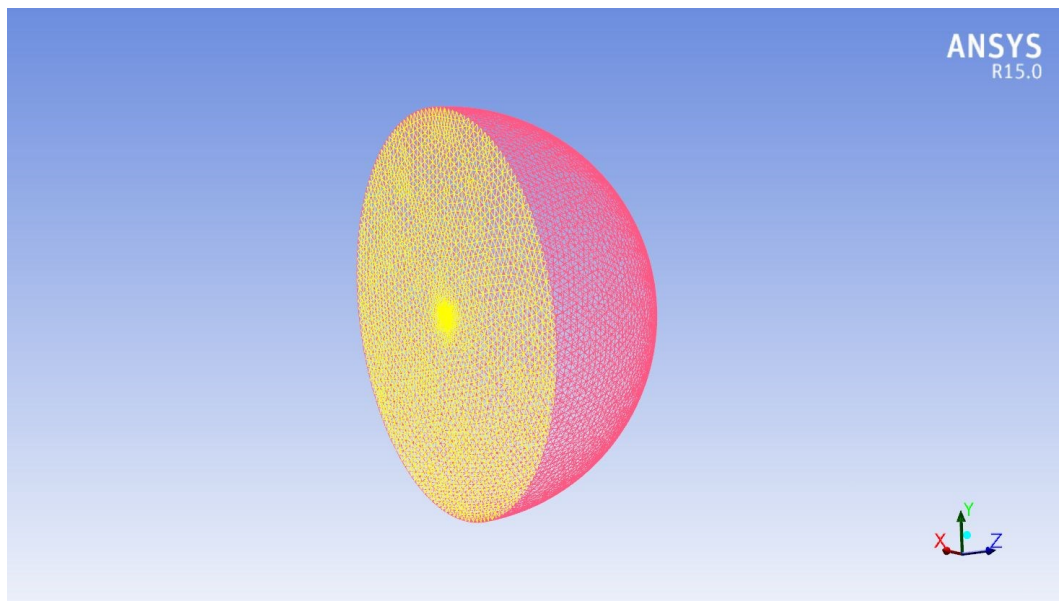


Figure 6.4. Typical mesh for fluid domain

Table 6.1. Boundary conditions

Face	Boundary Condition
Curved Surface of the Semi-Sphere	Pressure Far Field
Flat Surface of the Semi-Sphere	Symmetry
Surfaces of the joined-wings	Wall

6.2.2 Fluent Setup

ANSYS® Fluent is used to model the incompressible flow and the solution is performed using the following analysis scheme:

1. ANSYS® Fluent 3ddp (3D Double Precision) is selected as a solution type.
2. Pressure based solver is selected with implicit formulation and steady time options.
3. Spalart- Allmaras turbulence model is chosen for turbulence closure. In the material definition air is selected with ideal gas density properties.
4. Solution is established at variable Mach and the angle of attacks.
5. Pressure far field is defined for the hybrid initialization.
6. Number of iterations is defined as 1000.
7. Convergence criterion is selected as 10^{-5} to monitor residuals.

Although, pressure based approach is developed for low-speed incompressible flows originally and density based approach is mainly used for high speed compressible flows, recently both methods are extended and reformulated to solve and operate for a wide range of flow conditions beyond their traditional intent. In the recent study, the pressure based approach is tested on successfully on a number of scenarios, for instance, transonic and supersonic flows, low Mach number flows with low and high viscosity [43].

6.2.3 Convergence Monitoring

The residual plots can display when the residual values are reached to the specified tolerance. Usually the residuals should decrease at least three orders of magnitude to obtain accurate results. The convergence monitoring graph showing the relation between the momentum velocity residuals and the iteration number is given in Figures 6.5 and 6.6. To determine convergence criteria is satisfied, it is expected to velocity residuals to go below 10^{-3} [39].

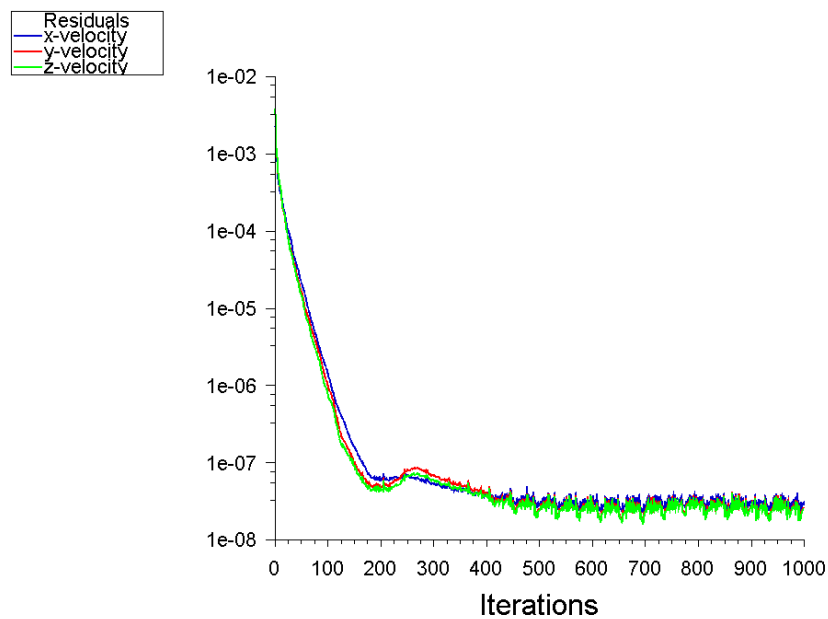


Figure 6.5. Change of scaled residuals vs. iteration number for pressure based solver

6.3 Analysis Results

After the fluid solver reached to a convergence, the results are presented as static pressure contour plots. Figures 6.6 and 6.7 show the static pressure distribution for the upper and lower surfaces of the selected Design Point 1 at 0.75 Mach, 0 degree AOA, respectively. Figures 6.8 and 6.9 show the static pressure distribution for the upper and lower surfaces of the selected Design Point 2 at 0.75 Mach, 0 degree AOA, respectively.

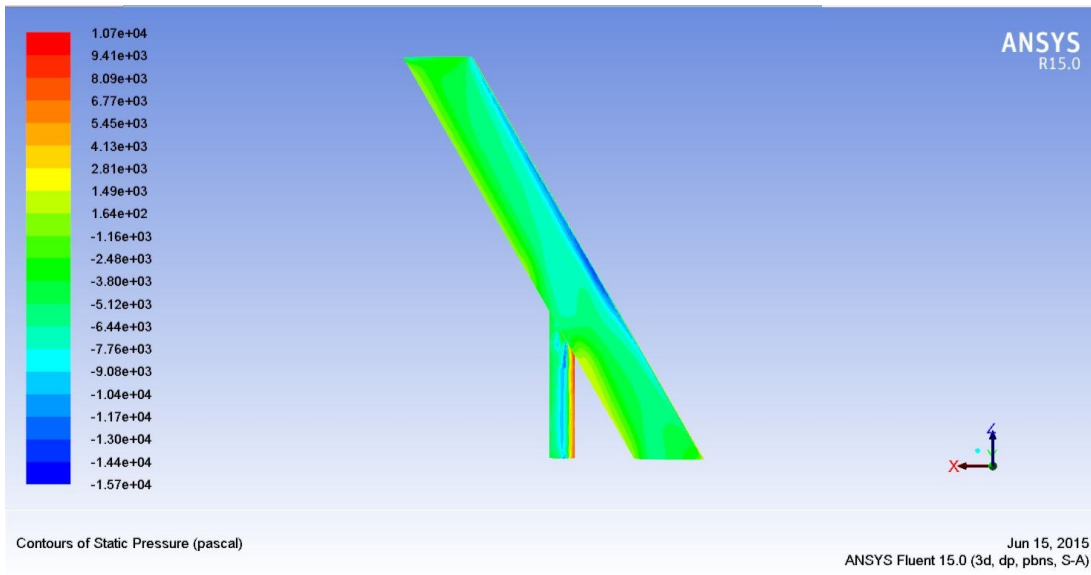


Figure 6.6. Upper surface static pressure contours of the Design Point 1 [Pa]

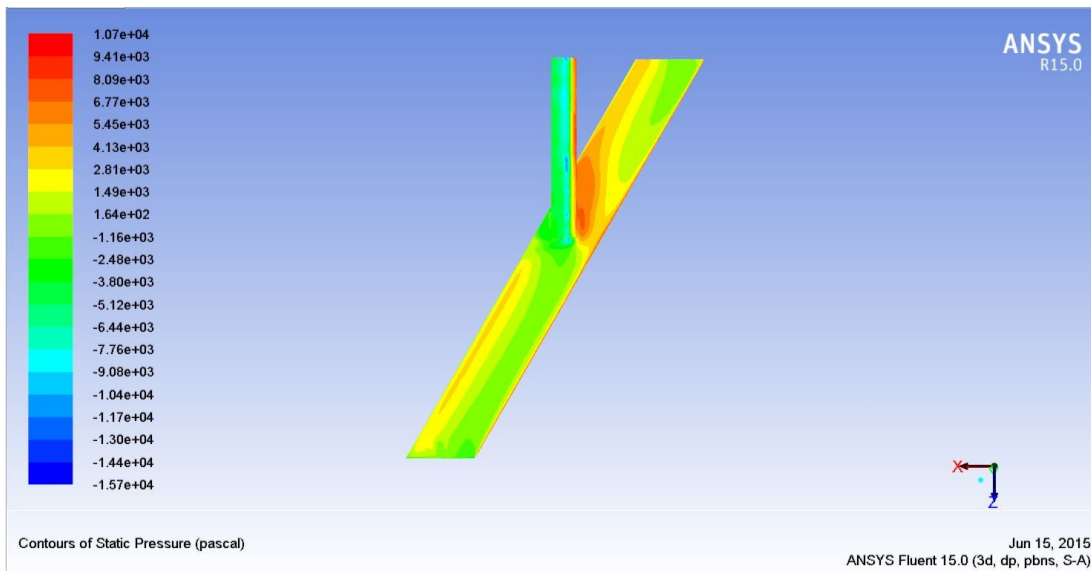


Figure 6.7. Lower surface static pressure contours of the Design Point 1 [Pa]

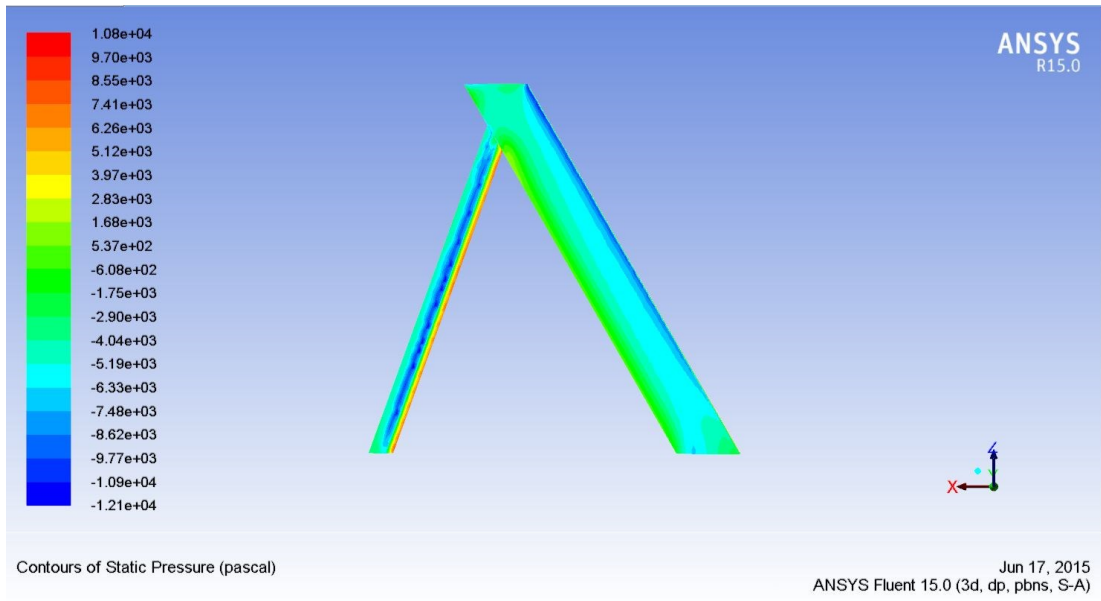


Figure 6.8. Upper surface static pressure contours of the Design Point 2 [Pa]

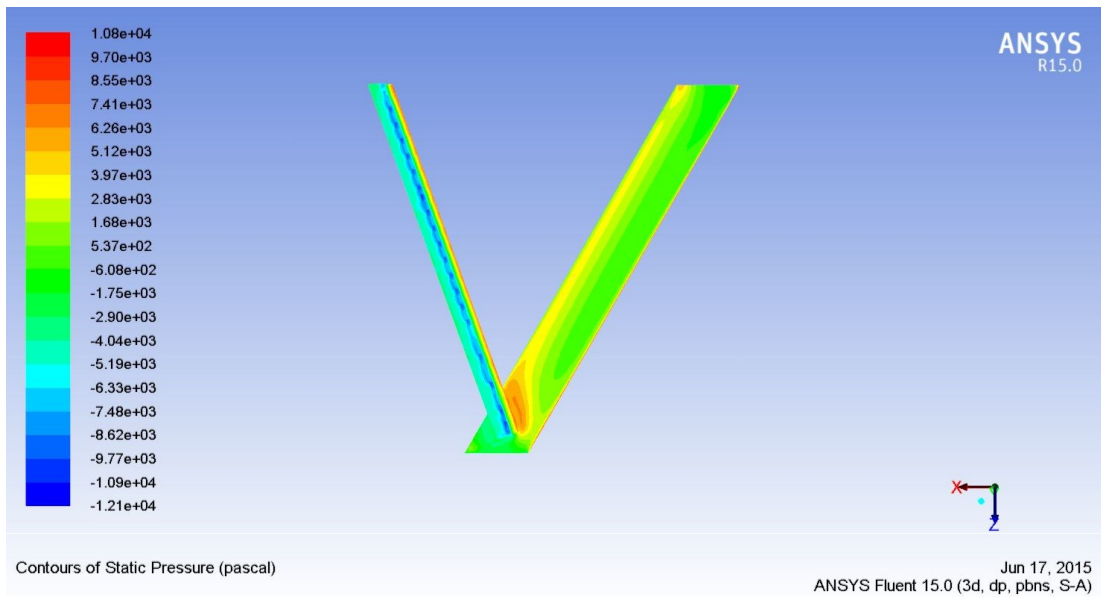


Figure 6.9. Lower surface static pressure contours of the Design Point 2 [Pa]

As it can be clearly seen from static pressure contour plots, there is an increase in the pressure values especially in the leading edge and around joint location. The red contours indicate the highest pressure value in the joined-wings.

In order visualize the flow of massless particles through the joined-wing sections, path line plots are generated. The particles are released from far field and the intensity of the particles increased at center of the wing surfaces. Figures 6.10 and 6.11 present the path line plots of the Design Point 1 and 2, respectively. Vortex generations behind the aft wing can also be seen from these plots.

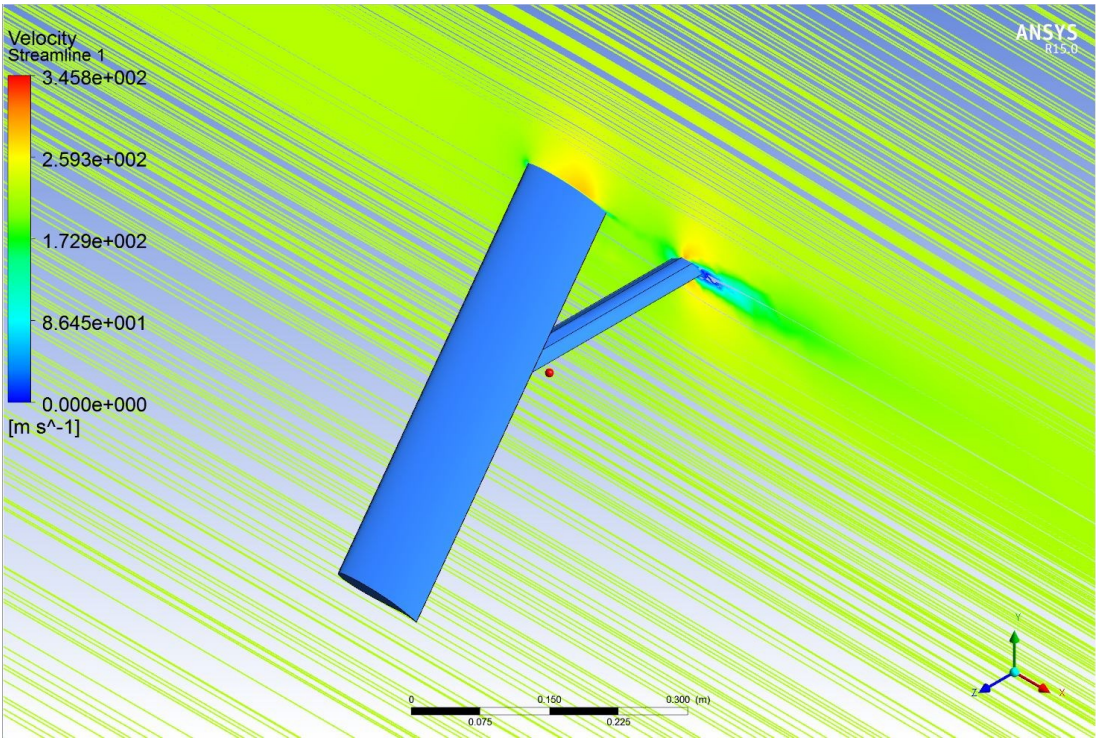


Figure 6.10. Symmetry surface path lines for the Design Point 1

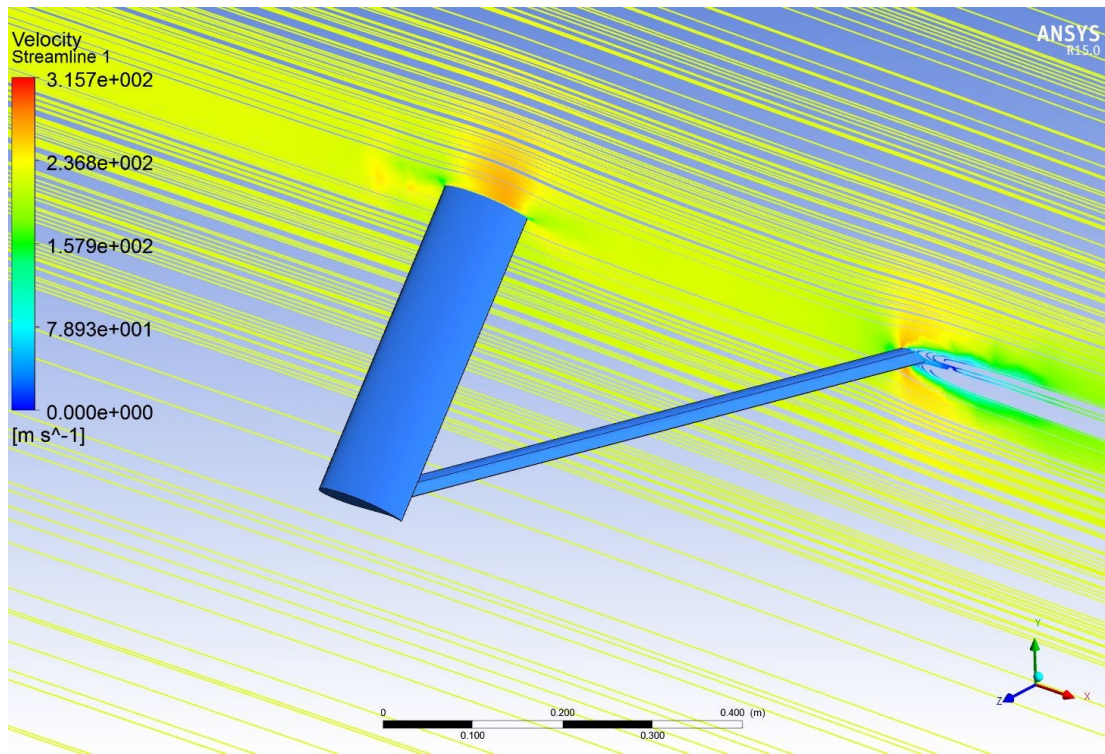


Figure 6.11. Symmetry surface path lines for the Design Point 2

6.4 Discussion and Conclusions

In this chapter, 3D aerodynamic analyses of the joined-wing configurations are conducted by using Fluent with implicit, upwind, second-order accurate, pressure based solver arrangement. The pressure contours and path line plots of the design points show close agreement with the similar transonic airfoil validation study presented in [44]. Furthermore, the velocity residuals have gone below 10^{-7} , therefore it can also be said that the convergence criteria satisfied.

CHAPTER 7

AERO-STRUCTURAL ANALYSES OF THE JOINED-WING CONFIGURATIONS

7.1 Introduction

This chapter presents the structural analyses of the joined-wing configurations under aerodynamic loads. In the previous chapter, aerodynamic analyses of the joined-wing configurations are performed. In this part of the study, the converged aerodynamic pressure distribution is mapped to the structural mesh of the joined-wing. Then static structural analyses of the joined-wing configurations are carried out. Maximum tip deflection, maximum equivalent stress and weight of the joined-wing configurations are calculated as outputs and stored for further optimization process.

7.2 Finite Element Analyses of the Joined-Wing Configurations under Aerodynamic Loads

The half symmetric parametric 3-D CAD models of the joined-wing configurations which are created in ANSYS® Design Modeler [41], are transformed to a commercial FEA software, ANSYS Mechanical [26], for the structural analyses. In ANSYS® Mechanical, finite element models (FEM) of the joined-wing configurations are constructed. Material properties of the wings (AL6061 T6) are inserted from material library of ANSYS. A twenty node hexagonal (Solid 186) and a ten node tetrahedron (Solid 187) higher order 3-D solid elements are used for structural meshing. Mesh convergence (the convergence process continues until the difference between the two consecutive results is less than 5%) is checked for equivalent stress and displacement values of the sample joined-wing configurations. Furthermore, the recommended element quality value of the 68 % is satisfied for each joined-wing configuration [26]. Structural meshes for the Design Point 1 and Design Point 2 can be seen in Figure 7.1

and 7.2, respectively. The FE models of the joined-wing configurations contain approximately 18000 element and 80000 nodes.

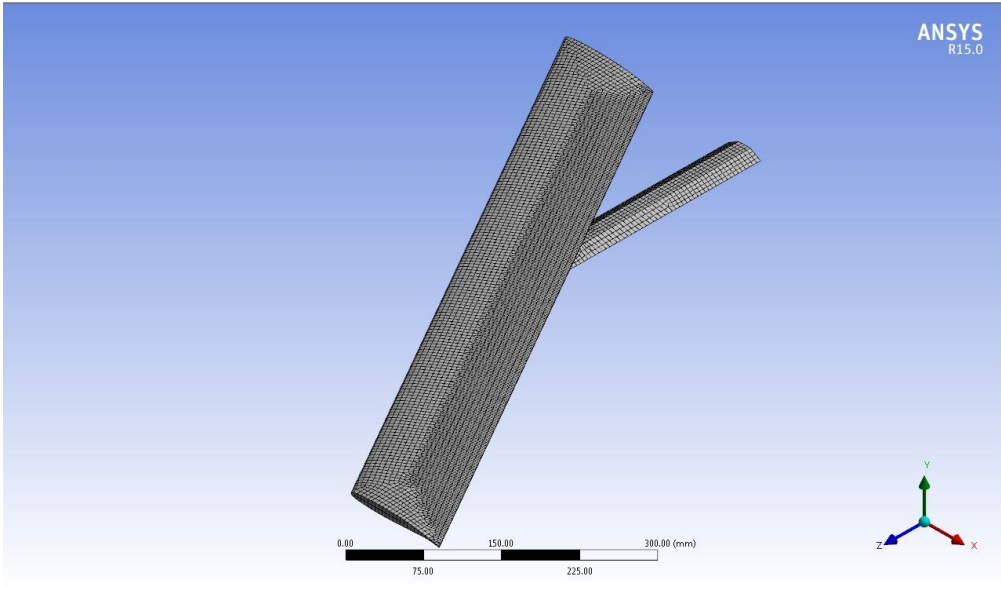


Figure 7.1. Structural mesh of the Design Point 1

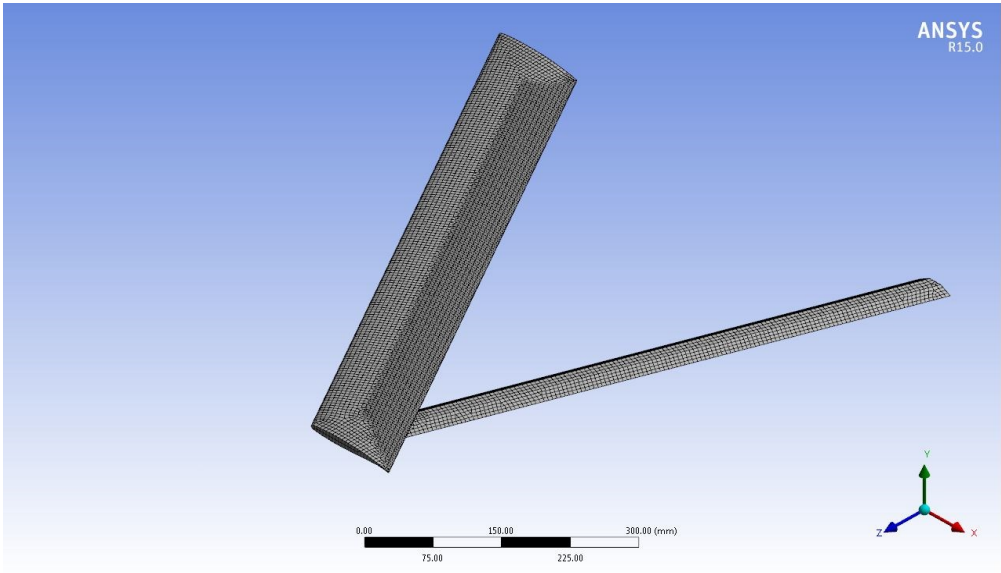


Figure 7.2. Structural mesh of the Design Point 2

The static structural analyses are performed under aerodynamic loads which are calculated in the previous chapter. The transferred static pressure distributions for the Design Point 1 and Design Point 2 are shown in Figures 7.3 and 7.4, respectively. These figures show that the transferred static pressure plots are consistent with the static pressure contour plots which are created in the previous chapter.

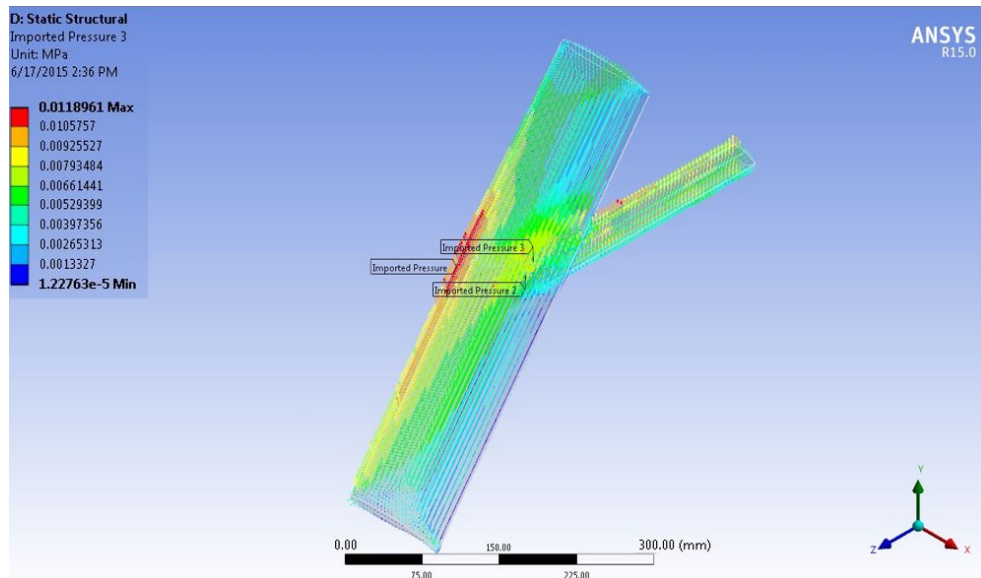


Figure 7.3. The transferred static pressure distribution in ANSYS® Mechanical for the Design Point 1

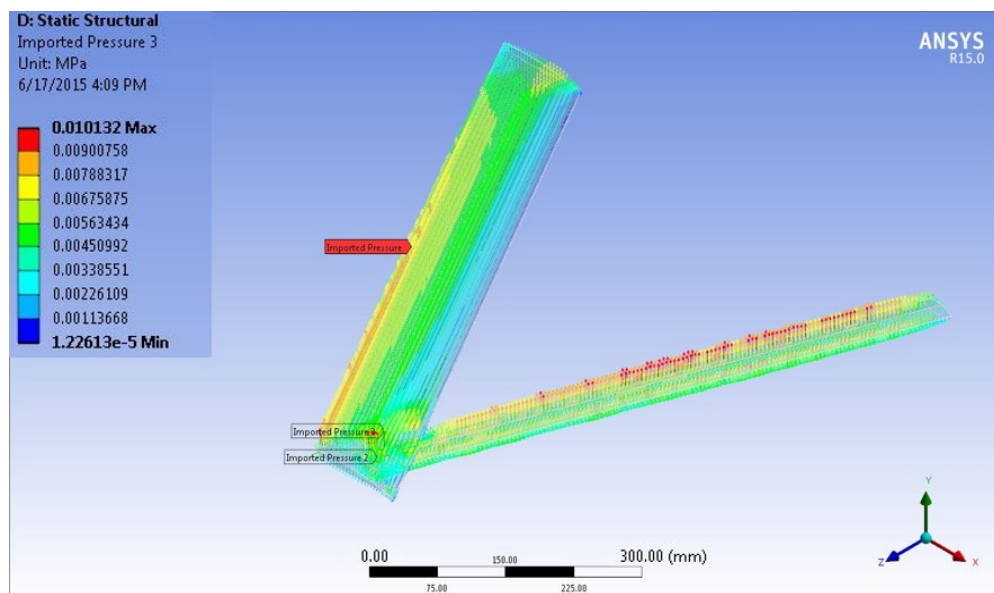


Figure 7.4. The transferred static pressure distribution in ANSYS® Mechanical for Design Point 2

After boundary conditions at the wing root and the joints are defined as rigid, the static structural analyses of joined-wings are performed. The displacement results of the Design Point 1 and Design Point 2 are given in Figures 7.5 and 7.6, respectively. The displacements shown in below figures are exaggerated to be able to see the results properly.

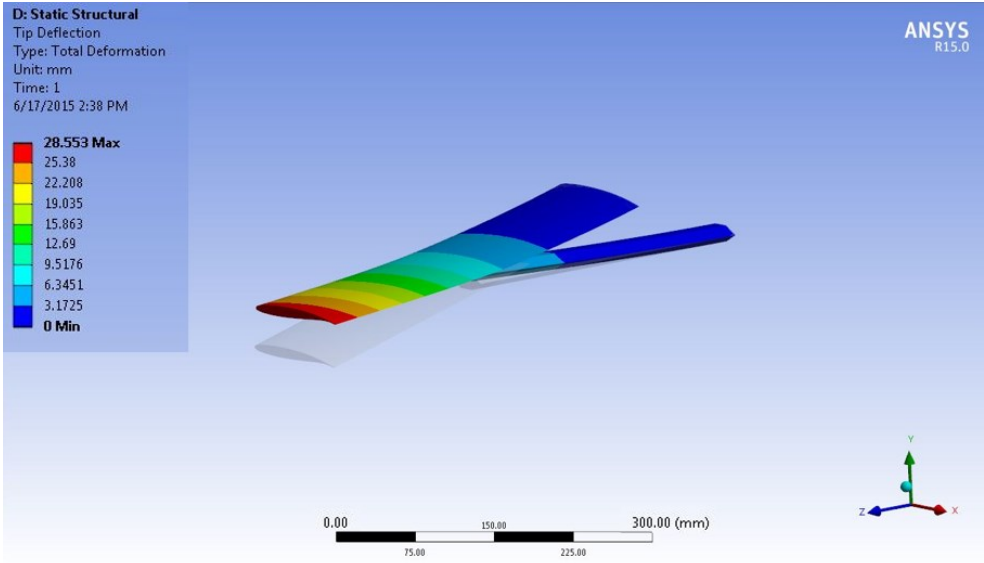


Figure 7.5. Displacement of the Design Point 1 [mm]

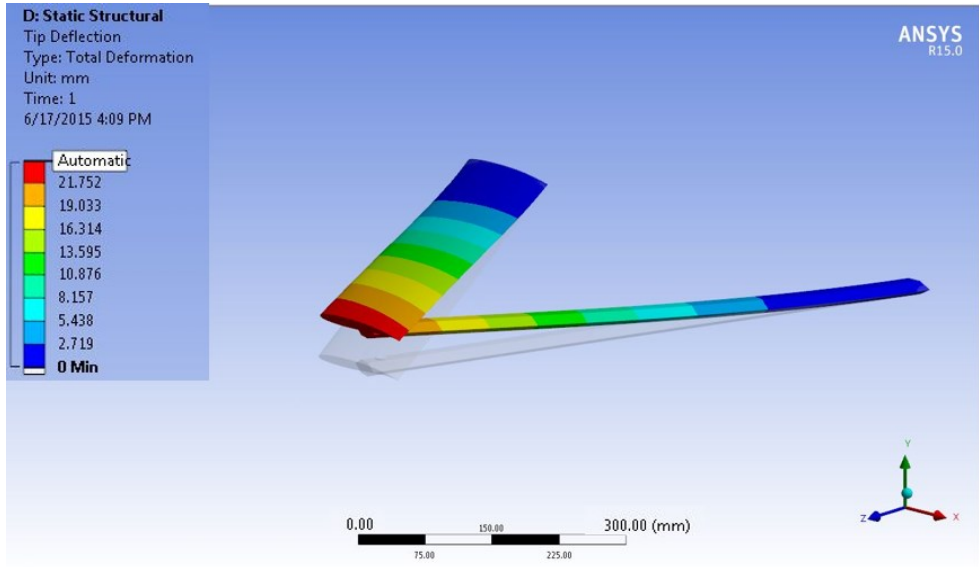


Figure 7.6. Displacement of the Design Point 2 [mm]

In the visualization of the stress values, sometimes discontinuous or abrupt changes in the stress pattern across the elements in the critical areas (such as connection, boundary condition areas, holes and etc.) may be observed. These changes may also provide incorrect assessment of the analysis results. Usually, these can be solved by local mesh refinement, however it requires lots of computational power. In this study, design of the wing root mount is not the primary focus, therefore in order to eliminate the misinterpreted results which are coming from local stresses in the vicinity of the joined-wing roots, divergent stress values are ignored by reading stress values from a plane parallel to the symmetry plane. The distance between the plane of the section of interest and the symmetry plane is taken as 5mm. The equivalent Von-Mises stress distributions caused by the aerodynamic loads for the design points are illustrated in the Figures 7.7, 7.8, 7.9 and 7.10.

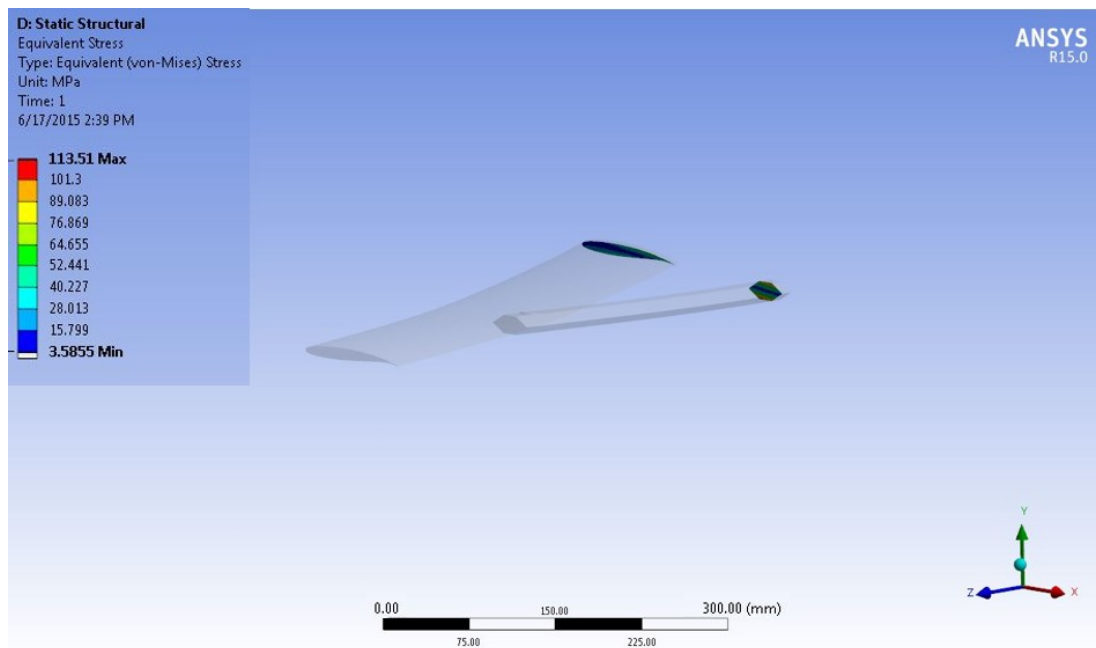


Figure 7.7. Equivalent stress distribution of the Design Point 1 [Pa]

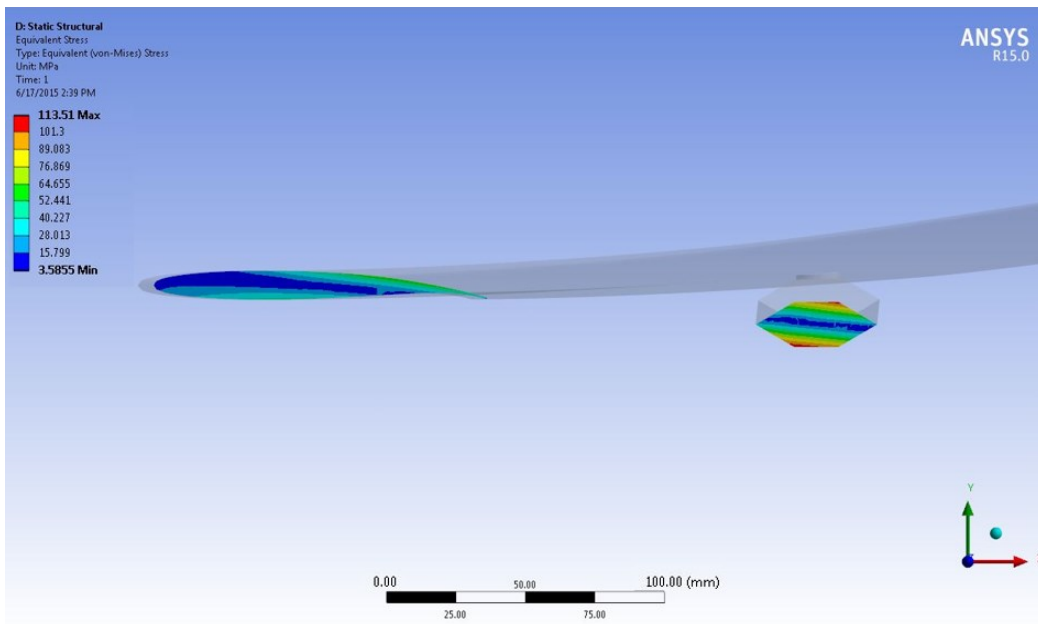


Figure 7.8. Zoomed view of the equivalent stress distribution of the Design Point 1 on the defined plane [Pa]

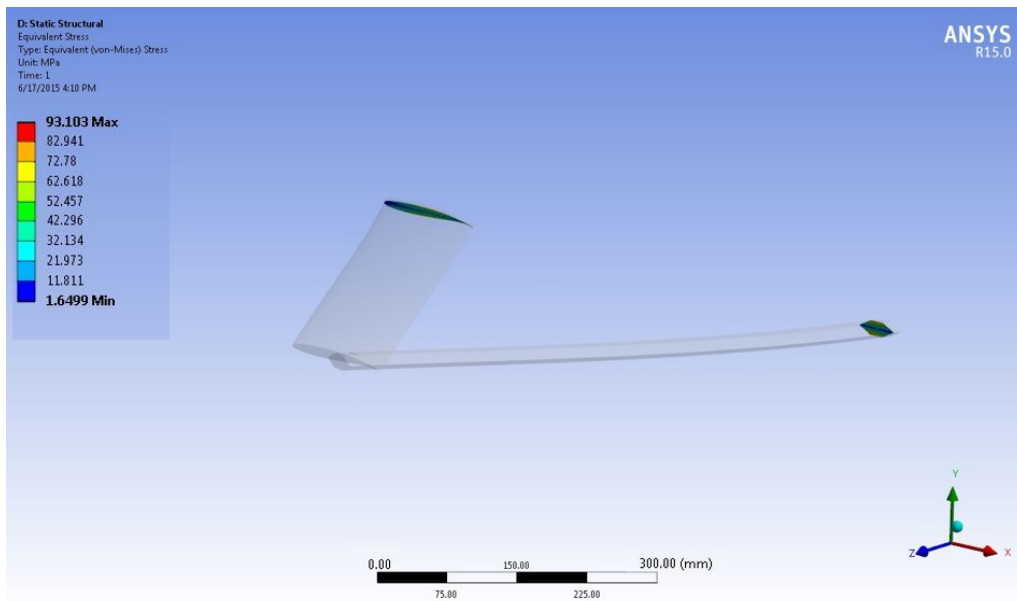


Figure 7.9. Equivalent stress distribution of the Design Point 2 [Pa]

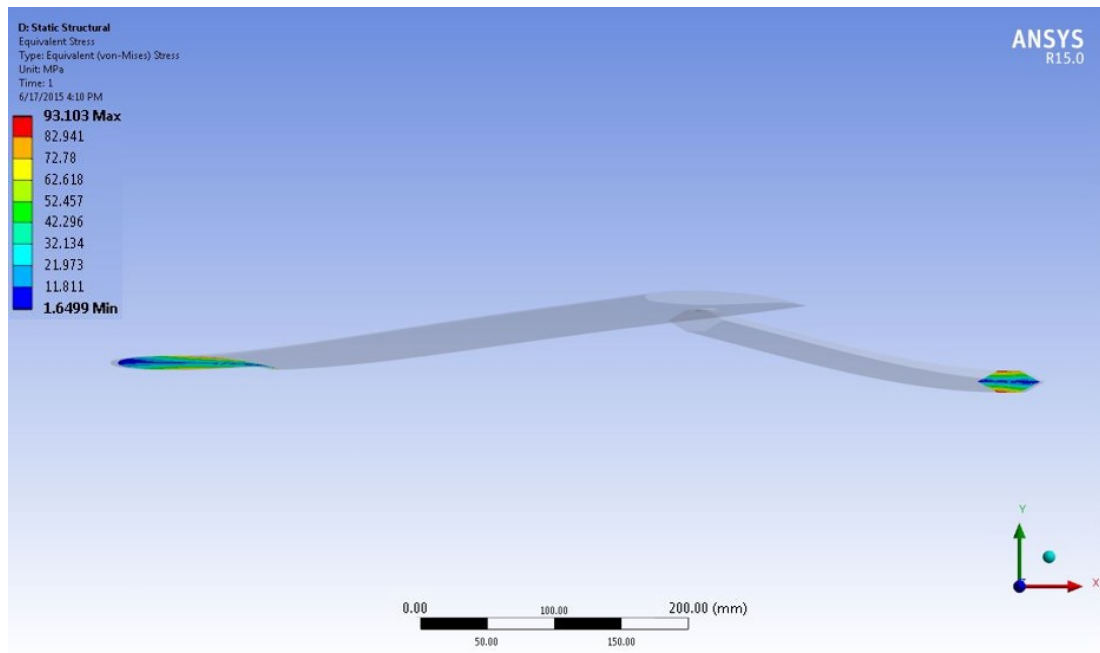


Figure 7.10. Zoomed view of the equivalent stress distribution of the Design Point 2 on the defined plane [Pa]

7.3 Discussion and Conclusions

In this chapter, the steps followed in the aero-structural analyses of joined-wing configurations are presented. The displacements and equivalent stress results of the joined-wing configurations under aerodynamic load are also visualized. The output of the aero-structural analyses such as maximum tip deflection, maximum equivalent stress and weight of the joined-wing configurations are stored for further optimization process. If the transferred static pressure graphs are compared with the static pressure contours plotted in the previous chapter, it can be seen visually that both graphs are in good agreement. The results of the static structural analysis for Design Point 1 and 2 indicate that lower joint location and aft wing sweep angle values result in higher equivalent stress and tip deflection at same flight condition, i.e. 0.75 Mach, 0 degree angle of attack.

CHAPTER 8

MULTIDISCIPLINARY DESIGN OPTIMIZATION OF THE JOINED-WING CONFIGURATIONS

8.1 Introduction

In this chapter, meta-model based multidisciplinary design optimization of the joined-wing configurations are carried out via ANSYS® Design Exploration [45]. The MDO analyses scheme of the ANSYS® Design Exploration is given in Figure 8.1.

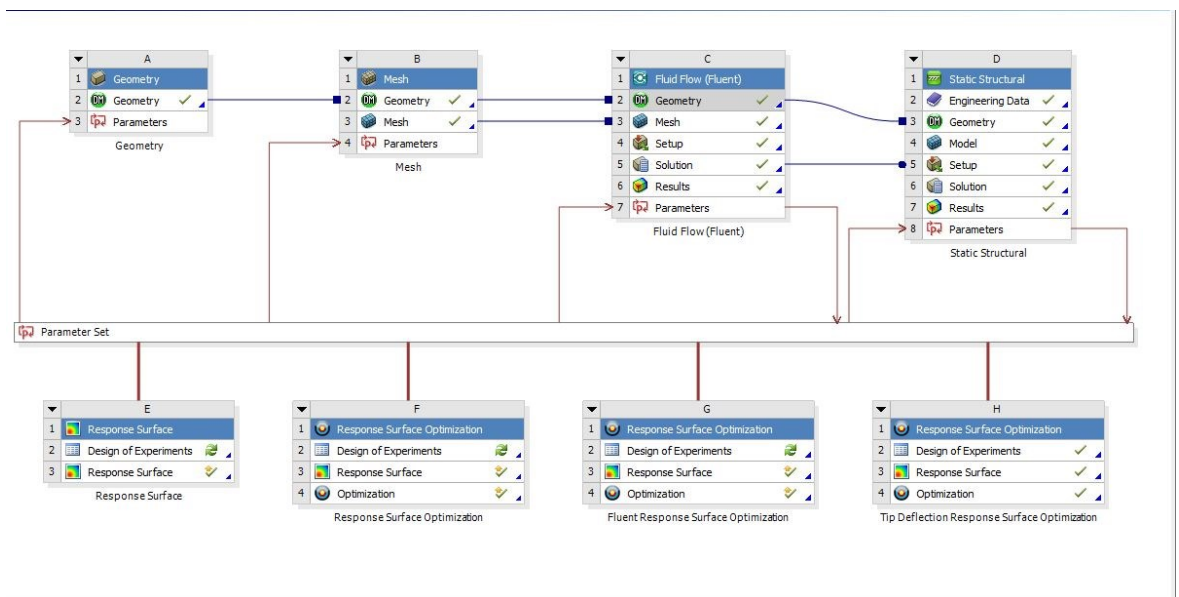


Figure 8.1. The framework of the ANSYS® Design Exploration

As it can be seen from the framework of ANSYS®, the process can be defined in the following order;

- A. Creation of the geometry
- B. Generation of aerodynamic mesh
- C. Aerodynamic analyses

D. Structural analyses

H. Optimization Process.

In the previous chapters, details of aerodynamic and structural analyses are explained. Here, multi-objective MDO analyses will be explained based on the following steps:

1. Formulation of optimization problem
2. Generation of design points (DOE)
3. Construction of response surfaces
4. Response surface optimization with multi-objective genetic algorithm.

The MDO of joined-wing configurations are performed mainly by the Response Surface Methodology (RSM). It can be defined as a collection of mathematical and statistical techniques for empirical model building and model exploitation. In other words, RSM tries to find a correlation between output parameter (i.e. response) and the input parameters. The response surface was developed in the early 1950's to model experimental responses [19] and then applied to the modelling of numerical experiments. Today, many engineering analysis applications require complex computer analyses or experiments. The steady improvement of computational capabilities has led to the consideration of phenomena of growing level of complexity. To deal with such a challenge, response surfaces are often used in place of the actual simulation models.

In addition to the MDO analyses, dynamic characteristics of joined-wing configurations are investigated as a separate study by changing two key parameters, namely; aft wing sweep angle and location of the joint. Meta-model based optimization study is conducted in order to determine how these parameters affect the vibration characteristics of the joined-wing configurations.

8.2 Optimization Problem Formulation

8.2.1 Design Variables and Operating Conditions

A guided gliding munition is generally subjected to various aerodynamic loading during its mission profile. In this study, two critical operating conditions, a 1 g cruise and a 2.5 g symmetric pull-up maneuver, are considered for MDOs of joined-wing configurations. These operating conditions are listed in Table 8.1.

Table 8.1. Operating conditions

Definition	Altitude (m)	Load Factor (g)
Cruise	10000	1.0
Maneuver	10000	2.5

In addition to the geometric design variables, munition's speed and angle of attack are also considered as continuous design variables. The input design variables and their ranges are summarized in Table 8.2. The simplified version of multidisciplinary optimization study considering constant 0.75 Mach cruise carried out at reference [46].

Table 8.2. Input design variables

Name	Lower Bound	Upper Bound
Joint Location (JL)	350 mm	750 mm
Aft Wing Sweep (AWS)	0°	30°
Angle of Attack (AOA)	-2°	10°
Mach Number	0.60	0.95

8.2.2 Objective Function

Objective function has a significant importance on the optimized structural design. In order to reflect the design intent for particular structure, the objective function must be carefully chosen [47]. The common multidisciplinary design objectives can be listed as: range, weight, displacements, stresses, vibrations and etc. Kenway and Martins [14] consider TOGW minimization and fuel-burn minimization as objective functions.. Kim et. al. [8] chose drag minimization, L/D maximization objectives for MDO of supersonic fighter wing.

In this study, objectives functions selected as below:

Gliding Range

If the platform is an airplane, it would be appropriate for range calculation to use the Breguet equation given as:

$$R = \frac{V}{C_t} \frac{C_L}{C_D} \ln \left(\frac{W_1}{W_2} \right) \quad (8.1)$$

where the R is the range, V is the flight speed, C_t is the trust-specific fuel consumption, and W_1 and W_2 are the initial and final cruise weights. However, since the dropped munition does not consume any fuel, its weight is constant. The guided munition can be assimilated as an airplane in which the engine is turned off, therefore its trust is zero. In such condition, to maintain airspeed, it is necessary to put the vehicle at such an attitude that the component of the gravity force in the direction of the velocity vector balances the drag [48]. Pictorial illustration of gliding airplane, gliding angle, range and altitude information is given at Figure 8.2. The flight path angle and glide range is given in Equation 8.2 and 8.3, respectively.

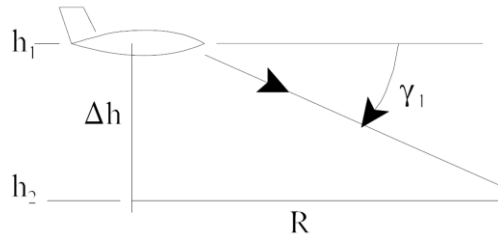


Figure 8.2. Gliding platform illustration

$$\tan \gamma_1 = \frac{h_1 - h_2}{R} = \frac{-\Delta h}{DR} \quad (8.2)$$

$$R = \frac{h_1 - h_2}{\tan \gamma_1} = \frac{L}{D} (h_1 - h_2) \quad (8.3)$$

where γ_1 is the flight path angle that the velocity makes with the horizontal. h_1 and h_2 are the initial and final altitudes, respectively. As can be seen Equation 8.3 the glide range is depends on L/D and Δh . It is clear that the maximum range occurs when glide angle is the flattest and that occurs at maximum L/D (or minimum drag).

Therefore in this research, to extent flight range at 1 g cruise and to improve maneuverability at the 2.5 g flight condition, lift constrained drag minimization should be performed.

Tip deflection of the joined-wing

Tip deflection of the joined-wing is directly related with the bending stiffness. Therefore, in order to make the designed joined-wing structurally stiffer and more stable, the joined-wing tip deflection has to be minimized.

Weight of the designed joined-wing,

To increase performance of the aircrafts, minimum weight aspect will always be one of the primary objectives of the structural designer. Since the front wing does not

changing, the only variance in the weight comes from the aft wings. The aft wings weight is depend on JL and ASA

Furthermore, the second and third objectives are also related with aeroelastic tailoring [49]. Aeroelastic tailoring is defined in [34] as; “... *Aeroelastic tailoring is the embodiment of directional stiffness into an aircraft structural design to control aeroelastic deformation, static or dynamic, in such a fashion as to affect the aerodynamic and structural performance of that aircraft in a beneficial way. ...*”

Effective determination of input design parameters by considering above design objectives also increases the effectiveness of aeroelastic tailoring.

During the multidisciplinary optimization process, the equivalent maximum stress (the reading location is explained in Chapter 7) is observed as a structural constraint to make sure the stress levels does not excess the elastic limits of the structure.

8.2.3 Standard Formulation

First, the optimizations independently performed for each design objectives. Then, multi criteria optimization is done. The three optimization problem can be written in its standard form as below:

1. The first design objective is maximizing the range by performing lift constrained drag minimization. D is a nonlinear function of the 4 input design parameters. In formal optimization terms for this case may be expressed as

$$\begin{array}{ll}
 \text{minimize} & D(\mathbf{x}) \\
 \text{with respect to} & \mathbf{x} \\
 \text{subject to} & L(\mathbf{x}) = \begin{cases} W, & \text{cruise operating condition} \\ 2.5 W, & \text{maneuver operating condition} \end{cases} \\
 & \sigma_{root} < \frac{\sigma_{yield}}{1.5} = 335 \text{ MPa}
 \end{array}$$

where \mathbf{x} denotes a vector of input design variables,

$$\mathbf{x} = [x_1, x_2, x_3, x_4]$$

σ_{root} is the maximum equivalent stress at the root section, σ_{yield} is the yield strength of the AL7075 T6. $L(x)$ is the lift, W is the weight of the munition. The 1.5 safety factor comes from the system requirements of the project.

- The second design objective is to minimize δ_{tip} , where δ_{tip} is a nonlinear function of the 4 input design parameters. In formal optimization terms for this case may be expressed as

$$\begin{aligned} &\text{minimize} && \delta_{tip}(\mathbf{x}) \\ &\text{with respect to} && \mathbf{x} \\ &\text{subject to} && L(\mathbf{x}) = \begin{cases} W, & \text{if cruise operating condition} \\ 2.5 W, & \text{if maneuver operating condition} \end{cases} \\ &&& \sigma_{root} < \frac{\sigma_{yield}}{1.5} = 335 \text{ MPa} \end{aligned}$$

- The third design objective is to minimize weight of the joined-wing. The weight is a linear function of the 2 geometric parameters. However, the Lift constraint is a nonlinear function of 4 input design parameters.

$$\begin{aligned} &\text{minimize} && W_{joined-wing}(\mathbf{x}) \\ &\text{with respect to} && \mathbf{x} \\ &\text{subject to} && L(\mathbf{x}) = \begin{cases} W, & \text{if cruise operating condition} \\ 2.5 W, & \text{if maneuver operating condition} \end{cases} \\ &&& \sigma_{root} < \frac{\sigma_{yield}}{1.5} = 335 \text{ MPa} \end{aligned}$$

As a separate optimization study from the multidisciplinary design optimization, dynamic characteristic of the joined-wing configurations are investigated by response surfaces. Input variables are, as before, two key geometric parameters, namely; aft wing sweep angle and location of the joint. In this optimization study, response surfaces are created in order to observe how the geometric parameters affect the vibration characteristics of the joined-wing configurations and design objective is

defined as shifting the fundamental natural frequency of the joined-wing configurations to a higher one.

8.3 Design of Experiments

Design of experiments (DOE) can be defined as a scientific way to locate the sample design points in the space design. The common characteristics of the DOE methods is to pinpoint these sampling points such that the relation between random input variables and the output variables is explored in most efficient way.

DOE starts with determining the objectives of the experiment and choosing the factors to be explored. The selection of the types of the design depends on the objectives of the experiment and the number of factors to be explored. The three main objectives of the experimental design can be listed as follows: Comparative, Screening and Response Surface. Comparative objective is used to spot one important factor and its influence on varying response excluding other parameters. Screening objective is used to reduce the number of factors by eliminating the ones that have minimal influence on the output. Response Surface Objective is mainly used to optimize the response and make the process more robust [50]. In this study, since the number of design variables is four and optimization study is aimed for the afore-mentioned objectives, the response surface methodology is preferred. A guideline for design selection is given in Table 8.3.

Table 8.3. Guideline for design selection [50]

Number of Factors	Comparative Objective	Screening Objective	Response Surface Objective
1	1-Factor Completely Randomized Design	–	–
2 to 4	Randomized Block Design	Full or Fractional Factorial	Central Composite or Box-Behnken
5 or more	Randomized Block Design	Fractional Factorial or Plackett-Burman	Screen First to Reduce Number of Factors

Although, there are huge number of DOE methods available in the literature, the most feasible ones for fitting the approximating models of second order response surface are listed in ANSYS DX [45] as follows:

1. Central Composite Design (CCD)
2. Box-Behnken Design (BBD)
3. Latin Hypercube Sampling Design (LHS)
4. Optimal Space-filling Design (OSF)
5. Sparse Grid Initialization

Brief summaries of design of experiments are given below.

8.3.1 Design of Experiment Types

Face Centered Central Composite Design (FCCCD)

Face centered central composite design generates a design space composed of one center point, eight corners of the cube, four center of faces of the cube in 3-D. FCCCD selections for three design variables can be seen in Figure 8.3. The FCCCD produce $(1+2N+2^N)$ points, where N is the number of design variables. It is recommended to use of moderate number of factors (less than 5) to have maximum efficiency [45].

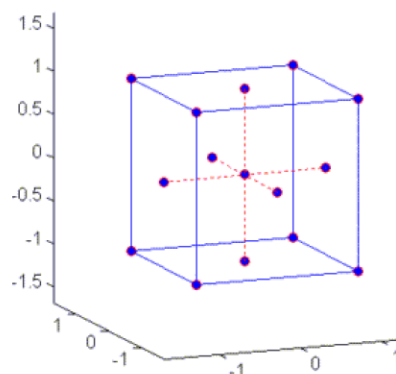


Figure 8.3. Face centered central composite designs (FCCCD) of three factors [45]

Box-Behnken Design (BBD)

The Box-Behnken design creates a design space composed of one or more center point, twelve midpoints of edges of the cube in 3-D. Figure 8.4 illustrates a Box-Behnken design for three factors.

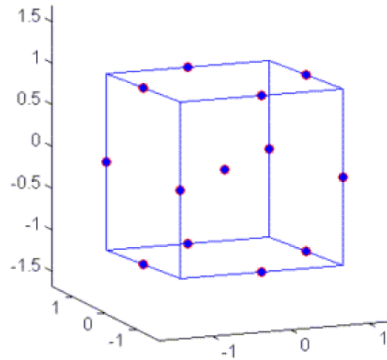


Figure 8.4. Box-Behnken designs (BBD) of three factors [45]

Latin Hypercube Sampling Design (LHS)

An LHS design is an advanced form of the Monte Carlo sampling method. In an LHS design, points are generated randomly in the design space, but there is only one sample in each row and each column of the design space. Figure 8.5 illustrates a LHS designs for two factors.

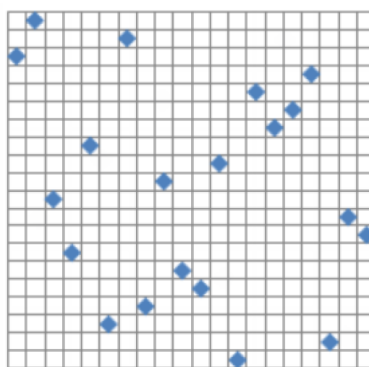


Figure 8.5. LHS designs for two factors [45]

Optimum Space Filling Design (OSF)

Optimum space filling algorithm creates design points such that the distance between any two points are maximized and they are equally distributed throughout the design space. The purpose of OSF is to gain insight into design with the fewest number of points. Figure 8.6 illustrates a OSF designs for two factors.

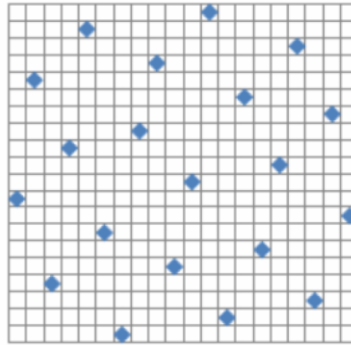


Figure 8.6. Optimum space filling designs for two factors [45]

Sparse Grid

The Sparse Grid meta-modeling is required to run a hierarchical Sparse Grid interpolation algorithm. It is an adaptive meta-model driven by observing requested accuracy. One advantages of the Sparse grid is that it refines only the necessary directions, therefore fewer points are enough to get the same quality response surfaces.

8.4 Response Surface (RS) Methodology

The aim of response surface methodology (RSM) is perform a series of experiments, based on numerical analyses or physical experiments, for a prescribed set of design points, and to construct global approximation of the measured quantity over the design space. The RS expresses the objective and constraint by simple functions using regression techniques. In this thesis the focused on following meta-modelling types [45]:

1. Standard response surface - Full 2nd order polynomials
2. Kriging
3. Non- Parametric Regression

4. Neural Network
5. Sparse Grid

8.4.1 Response Surface Types

Brief summaries of ANSYS® Design Exploration meta-modelling types are given below:

Standard response surface - Full 2nd order polynomials

The standard response surface method was introduced by G. E. P. Box and K. B. Wilson in 1951 [19]. In this method, second-degree polynomial is used to perform in order to determine the relationship between input parameters and output parameters based on the sample points determined by DOE.

Kriging

Kriging is a method of interpolation that provides an improved response quality and fits higher order variations of the output parameter. It provides better results than the Standard Response surface when the variations of the output parameters is stronger and non-linear. Automatic refinement option is provided for Kriging meta-model in ANSYS® Design Exploration. In fact, the effectiveness of the Kriging algorithm come from the ability of its internal error estimator to improve response surface quality by generating refinement points and adding them to the areas of the response surface most in need of improvement. In each iteration of refinement, Kriging model is reconstructed and the predicted relative error [51] is calculated. In this study for Kriging meta-modelling, the refinement procedure is continued until the error becomes less than 5%.

Non- Parametric Regression

Non-parametric regression meta-modelling used to predict high nonlinear behavior of the output parameters with respect to the inputs. Unlike the parametric approach where the response function is described by a finite set of parameters, nonparametric modelling provides flexibility in regression analysis. It is usually slow to compute

when compared to other mentioned response surfaces and recommended to use when the results are noisy.

Neural Network (NN)

The neural network method is inspired by the nature of human brain. The main element of NN is a neuron whose shape and size can change according to its function. A neural network contains the input layer neurons, hidden layer neurons, and an output layer. A simple presentation of ANN is shown in Figure x. Combination of neurons with different weighted interconnections constructs the neural networks.

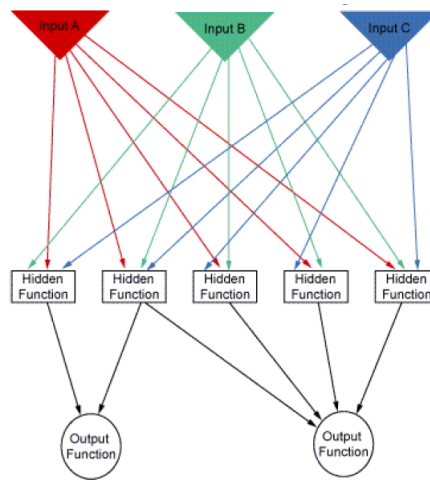


Figure 8.7. NN architecture [45]

Sparse Grid

Sparse Grid refines itself automatically. A dimension-adaptive algorithm provides it to determine which dimensions are most important to the objectives functions, thus reducing computational effort.

8.5 Accuracy Assessments of Response Surfaces

Although RS is an effective optimization tool, its accuracy of RS model is often affected by many factors such as the use of limited number of data points for model generation or poorly chosen design points. This part specifically focused on the accuracy of the RS meta-models and possible way of improving it by using feasible treatments.

The goodness of fit of the RS is assessed by seven error measures in ANSYS® Design Explorer [45] as Coefficient of Determination (R^2), Adjusted Coefficient of Determination (Adjusted R^2), Maximum Relative Residual, Root Mean Square (RMS) Error, Relative Root Mean Square Error, Relative Maximum Absolute Error, and Relative Average Absolute Error [45]. For R^2 and Adjusted R^2 the value of 1 and the remaining error measures, the value of 0% indicates the best quality of the response surface. These error criteria are briefly summarized below.

Coefficient of Determination (R^2):

The response surface regression equation explains the percent of the deviation of the output parameter. The ratio of the explained deviation to the total deviation is called as the Coefficient of Determination. The best value is 1.

The points used to create the response surface are likely to contain variation for each output parameter (unless all the output values are the same, which will result in a flat response surface). This variation is illustrated by the response surface that is generated. If the response surface were to pass directly through each point (which is the case for the Kriging meta-model), the coefficient of determination would be 1, meaning that all variation is explained.

Mathematically represented as:

$$R^2 = 1 - \frac{\sum_{i=1}^N (y_i - \hat{y}_i)^2}{\sum_{i=1}^N (y_i - \bar{y})^2} \quad (8.11)$$

Where;

y_i = value of the output parameter at the i-th sampling point

\hat{y}_i = value of the regression model at the i-th sampling point

\bar{y} = the arithmetic mean of the values y_i

σ_y = the standard deviation of the values y_i

Adjusted Coefficient of Determination (Adjusted R^2):

Despite of the R^2 , the Adjusted R^2 take sample size in consideration. Again the best value is 1. This is generally more valuable when the number of samples is less than 30. Furthermore, it is only meaningful for standard responses. Mathematical representation is given in equation 8.12:

$$adjusted\ R^2 = 1 - \frac{N-1}{N-P-1} \frac{\sum_{i=1}^N (y_i - \hat{y}_i)^2}{\sum_{i=1}^N (y_i - \bar{y})^2} \quad (8.12)$$

Maximum Relative Residual:

The maximum distance out of all of the points from the calculated response surface to the points generated from the regression model. The best value is 0%; in general, the closer the value is to 0%, the better quality of the response surface. Mathematical representation is given in equation 8.13:

$$Max.\ Relative\ Residual = \max_{i=1:N} \left(Abs \left(\frac{y_i - \hat{y}_i}{\bar{y}} \right) \right) \quad (8.13)$$

Root Mean Square (RMS) Error:

This is the square root of the arithmetic mean of the squares of the residuals at the DOE points for meta-model methods. Mathematical representation of RMS error is given in equation 8.14.:

$$RMS\ error = \sqrt{\frac{1}{N} \sum_{i=1}^N (y_i - \hat{y}_i)^2} \quad (8.14)$$

Relative Root Mean Square (RMS) Error:

This is the square root of the arithmetic mean of the squares of the residuals scaled by the actual output values. Mathematical representation of RMS error is given in equation 8.15:

$$Relative\ RMS\ error = \sqrt{\frac{1}{N} \sum_{i=1}^N \left(\frac{y_i - \hat{y}_i}{y_i} \right)^2} \quad (8.15)$$

Relative Maximum Absolute Error:

This is the absolute maximum residual value relative to the standard deviation of the actual output data, modified by the number of samples. The best value is 0%; in general, the closer the value is to 0%, the better quality of the response surface.

$$Rel.\ Max.\ Abs.\ Error = \frac{1}{\sigma_y N} \max_{i=1:N} (Abs(y_i - \hat{y}_i)) \quad (8.16)$$

Relative Average Absolute Error

This is the average of the residuals relative to the standard deviation of the actual outputs. This is useful when the number of samples is low (<30). The best value is 0%; in general, the closer the value is to 0%, the better quality of the response surface.

$$Rel.\ Ave.\ Abs.\ Error = \frac{1}{\sigma_y N} \max_{i=1:N} (Abs(y_i - \hat{y}_i)) \quad (8.17)$$

8.5.1 Comparisons of Different DOE Types

A comparative study is performed to understand the effects of the selection of different DOE types on the accuracy of RS models. To investigate the issue, for each DOE types which are available in ANSYS® Design Explorer, sampling design points are generated and analyzed. The generated design points of FCCCD, BBD, OSF, LHS DOE types are given in Appendix B. In order to get an insight about how the DOE types affect the RS accuracy, standard second order polynomial RS are fitted into each data created by different DOE types without refinement. Table 8.4 presents evaluations of accuracies of the total lift RS according to different DOE types.

Table 8.4. Accuracy of response surfaces based on DOE types

	FCCCD	BBD	LHS	OSF
Coefficient of Determination (Best Value = 1)	0.9980	0.9953	0.9719	0.9858
Adjusted Coeff of Determination (Best Value = 1)	0.9975	0.9941	0.9663	0.9829
Maximum Relative Residual (Best Value = 0%)	12.7954	10.8619	12.2209	8.1514
Root Mean Square Error (Best Value = 0)	20.6274	23.1059	44.1634	30.6450
Relative Root Mean Square Error (Best Value = 0%)	4.9405	4.1907	5.7220	4.2975
Relative Maximum Absolute Error (Best Value = 0%)	11.3205	14.8454	45.6002	24.5685
Relative Average Absolute Error (Best Value = 0%)	3.5079	5.1811	12.7931	9.8579

8.5.2 Comparisons of Different RS Methods

In this section, different response surface models which are exist in ANSYS® Design Explorer used to approximate responses. In order to compare their accuracies, FCCCD selected as a base design and response surfaces models including standard response surfaces, neural network, kriging, non-parametric regression are constructed on that DOE. To assess accuracies of the RS models, detailed goodness of fit charts are created and given in Appendix C. Their comparison according to lift approximations are given at Table 8.5. This measurement values are evaluated from verification points which are given in Appendix B. The table shows that standard RS provides slightly better approximations. However, the error measurement values are not acceptable. Therefore, optimization study is further investigated by performing by applying kriging algorithm due to its auto-refinement option and relatively high accuracy.

Table 8.5. Accuracy of response surfaces created by different RS modelling types

	Standard RS	Neural Network	Non-Parametric Reg.	Kriging
Maximum Relative Residual (Best Value = 0%)	9.8668	162.5984	18.3940	18.0648
Root Mean Square Error (Best Value = 0)	37.5901	258.3021	53.5712	41.4455
Relative Root Mean Square Error (Best Value = 0%)	4.8482	58.5672	7.6802	5.5180
Relative Maximum Absolute Error (Best Value = 0%)	25.1814	138.8897	33.3687	34.4551
Relative Average Absolute Error (Best Value = 0%)	5.5576	38.2577	8.2146	5.6402

To investigate effects of selected DOE types with refinement, FCCCD, BBD, LHS and OSF DOE data are used again. RS models are created by applying Kriging algorithms with auto-refinement option. In the auto-refinement procedure, predicted related error [45] is considered as a convergence criterion and set as 5%. The refinement points for each case are given in Appendix D. The accuracies are assessed through 20 verification points given in Appendix B. Table 8.6 displays accuracy comparisons of each case for total lift response. In Table 8.6 in addition to kriging, error measurements of the total lift RS which is created by Sparse Grid algorithm is included. The results points out that OSF designs provides same order of error with less number of design points, therefore it can be said that it works with kriging more efficient compared to other DOE types.

Table 8.6. Accuracy of response surfaces created by different RS modelling types

DOE Type	FCCCD	BBD	LHS	OSF	Sparse Grid
Number of refinement points	56	59	49	28	109
Total number of design points	81	84	74	53	118
Maximum Relative Residual (Best Value = 0%)	4.8138	7.4312	7.3244	7.1013	6.6765
Root Mean Square Error (Best Value = 0)	13.4530	17.3818	25.1531	23.5924	19.3037
Relative Root Mean Square Error (Best Value = 0%)	2.2093	2.8439	3.5448	3.4523	2.6287
Relative Maximum Absolute Error (Best Value = 0%)	9.6000	12.9537	22.2885	14.5820	14.4136
Relative Average Absolute Error (Best Value = 0%)	2.6153	3.4945	4.8172	4.7151	3.2985

As a final comparison study, again FCCCD data as selected as base design data. The refinement points calculated in kriging auto-refinement procedure inserted on this data and RS models are constructed again by applying standard RS, Neural Network, Non-parametric regression, kriging. Table 8.7 displays accuracies of RS constructed on refined FCCCD data. With refined DOE, kriging shined out of others while all RS meta-modelling types are using the same data. Therefore, the optimization study is conducted using OSF DOE and kriging algorithm.

Table 8.7. Accuracy of response surfaces created by different RS modelling types

Response Surface Modelling Type	Standard RS	Neural Network	Non-Parametric Reg.	Kriging
Maximum Relative Residual (Best Value = 0%)	15.3251	9.8868	9.0757	4.8138
Root Mean Square Error (Best Value = 0)	32.3464	24.3909	42.5015	13.4530
Relative Root Mean Square Error (Best Value = 0%)	7.5890	4.3145	4.8363	2.2093
Relative Maximum Absolute Error (Best Value = 0%)	16.7594	14.8135	32.3210	9.6000
Relative Average Absolute Error (Best Value = 0%)	7.0533	5.0062	6.6640	2.6153

The refinement procedure and following optimization process is summarised and illustrated in Figure 8.8.

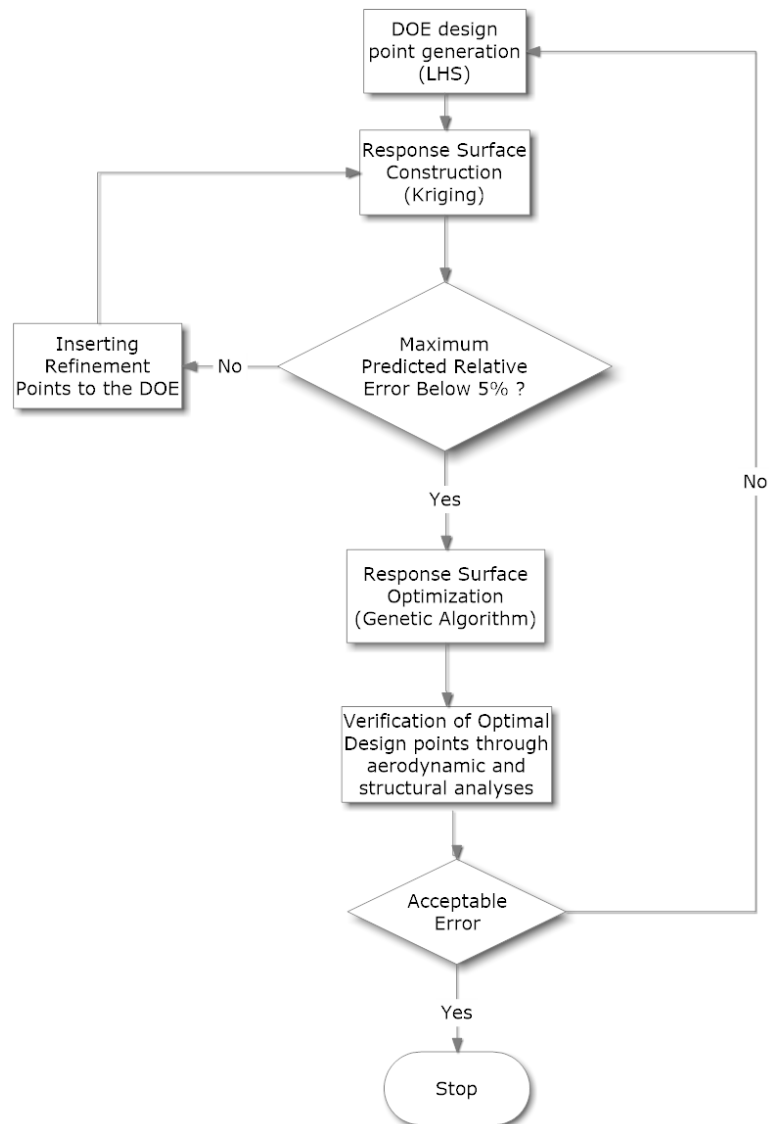


Figure 8.8. Summary of response surface optimization process

8.6 Response Surface Results

In this section, the created response surfaces are explained and evaluated below:

Response surfaces for Total Lift (L)

Total lift responses (in N) based on Kriging metamodel are shown in Figure 8.9, 8.10 and 8.11. The results are presented in three different graphs as functions of “joint location”, “aft wing sweep angle”, “Mach number and AOA”. Figure 8.10 and 8.11 show that the total lift peaks up when the joint location is below 400 mm but then it falls when the joint location increases from 400 mm to 600mm. Meanwhile, the aft wing sweep angle has a considerable influence on total lift response. As shown in Figure 8.10, the response surface results indicate that a higher aft wing sweep angles produce lower total lift responses. The reason for this is that since the aft wing cross section has a hexagonal shape instead of producing lift, it influences the total lift in an adverse manner. Figure 8.11 shows that Mach number and AOA have a stronger influence on the total lift responses than that of the joint location and aft wing sweep angle. Additionally, higher Mach number and AOA produce higher total lift values.

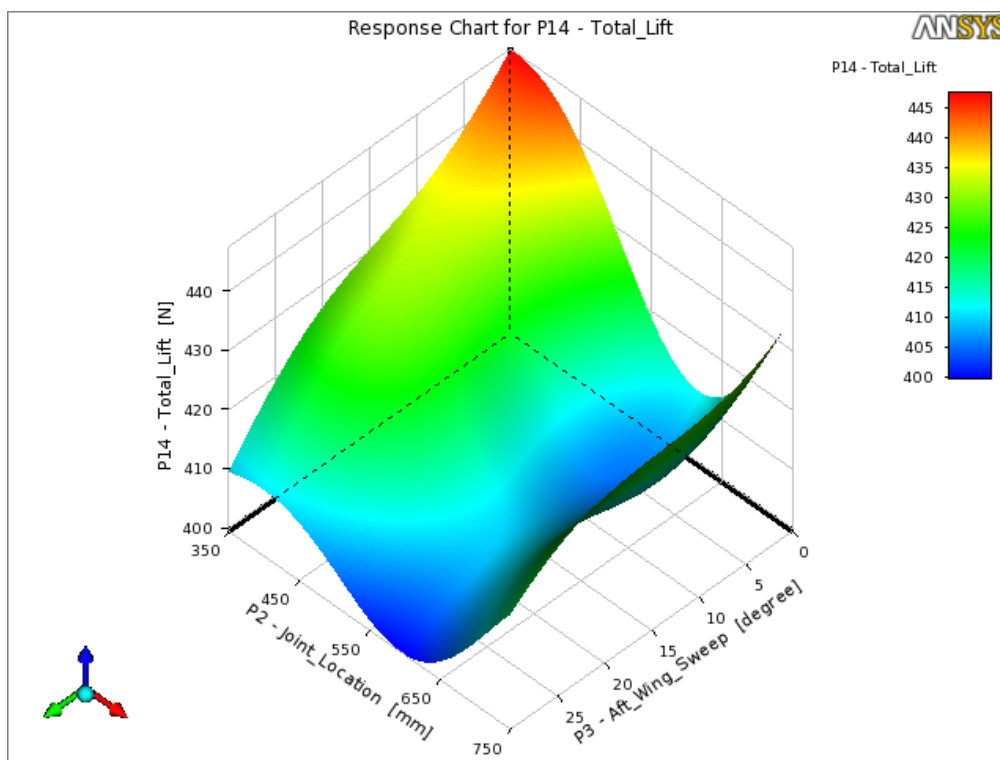


Figure 8.9. Total lift [N] response as a function of joint location and aft wing sweep angle (AOA: 0°, Mach: 0.7)

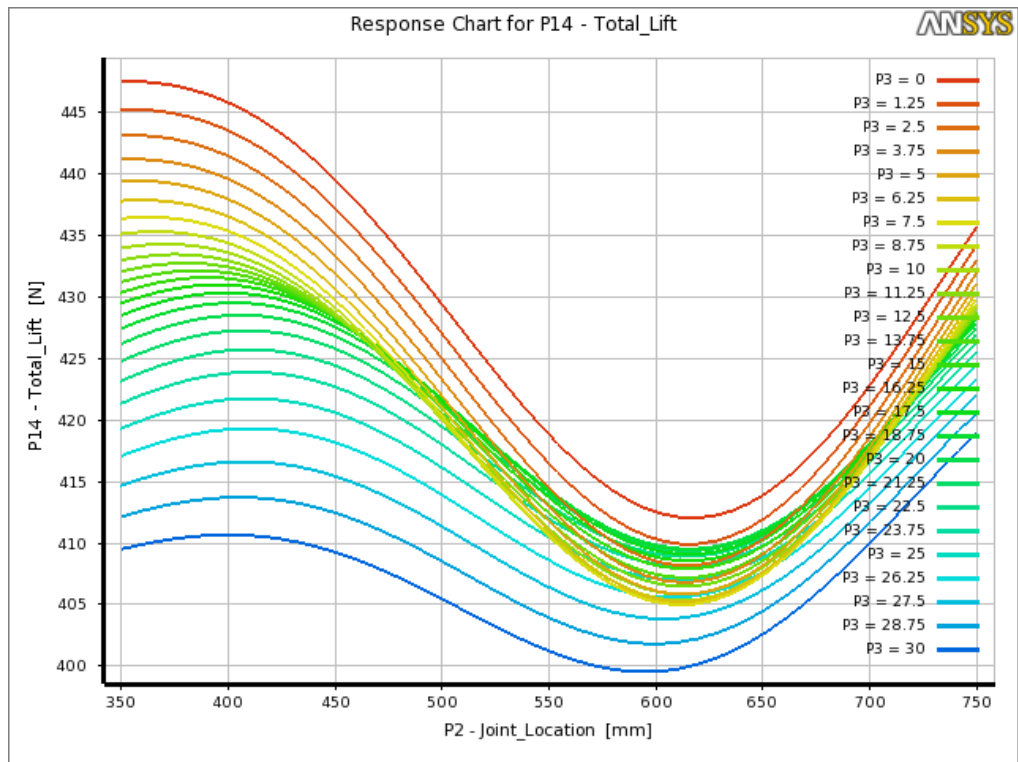


Figure 8.10. 2D slice response chart for total lift [N] as a function of joint location and aft wing sweep angle (AOA: 0°, Mach: 0.7)

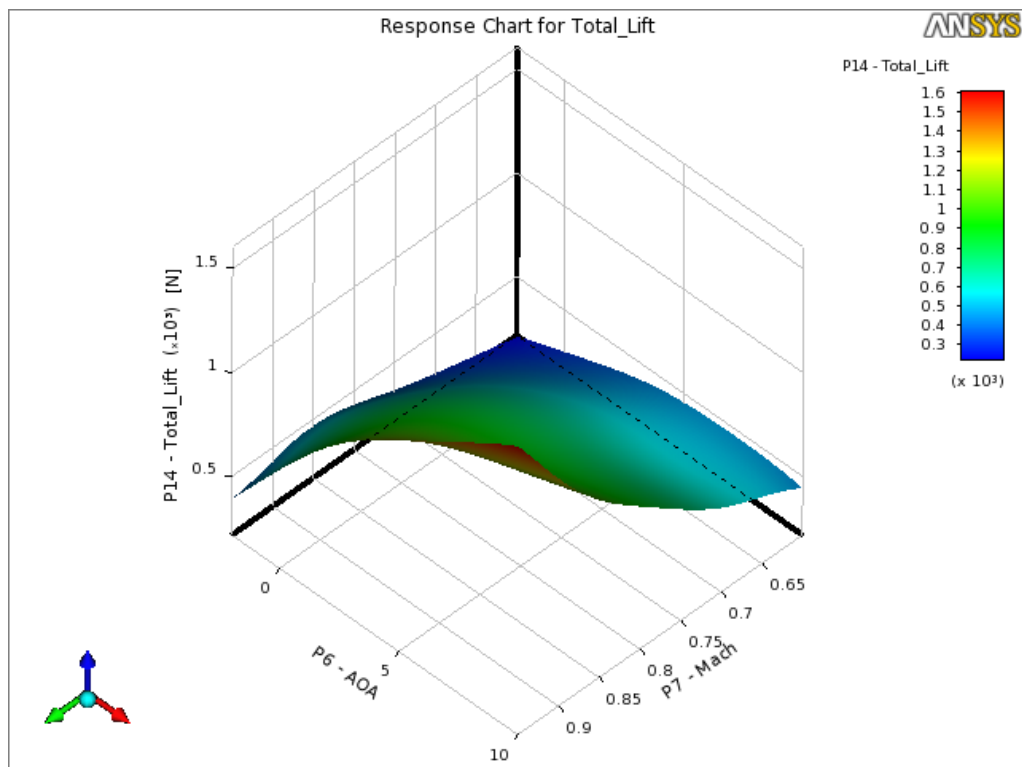


Figure 8.11. Total lift [N] response as a function of Mach number and AOA (joint location: 350 mm, aft wing sweep angle: 0°)

Response surfaces for Total Drag (D)

As it can be seen from the Figures 8.12 and 8.13 that the higher joint location results in bigger total drag values. On the other hand, when the aft wing sweep angle increases the total drag response decreases proportionally. Based on Figure 8.14 Mach number input has the highest influence on the total drag responses. Additionally, it is also shown that the higher Mach values create higher total drag values.

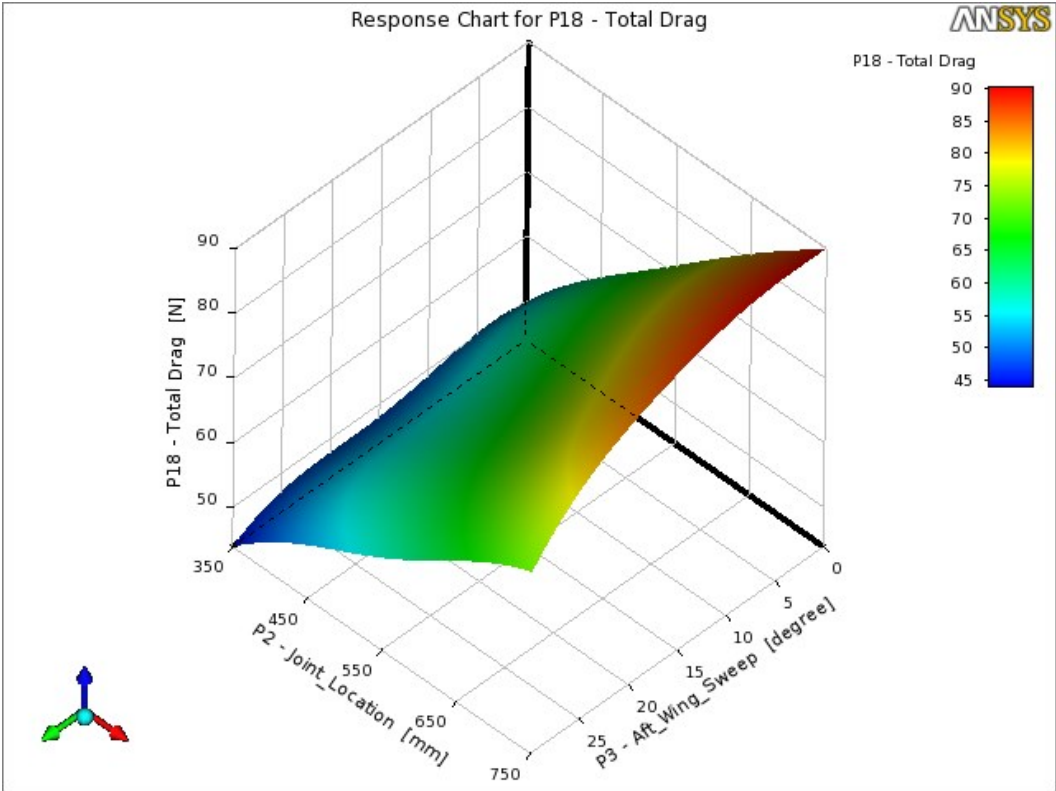


Figure 8.12. Total drag [N] response as a function of joint location and aft wing sweep angle (AOA: 0°, Mach: 0.7)

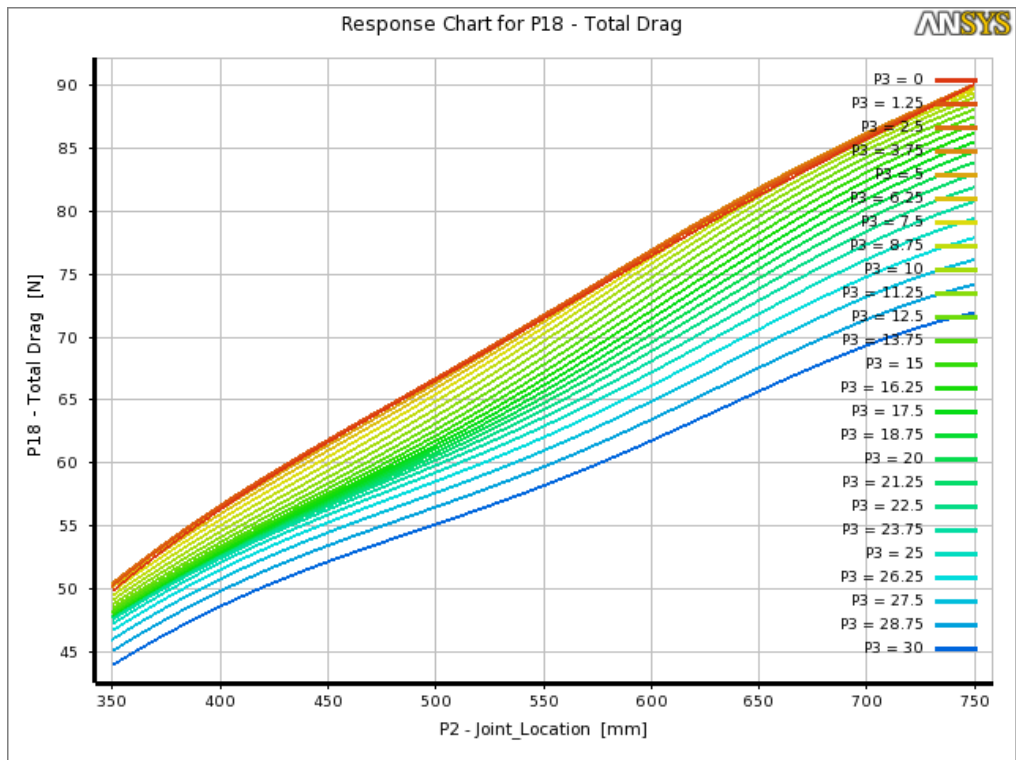


Figure 8.13. 2D slice response chart for total drag [N] as a function of joint location and aft wing sweep angle (AOA: 0°, Mach: 0.7)

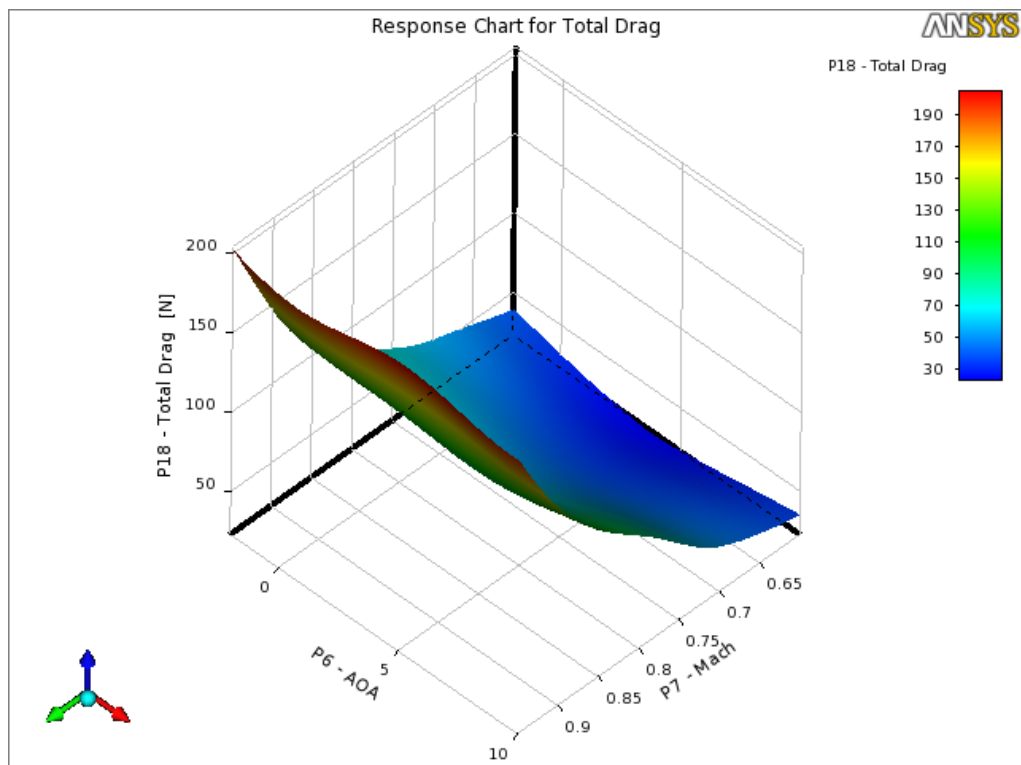


Figure 8.14. Total drag [N] response as a function of Mach number and AOA (joint location: 350 mm, aft wing sweep angle: 0°)

Response surfaces for L/D

In the investigation of the total drag and total lift responses, it is found that the higher lift values can be attained at low joint locations and the total drag decreases while the aft wing angle increases. Similarly, Figures 8.15 and 8.16 show that the lower joint locations with high aft sweep angle lead to the highest L/D value. Meanwhile, Figure 8.17 displays L/D responses as a function of Mach number and AOA. The L/D responses have larger values for lower Mach Numbers but then it peaks up when the AOA values fall in between 2° and 5°.

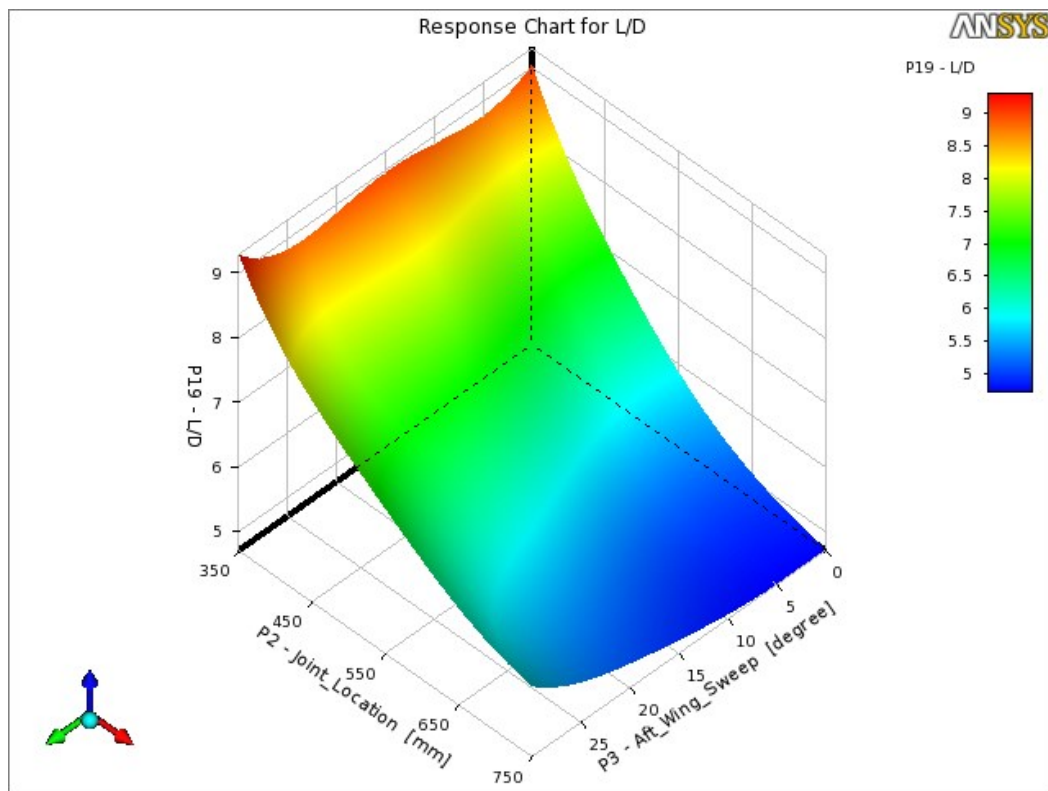


Figure 8.15. L/D response as a function of joint location and aft wing sweep angle (AOA: 0°, Mach: 0.7)

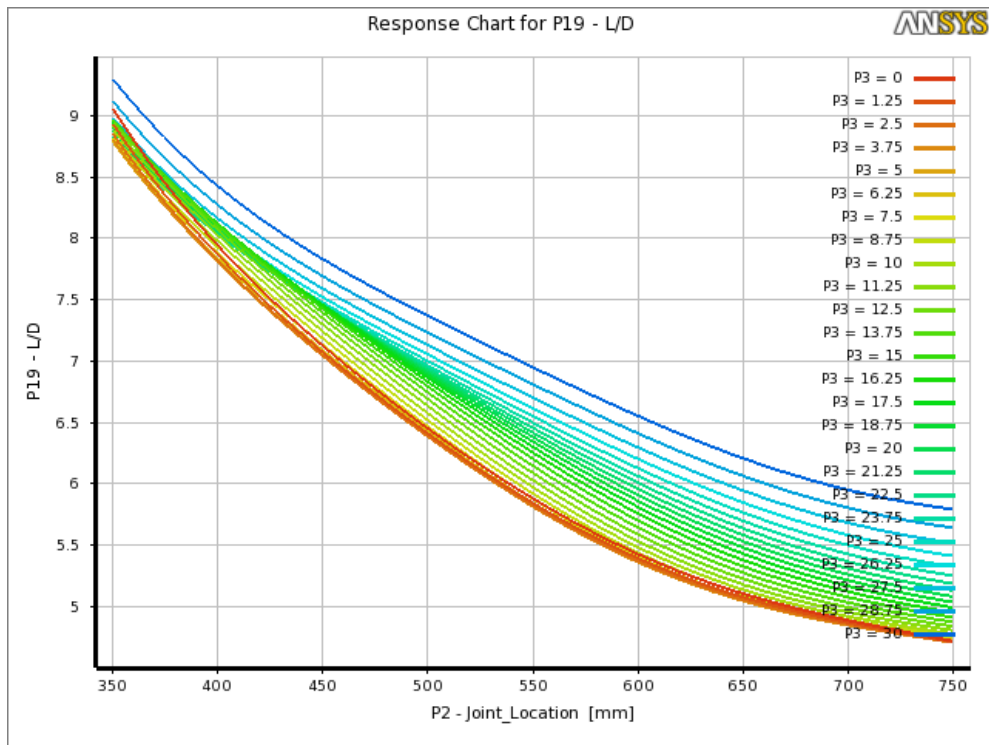


Figure 8.16. 2D slice response chart for L/D as a function of joint location and aft wing sweep angle (AOA: 0° , Mach: 0.7)

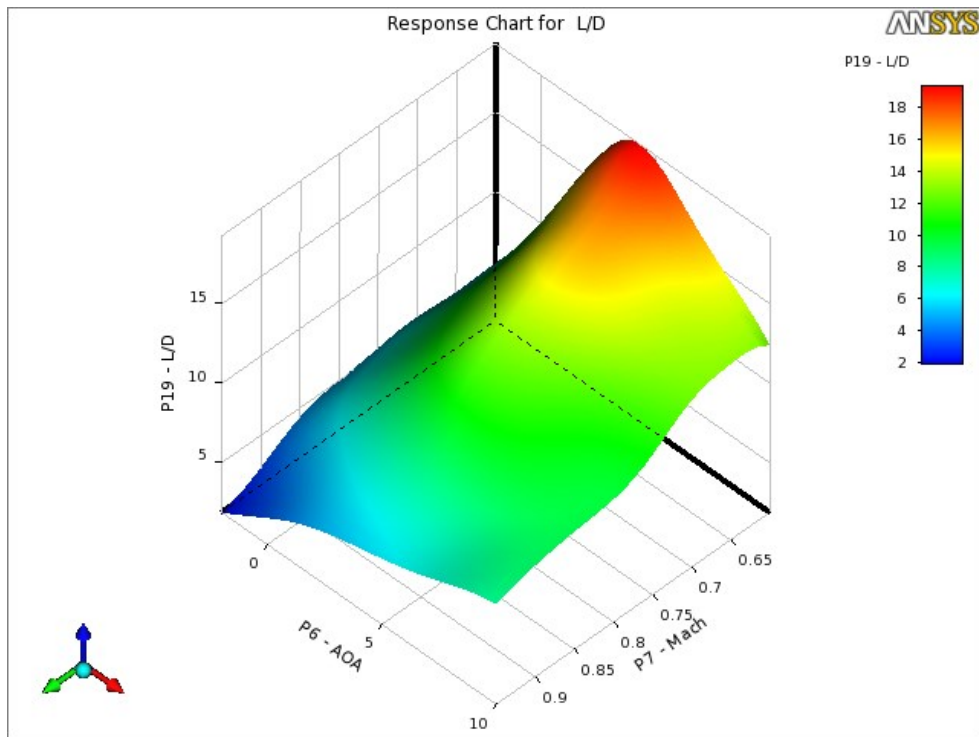


Figure 8.17. L/D response as a function of Mach number and AOA (joint location: 350 mm, aft wing sweep angle: 0°)

Response surfaces for Tip Deflection

As it is presented in Figures 8.18 and 8.19 that the joint location has a significant influence on the tip deflection. It can be concluded that the tip deflection can be minimized by setting joint location somewhere in between 500 mm and 650 mm. The aft wing sweep angle has a minimal influence compared to other input design variables. As it can be seen from Figure 8.20, the shape of the response surface is almost the same as the one in Figure 8.11. The reason is from the fact that an increase in the Mach number and AOA leads to an increment in the total lift response, and therefore, it results in increments in tip deflection responses.

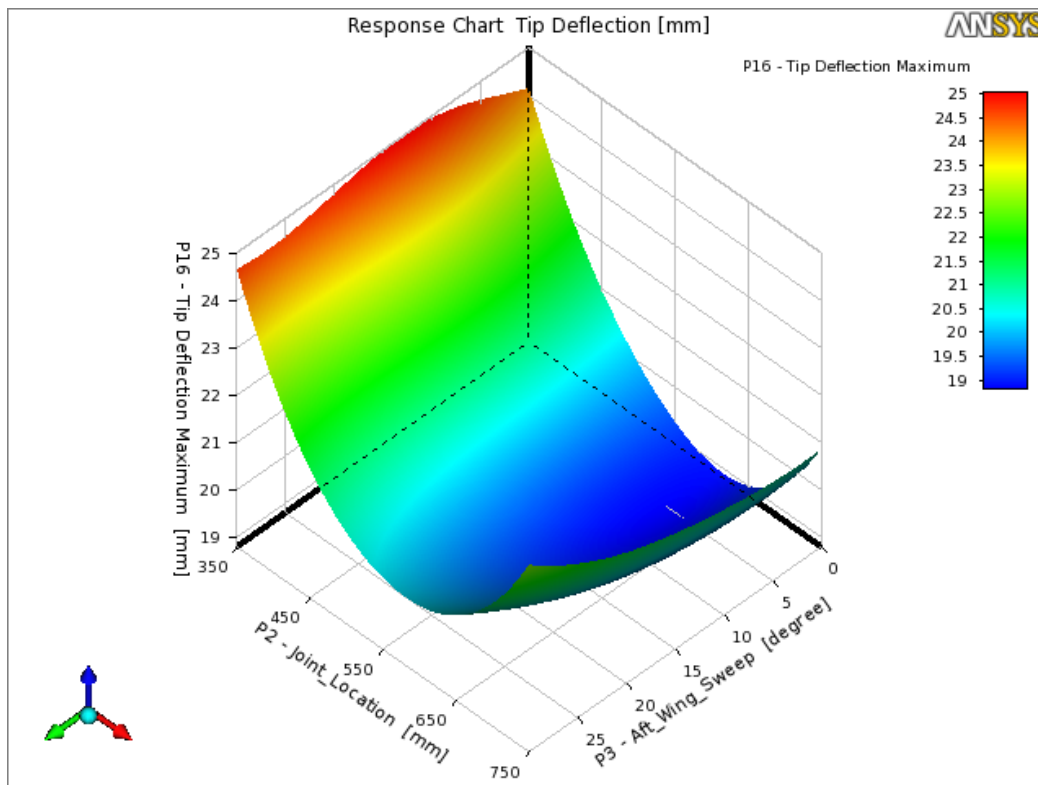


Figure 8.18. Tip deflection [mm] response as a function of joint location and aft wing sweep angle (AOA: 0°, Mach: 0.7)

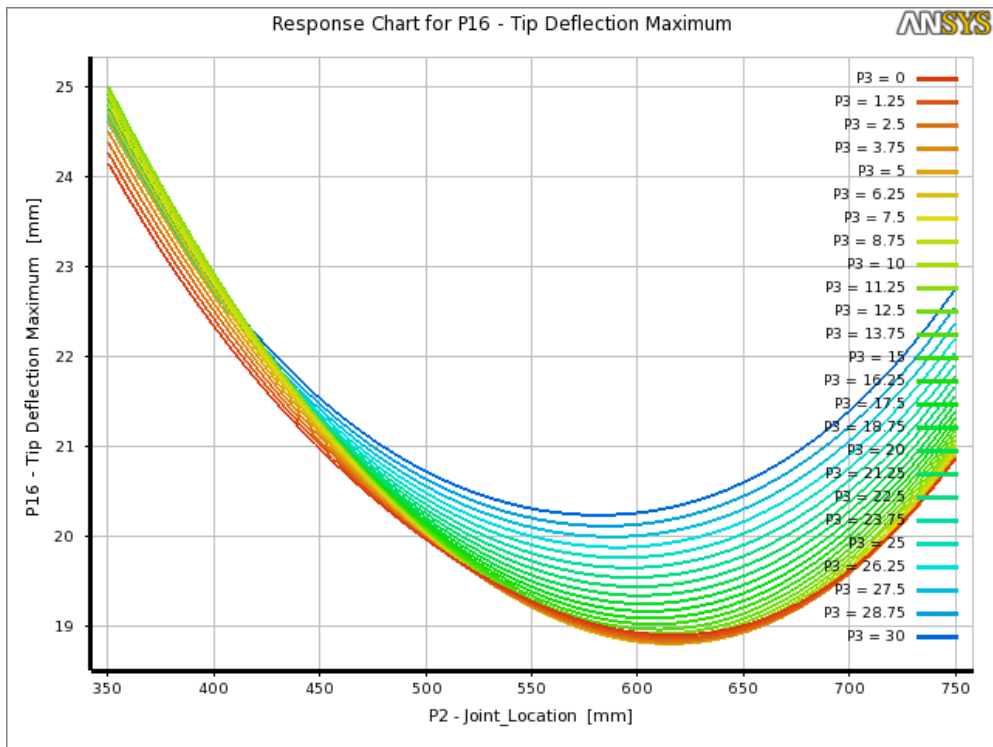


Figure 8.19. 2D slice response chart for Tip Deflection as a function of joint location and aft wing sweep angle (AOA: 0°, Mach: 0.7)

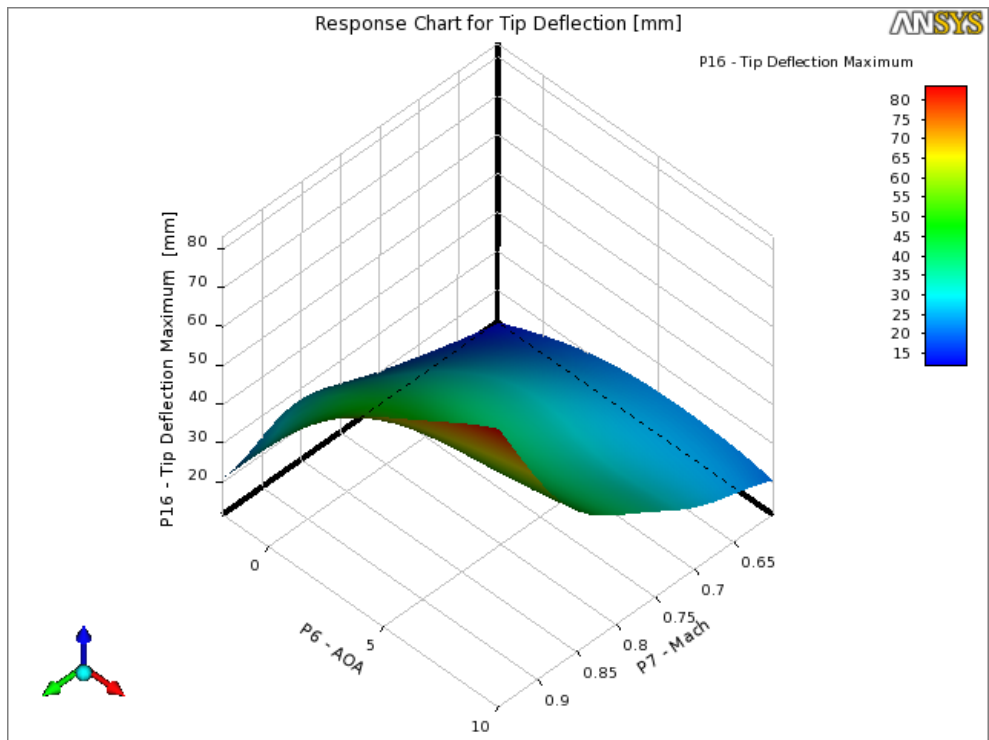


Figure 8.20. Tip deflection [mm] response as a function of Mach number and AOA (joint location: 350 mm, aft wing sweep angle: 0°)

Response surfaces for Maximum Equivalent Stress

The maximum equivalent stress responses are constructed by also observing these values in order to make sure that they are below the structural limits. Figures 8.21 and 8.22 show that the maximum equivalent stress value decreases when the joint location and aft wing sweep angle increase however it increases if the joint location goes beyond the value of 600 mm. Meanwhile, as it can be seen from Figure 8.23, higher Mach number and AOA result in higher values in the maximum equivalent stress responses.

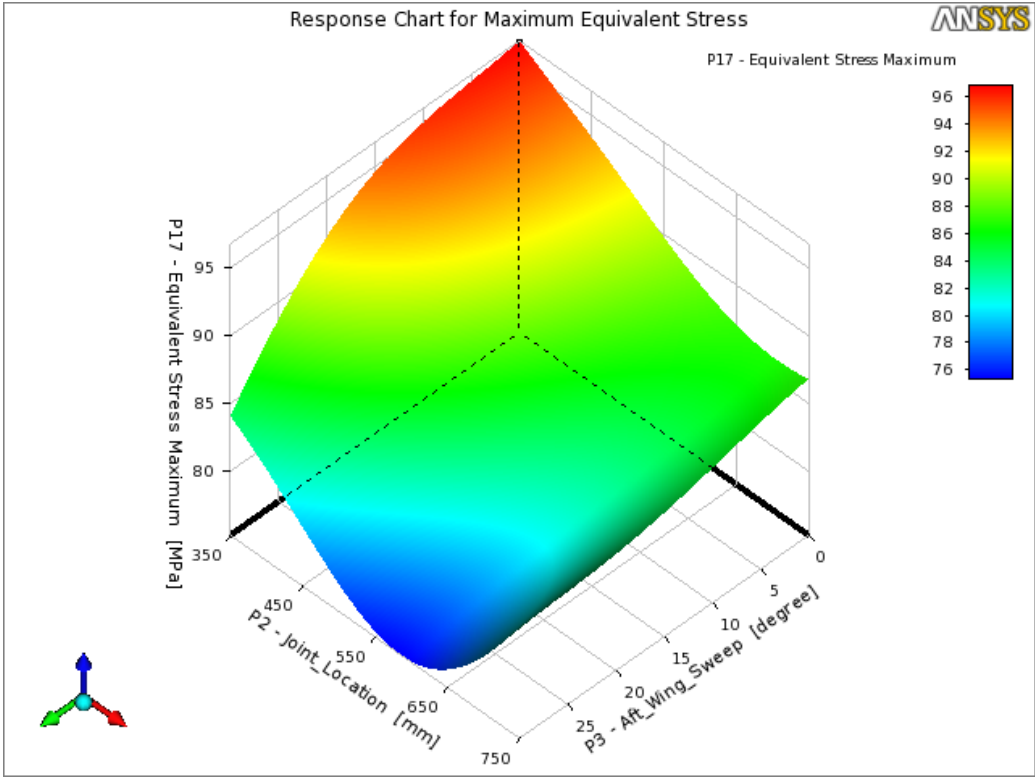


Figure 8.21. Maximum equivalent stress [MPa] response as a function of joint location and aft wing sweep angle (AOA: 0°, Mach: 0.7)

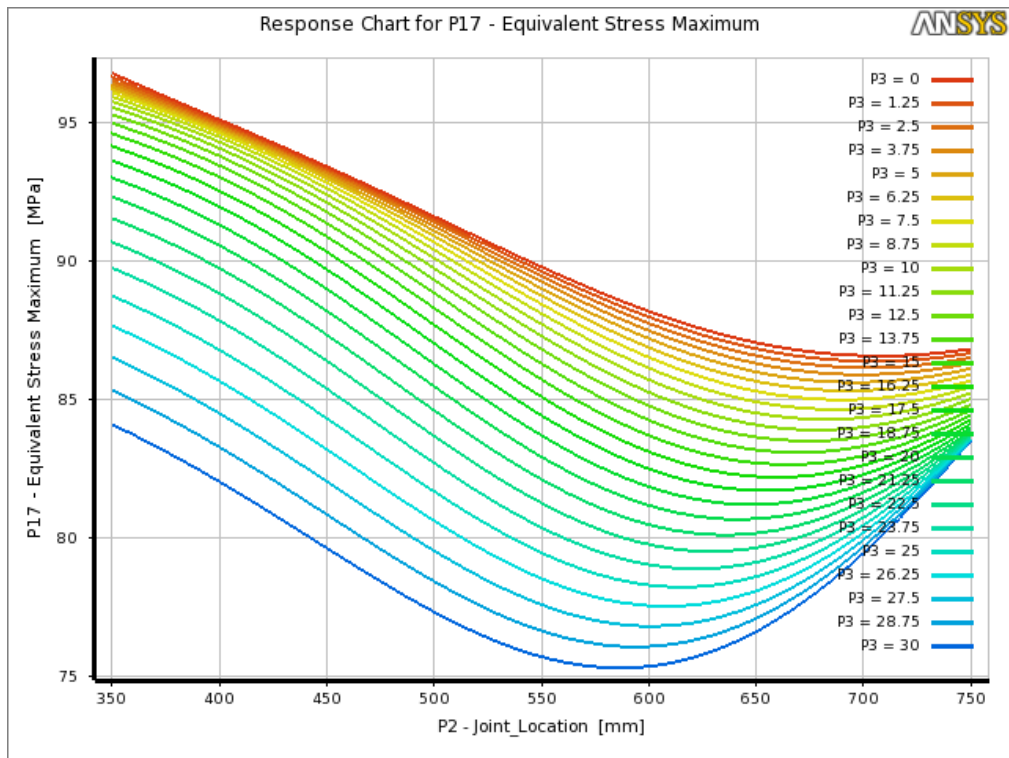


Figure 8.22. 2D slice response chart for Maximum Equivalent Stress as a function of joint location and aft wing sweep angle (AOA: 0°, Mach: 0.7)

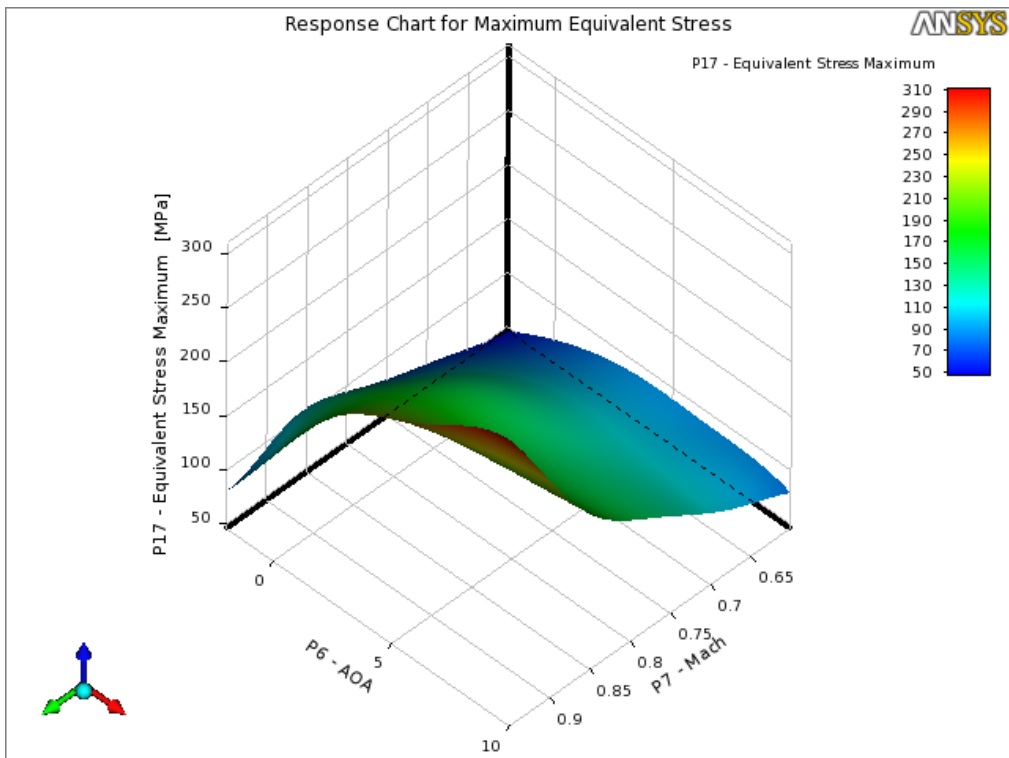


Figure 8.23. Maximum equivalent stress [MPa] response as a function of Mach number and AOA (joint location: 350 mm, aft wing sweep angle: 0°)

Response Surfaces for Weight

Figure 8.24 shows that high joint location and aft wing sweep angle produce a very heavy joined-wing configuration. Since the increment in the joint location and aft wing sweep angle imply a bigger aft wing, it causes an increase in weight. As it can be expected, the Mach number and AOA have no effect on the weight of the joined-wing.

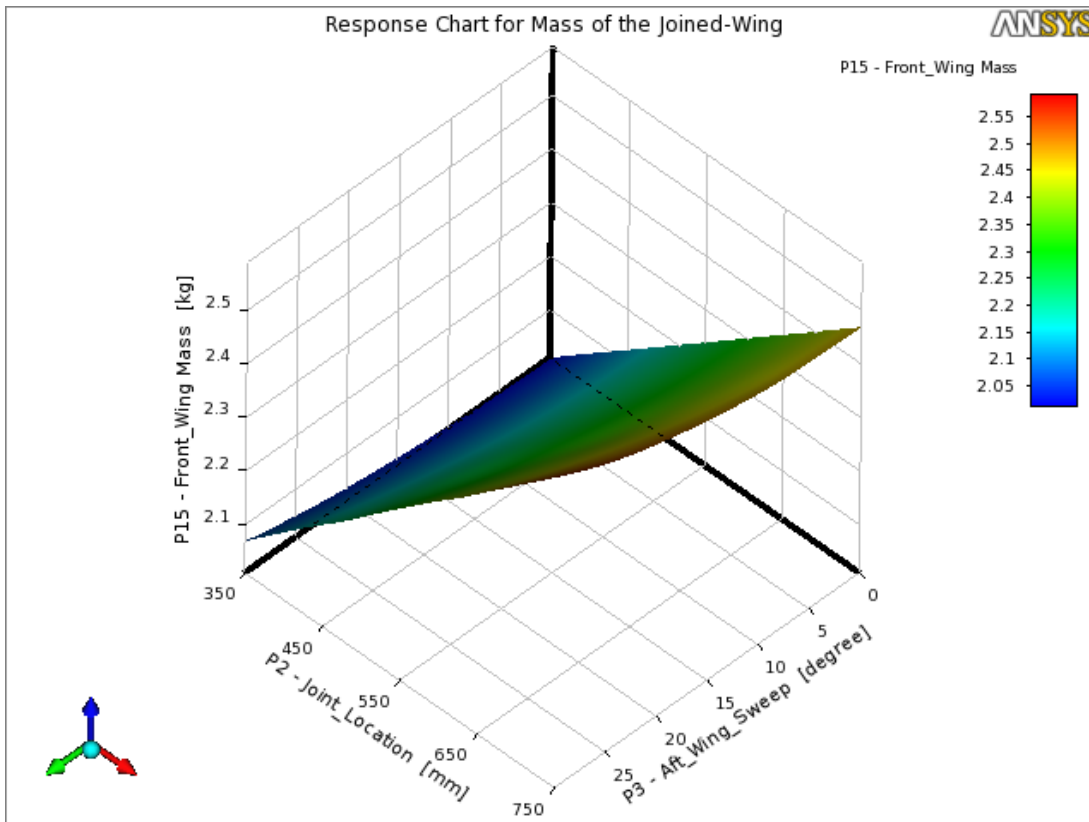


Figure 8.24. Mass of the joined-wing [kg] response as a function of joint location and aft wing sweep angle

8.7 Response Methodology for Dynamic Characteristics of the Joined-Wing

In addition to the MDO analyses, in this section dynamic characteristics of joined-wing configurations are investigated as a separate study by changing two key parameters, namely; aft wing sweep angle and location of the joint.

Understanding both the natural frequencies and the corresponding mode shapes and knowing their effects on the structure helps engineers to design better structures.[35] So, in this study in order to investigate dynamic characteristics of joined-wing configurations; firstly, 9 initial sampling points are determined through LHS (DOE) methods. Secondly, modal analyses are performed for all of the sampling points and natural frequency information is stored. Thirdly, response surfaces are constructed by using kriging model. Then, the accuracy of the created responses is checked through an error criterion, if the requirement of the criterion is not satisfied, a refinement point is inserted into design space and the previous steps are repeated. This procedure continues until the error criterion is fulfilled. Finally, in order to verify response surface models, verification points are inserted and analyzed.

Table 8.8. DOE- LHS points for modal analyses

Design Point #	Input Design Variables		Output Design Variables			
	Joint Location (mm)	Aft Wing Sweep (degree)	1 st Mode [Hz]	2 nd Mode [Hz]	3 rd Mode [Hz]	4 th Mode [Hz]
1	505.56	1.67	22.84	22.97	86.94	87.24
2	638.89	3.89	21.23	21.35	94.79	95.26
3	372.22	0.56	21.42	21.52	83.63	83.91
4	594.44	5	21.96	22.09	94.39	94.99
5	416.67	8.33	22.15	22.26	81.56	81.78
6	727.78	2.78	19.43	19.54	84.5	84.72
7	550	9.44	22.41	22.53	89.53	90.33
8	683.33	7.22	20.27	20.37	90.39	90.76
9	461.11	6.11	22.69	22.81	82.97	83.25

After the modal analyses performed for all of the sampling points, initial response surfaces are created by applying Kriging model. Following this, the auto-refinement procedure is implemented by ANSYS® Design Exploration. In the refinement procedure, maximum %2 of predicted relative error [45] is considered as a convergence criterion. In order to satisfy this error criterion 23 refinement points are automatically inserted into design space. These refinement points can be seen in Appendix D.1.

In this response surface generation, since Kriging model, an interpolated response surface model, is used, it is ensured that the response surface passes through all of the DOE points. To evaluate response surface accuracy, using of verification points to compare the predicted and observed values of the output parameters of the response surface is a better way. For this aim, eight verification points are placed where the distance from existing DOE points and refinement points are maximum. These verification points can be seen in Appendix F.1.

Table 8.9 shows the results of goodness of fit of the response surfaces. In this case, it can be seen that the error values are less than 5%. And it can be said that this error is perfectly adequate for this case.

Table 8.9. Goodness of fit of natural frequency RS for verification points

	1 st Mode [Hz]	2 nd Mode [Hz]	3 rd Mode [Hz]	4 th Mode [Hz]
Maximum Relative Residual (Best Value = 0%)	0.13	0.14	0.11	0.12
Root Mean Square Error (Best Value = 0)	0.01	0.02	0.04	0.04
Relative Root Mean Square Error (Best Value = 0%)	0.06	0.07	0.05	0.04
Relative Maximum Absolute Error (Best Value = 0%)	2.31	2.39	1.93	2.03
Relative Average Absolute Error (Best Value = 0%)	0.82	0.97	0.68	0.43

In order to observe how the geometric parameters affect the vibration characteristics of the joined-wing configurations, response surfaces are constructed and presented based on the definitions listed in Table 8.10. Natural frequency responses corresponding to Mode 1, Mode 2, Mode3 and Mode 4 are given in Figures 8.25, 8.26, 8.27, and 8.28, respectively.

Table 8.10. Description of the free vibration modes

Mode	Description of the free vibration modes
1	Front wing first anti-symmetric out-of-plane bending
2	Front wing first symmetric out-of-plane bending
3	Front wing second anti-symmetric out-of-plane bending, Aft wing first anti-symmetric out-of-plane bending
4	Front wing second symmetric out-of-plane bending, Aft wing first symmetric out-of-plane bending

Figures 8.25 and 8.26 show that “Mode 1” and “Mode 2” have similar tendencies and they peak up when joint location is in between 450 mm and 550 mm. If the influence

of the aft wing sweep angle is considered, it can be seen that it has almost no effect on the natural frequencies.

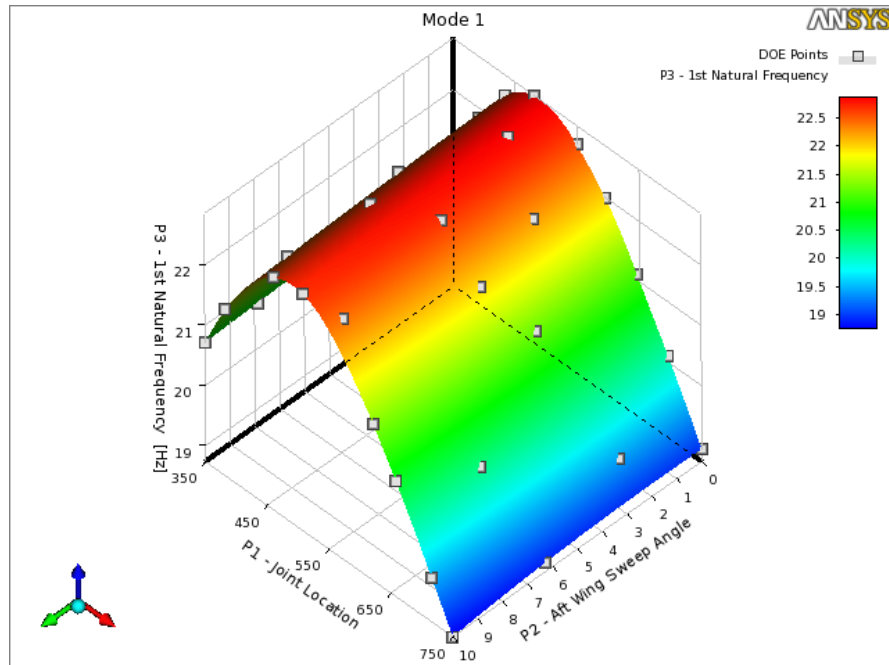


Figure 8.25 Natural frequency responses corresponding to Mode 1 as a function of joint location and aft wing sweep angle

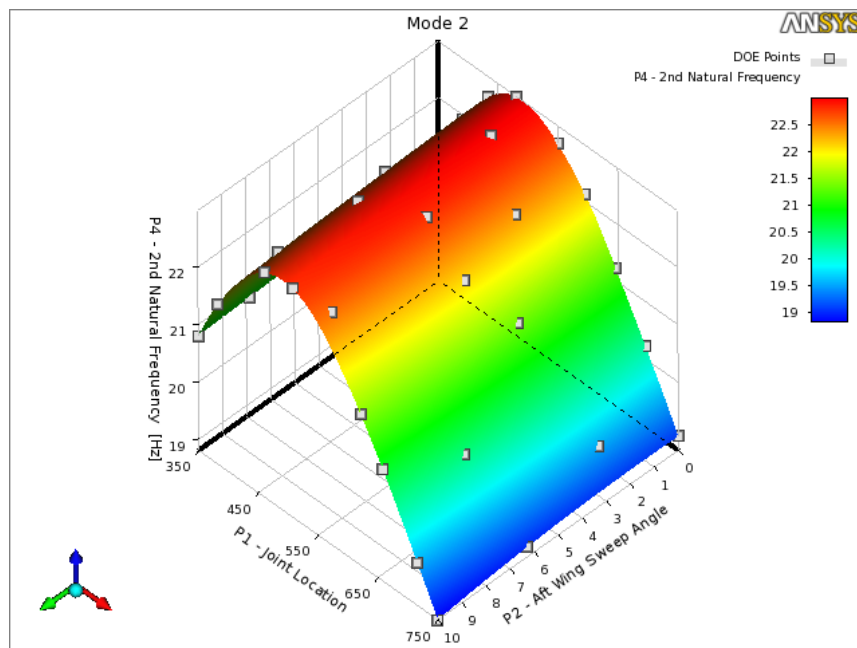


Figure 8.26. Natural frequency responses corresponding to Mode 2 as a function of joint location and aft wing sweep angle

As it can be seen from Figures 8.27 and 8.28, Mode 3 and Mode 4 have similar tendencies; however, their characteristics are completely different from Mode 1 and Mode 2. From these figures, it is observed that joint location has highest influence on Mode 3 and Mode 4. The frequency values are at its absolute minimum and maximum value when the joint location is in between 350 mm - 450 mm and 550mm – 650mm, respectively. On the other hand, the aft wing sweep angle appeared to have a minimal influence on the natural frequencies when compared to the influence of joint location.

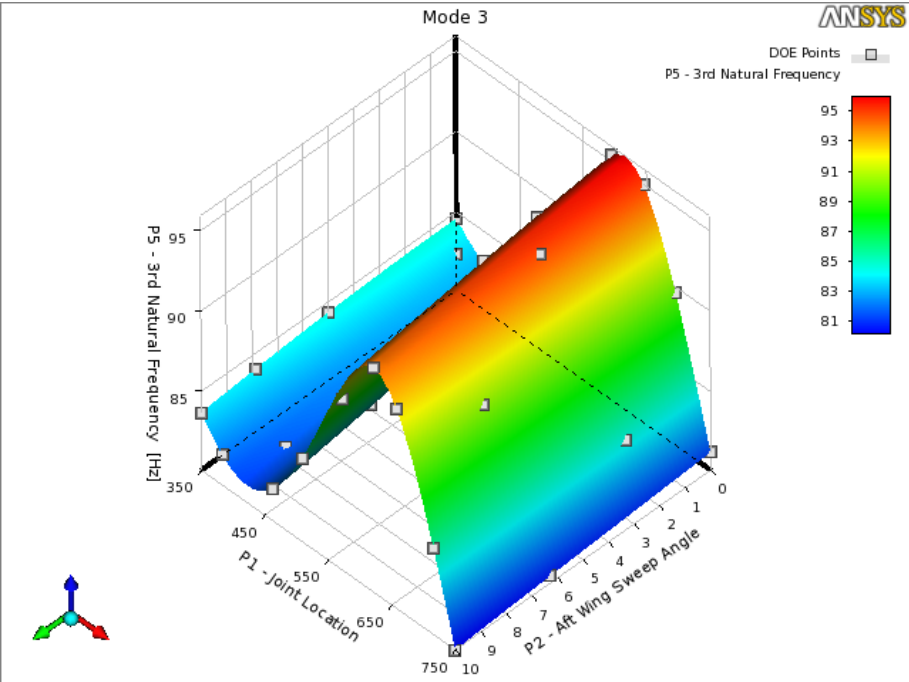


Figure 8.27. Natural frequency responses corresponding to Mode 3 as a function of joint location and aft wing sweep angle

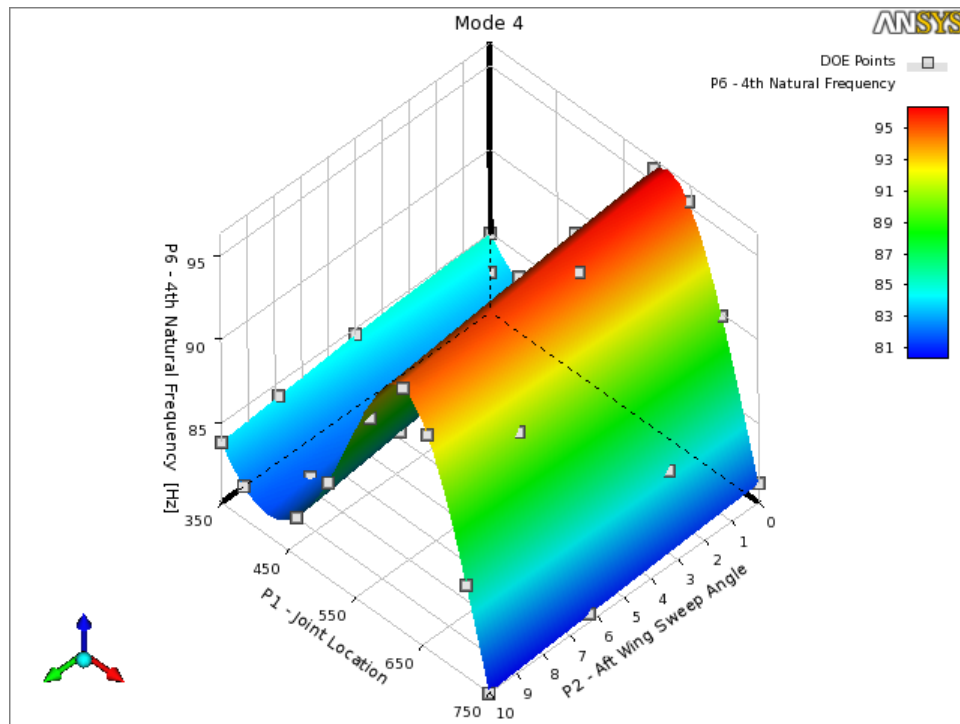


Figure 8.28. Natural frequency responses corresponding to Mode 4 as a function of joint location and aft wing sweep angle

8.8 Application of a Genetic Algorithm

The genetic algorithm mimics the process of natural selection. It can solve both constrained and unconstrained optimization problems. The genetic algorithm uses natural evolution techniques such as crossover, selection and mutation. In this study, Multi Objective Genetic Algorithm (MOGA), a hybrid variant of the NSGA-II (Non-dominated Sorted Genetic Algorithm-II) [52], is used as an optimization tool. In the MOGA the initial population is extracted from response surfaces by using OSF design. Then, a new population is generated via crossover and mutation techniques. Crossover combines two chromosomes (parents) to form a new chromosome (children) for the next generation. Mutation changes one or more gene values in a chromosome from its original state. This new mutated chromosome may lead the genetic algorithm to reach a better solution. This modification of population repeatedly continues until the maximum allowable pareto percentage is reached [45]. The used analysis scheme of ANSYS MOGA algorithm is given at Table 8.10.

Table 8.11. MOGA analysis scheme

	Setup	Optimization Status
Converged	-	Yes
Number of Initial Samples	1000	-
Number of Samples Per Iteration	500	-
Maximum Allowable Pareto Percentage	70	72.5
Number of Evaluations	-	10460

Then, the optimization is performed according to standard formulations which are defined previous sections. Tables 8.10 and 8.11 display results for 1g and 2.5g load conditions, respectively. In the tables 4 different optimizations are seen, the first three ones are single-objective optimizations, their objectives and constrains are defined in the section 8.2.2, the fourth optimization is the combination of these three optimization.

Table 8.12. MOGA results for 1g load condition

Optimization Purpose	Single –Objective Optimization			Single - Objective Optimization		
	Lift Constrained Drag Minimization			Tip Deflection Minimization		
	Candidate Point 1	Candidate Point 1 Verified	Error [%]	Candidate Point 2	Candidate Point 2 Verified	Error [%]
Joint Location (mm)	371.39			610.90		
Aft Wing Sweep (deg.)	29.89			1.25		
AOA (degree)	4.92			9.86		
Mach	0.69			0.67		
Total Lift (N)	588.73	597.52	1.49	588.65	611.87	3.94
Total Drag (N)	32.50	32.81	0.95	72.92	71.38	2.11
Weight (kg)	2.10	2.10	0.00	2.31	2.31	0.00
Tip Deflection (mm)	30.14	31.15	3.35	19.88	21.30	7.14
Eqv. Max. Stress (MPa)	106.96	111.01	3.79	93.70	100.31	7.05
L/D	18.11	18.21	0.55	8.04	8.57	6.59
Optimization Purpose	Single - Objective Optimization			Multi - Objective Optimization		
	Weight Minimization			*L/D Optimization *Tip Deflection Minimization *Weight Minimization		
	Candidate Point 3	Candidate Point 3 Verified	Error [%]	Candidate Point 4	Candidate Point 4 Verified	Error [%]
Joint Location (mm)	350			352.26		
Aft Wing Sweep (deg.)	1.02			2.08		
AOA (degree)	5.01			6.32		
Mach	0.69			0.69		
Total Lift (N)	588.75	595.62	1.17	582.89	588.52	0.97
Total Drag (N)	37.68	38.98	3.45	40.79	42.20	3.46
Weight (kg)	2.01	2.01	0.00	2.01	2.01	0.00
Tip Deflection (mm)	27.87	28.81	3.37	27.12	28.18	3.91
Eqv. Max. Stress (MPa)	114.85	115.47	0.54	112.47	112.82	0.31
L/D	15.82	15.28	3.41	14.56	13.95	4.19

Table 8.13. MOGA results for 2.5 g load condition

Optimization Purpose	Single –Objective Optimization			Single - Objective Optimization		
	L/D Optimization,			Tip Deflection Minimization		
	Candidate Point 1	Candidate Point 1 Verified	Error [%]	Candidate Point 2	Candidate Point 2 Verified	Error [%]
Joint Location (mm)	376.36			626.66		
Aft Wing Sweep (deg.)	29.98			2.26		
AOA (degree)	9.73			9.60		
Mach	0.93			0.93		
Total Lift (N)	1462.27	1428.17	2.33	1465.85	1456.75	0.62
Total Drag (N)	152.37	148.07	2.82	250.66	254.29	1.45
Weight (kg)	2.10	2.10	0.00	2.33	2.33	0.00
Tip Deflection (mm)	79.20	72.62	8.31	56.43	55.20	2.18
Eqv. Max. Stress (MPa)	267.44	265.21	0.83	270.31	261.36	3.31
L/D	9.63	9.65	0.21	5.86	5.73	2.22
Optimization Purpose	Single - Objective Optimization			Multi - Objective Optimization		
	Weight Minimization			*L/D Optimization *Tip Deflection Minimization *Weight Minimization		
	Candidate Point 3	Candidate Point 3 Verified	Error [%]	Candidate Point 4	Candidate Point 4 Verified	Error [%]
Joint Location (mm)	351.78			433.26		
Aft Wing Sweep (deg.)	1.89			15.48		
AOA (degree)	9.30			9.76		
Mach	0.94			0.91		
Total Lift (N)	1471.76	1466.38	0.37	1349.36	1305.28	3.27
Total Drag (N)	178.97	177.72	0.70	166.09	163.30	1.68
Weight (kg)	2.01	2.01	0.00	2.12	2.12	0.00
Tip Deflection (mm)	74.97	72.92	2.73	57.95	53.63	7.45
Eqv. Max. Stress (MPa)	291.57	291.89	0.11	255.17	237.48	6.93
L/D	8.23	8.25	0.24	8.09	7.99	1.24

8.9 Optimization Results for the Joined-Wing Configurations

The local sensitivity analysis for MDO part and the investigation of dynamic characteristics of joined-wings are depicted in Figures 8.29 and 8.30, respectively. Each bar represents the sensitivity intensity of each input (i.e. joint location, aft wing sweep angle, Mach number and AOA) toward the variability of the output variables. As shown in Figure 8.29, Mach number has the highest influenced intensity on all the output variables. In addition to that, the aft wing sweep angle possesses a minimal influence on the overall output responses. The local sensitivity graph for the mode shape response surfaces of the joined-wings is given in Fig.11. As observed from Fig.11, the aft wing sweep angle does not have any influence on the Mode 1 and Mode 2. However, in the Mode 3 and Mode 4, the sensitivity intensity of the aft wing sweep

angle increases. Although, the aft wing sweep angle is getting more effective when compared to its effectiveness in the first two mode, it can be easily seen that the joint location has the highest influenced intensity on all the modes.

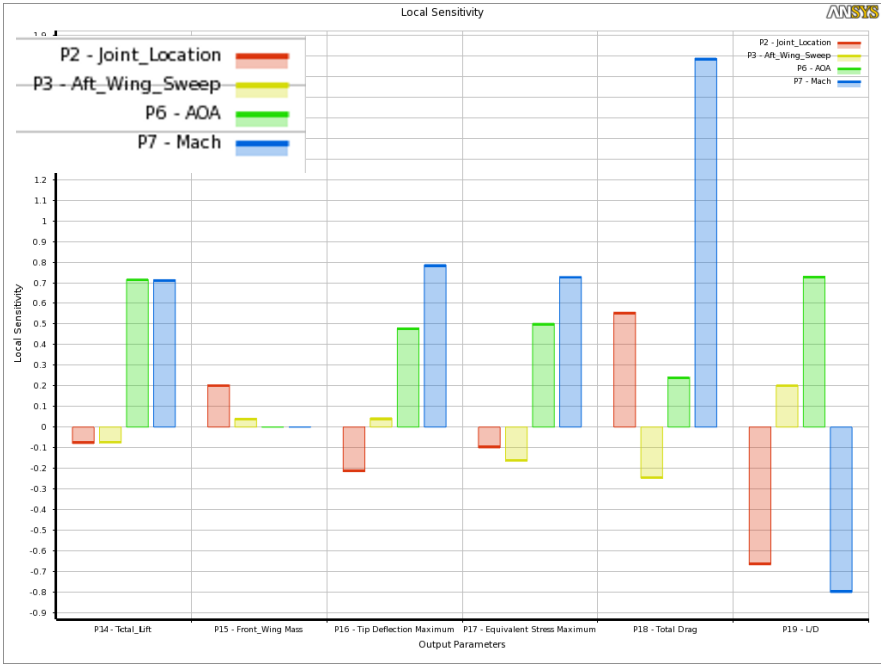


Figure 8.29. Local sensitivity for MDO of joined-wing

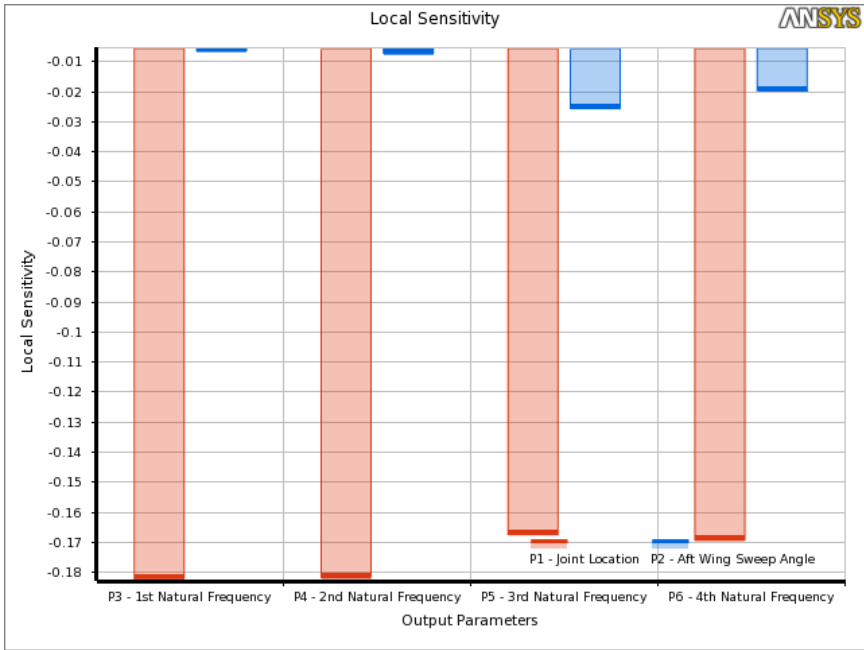


Figure 8.30. Local sensitivity graph for the mode shapes of the joined-wings

8.10 Discussion and Conclusions

In this chapter, the steps followed in the meta-model based multidisciplinary design optimization of the joined-wing configurations are presented. The detailed explanations of the design of experiment and response surface methodology have been made. The influences of the input design parameters (joint location, aft wing sweep angle, Mach number and AOA) on the output design parameters of MDO and mode shapes are also investigated via the genetic algorithm and response surfaces.

The application of genetic algorithm with lift constrained drag as an objective function results in an optimum with lower drag than other objective functions as expected. It is seen that the lower joint-location value and the higher aft wing sweep angle generates lower drag force at 1 g flight condition. These results also show good agreement with the lift to drag response surface graphs. For 2.5 g flight condition, the lower joint-location value and the higher aft wing sweep angle results in lower drag force values as well. The difference between 1 g and 2.5 g flight conditions mainly comes from the aerodynamic input parameters comprising Mach number and AOA as both conditions provide similar geometrical parameters.

For the case of a tip deflection as an objective function, the genetic algorithm finds an optimum with lower tip deflection at almost 600 mm joint location and 1 degree aft wing sweep angle for both 1 g and 2.5 g flight conditions. Similar trend can be seen in Figure 8.19.

The weight of the joined-wing is only depends on the geometrical parameters. Since the Mach number and AOA do not affect the value of the weight, the minimum weight must be at the configuration where both joint-location and aft wing sweep angle are at their lowest values. The result of the genetic algorithm using the weight as an objective function also supports this particular outcome.

In the application of multi-objective genetic algorithm, all objective functions are taken into consideration. It seems that the lower joint-location value is favorable for

the lift constrained drag optimization and the weight as objective functions, therefore the genetic algorithm results with a lower joint-location value for 1g flight condition. On the other hand, for 2.5 g flight condition, the optimum is achieved at joint location of 433 mm and aft wing sweep angle of 15 degree. This optimum point appears in between the optimum points obtained from the single-objective optimization results where the tip deflection and the lift-constrained drag used as an individual objective function.

Furthermore, according to genetic algorithm results, it is feasible to choose 0.69 Mach and 5 to 6 degree AOA for cruise condition. For 2.5 g flight condition, on the other hand, 0.93 Mach and 9.5 degree AOA seem to be the ideal candidates for all the objective functions.

CHAPTER 9

CONCLUSIONS

9.1 General Conclusions

In this thesis, after dynamic characteristics of the joined-wing configurations are investigated and their experimental validations are performed through the classical modal analyses techniques, a high-fidelity loosely coupled MDO of the joined-wing is elucidated with a hybrid MOGA and RSM. In consideration of the 3-D aerodynamic analyses, RANS simulations with Spalart-Allmaras model are used for turbulence closure. Then, the structural analyses are performed under aerodynamic loading. As the high fidelity models in both aerodynamic and structural analyses make the optimization process computationally expensive, the use of the response surfaces with sophisticated kriging model helps to reduce the cost and it provides designers to quickly define the design trends and the optimal regions.

In this study, it is observed from the obtained maximum RMS error values of the response surfaces that an accurate surrogate model is achieved and it is used as a replacement for the computationally expensive analyses. In addition to that various verification points are created and analyses are then repeated. As it can be seen from the validated MOGA results, the percentage error between the results of the empirical model and that of the analyses is observed to be less than 7.5.

For the optimizations of the response surfaces, the genetic algorithms are also introduced and single and multi-objective design optimizations are performed. It is observed that the single-objective optimizations provide better results for the interested objective (i.e. one of the aforementioned objectives such as; “lift constrained drag minimization”, “tip deflection minimization” and “weight minimization”). However, it produces moderate performance for the remaining objectives. On the other

hand, the multi-objective design optimization tries to meet all the design objectives. In this study, since the tip deflection has a great influence in both structural stability and aerodynamic efficiency, it is considered as important as the L/D and weight objective. It is also ensured that the stress levels do not exceed the elastic limits of the structure at all design points. As a general conclusion, the use of a high fidelity multi-disciplinary analysis with statistical approaches leads to more realistic results in an efficient way.

9.2 Recommendations for Future Work

In this thesis, after the dynamic characteristic of the joined-wings are investigated through both Finite Element Analyses and Classical Modal Analyses, a meta-model based MDO of the joined-wings is performed with hybrid MOGA and RSM.

The recommendations for the future work of this study can be listed as follows:

- In this study, MDO part of the study is performed based on loosely coupled analyses, however, with a superior computational capability the joined-wing configurations can be investigated by including the aeroelastic effects both in sensitivity and analysis levels.
- In addition to the joint location and aft wing sweep angle variables, various more input design variables such as front wing sweep, dihedral angle, taper ratio, thickness of wings, etc. can be included in the optimization study.
- Aerodynamic shape optimization study for both aft and front wing airfoils could also be performed.
- The buckling should also be considered as a design constraint in the further optimization routines.

REFERENCES

- [1] J. Wolkovitch, “The joined wing - An overview,” *J. Aircr.*, vol. 23, no. 3, pp. 161–178, 1985.
- [2] J. Wolkovitch, “Subsonic VSTOL Aircraft Configurations with Tandem Wings,” *Journal of Aircraft*, vol. 16, pp. 605–611, 1979.
- [3] “Above Top Secret [Online] [Cited: 06 June 2015] <http://www.abovetopsecret.com/forum/thread192824/pg1>.” .
- [4] J. R. R. A. Martins and A. B. Lambe, “Multidisciplinary Design Optimization: A Survey of Architectures,” *AIAA J.*, vol. 51, no. 9, pp. 2049–2075, 2013.
- [5] G. P. Guruswamy and S. Obayashi, “Study on the Use of High-Fidelity Methods in Aeroelastic Optimization,” *Journal of Aircraft*, vol. 41, no. 3, pp. 616–619, 2004.
- [6] J. R. R. A. Martins, J. J. Alonso, and J. J. Reuther, “A Coupled-Adjoint Sensitivity Analysis Method for High-Fidelity Aero-Structural Design,” *Optim. Eng.*, vol. 6, pp. 33–62, 2005.
- [7] B. Iooss and P. Lemaître, “A review on global sensitivity analysis methods,” *arXiv Prepr. arXiv1404.2405*, p. 23, 2014.
- [8] Y. Kim, Y.-H. Jeon, and D.-H. Lee, “Multi-Objective and Multidisciplinary Design Optimization of Supersonic Fighter Wing,” *Journal of Aircraft*, vol. 43, no. 3, pp. 817–824, 2006.
- [9] M. Blair and R. A. Canfield, “A Joined-Wing Structural Weight Modeling Study,” in *43rd AIAA/ASME/ASCE/AHS/ASC Structures, Structural Dynamics, and Materials Conference*, 2002.
- [10] F. T. Johnson, “A general panel method for the analysis and design of arbitrary configurations in incompressible flows,” *NASA CR-3079*, 1980.
- [11] W. Q. Wang and Y. Yan, “Strongly coupling of partitioned fluid-solid interaction solvers using reduced-order models,” *Applied Mathematical Modelling*, vol. 34, no. 12, pp. 3817–3830, 2010.
- [12] J. Van Muijden, B. B. Prananta, and R. P. G. Veul, “Efficient Aeroelastic Simulation in a Parametric Procedure for Fatigue Analysis,” *26th International Congress of the Aeronautical Sciences*. pp. 1–10, 2008.

- [13] D. E. Raveh and M. Karpel, "Structural Optimization of Flight Vehicles with Computational-Fluid-Dynamics-Based Maneuver Loads," *Journal of Aircraft*, vol. 36, no. 6. pp. 1007–1015, 1999.
- [14] G. K. W. Kenway and J. R. R. A. Martins, "Multipoint High-Fidelity Aerostructural Optimization of a Transport Aircraft Configuration," *J. Aircr.*, vol. 51, no. 1, pp. 144–160, 2014.
- [15] V.B.Venkayya, "Structural Optimization: A review and some recommendations," *Int. J. Numer. Methods Eng.*, vol. 13, pp. 203–228, 1978.
- [16] S. Venkataraman and R. T. Haftka, "Structural optimization complexity: What has Moore's law done for us?," *Structural and Multidisciplinary Optimization*, vol. 28, no. 6. pp. 375–387, 2004.
- [17] J. Telford, "A brief introduction to design of experiments," *Johns Hopkins apl technical digest*, vol. 27, no. 3. pp. 224–232, 2007.
- [18] R. A. Fisher, "Design of Experiments," *Analytic Methods for Design Practice*. 1935.
- [19] G. E. P. Box and N. R. Draper, "Empirical Model-Building and Response Surfaces," *Wiley*. 1987.
- [20] M. Papila and R. T. Haftka, "Response approximations - Noise, error repair, modeling errors," *AIAA Journal*, vol. 38. pp. 2336–2343, 2000.
- [21] M. J. Alvarez, L. Ilzarbe, E. Viles, and M. Tanco, "The Use of Genetic Algorithms in Response Surface Methodology," *Qual. Technol. Quant. Manag.*, vol. 6, no. 3, pp. 295–307, 2009.
- [22] A. Oyama, S. Obayashi, K. Nakahashi, and T. Nakamura, "Aerodynamic Optimization of Transonic Wing Design Based on Evolutionary Algorithm," in *Third International Conference on Nonlinear Problems in Aviation and Aerospace*, 2000.
- [23] R. T. Haftka, J. Sobieszczanski-Sobieski, and S. L. Padula, "On options for interdisciplinary analysis and design optimization," *Structural Optimization*, vol. 4. pp. 65–74, 1992.
- [24] J. R. R. a. Martins and C. Marriage, "An Object-Oriented Framework for Multidisciplinary Design Optimization." 2007.
- [25] I. Kroo, "Distributed Multidisciplinary Design and Collaborative Optimization," *Optimization Methods & Tools for Multicriteria/Multidisciplinary Design*. p. 22, 2004.
- [26] *ANSYS Mechanical User 's Guide*, vol. 15317, no. November. 2013.

- [27] G. Forbes and M. Caresta, “Brüel & Kjær Pulse Labshop Primer,” 2009.
- [28] Vibrant Technology, “ME’scopeVES 5.0 - Reference Manual - Basic Operations,” vol. IIA,. August, 2008.
- [29] P. Avitabile, “Experimental Modal Analysis A Simple Non-Mathematical Presentation,” *Sound Vib.*, 2002.
- [30] M. Rider, *Designing with Creo Parametric 2.0*. SDC Publications.
- [31] D. J. Ewins, *Modal Testing: Theory, Practice and Application, 2nd Edition*. Wiley, 2009.
- [32] Brüel&Kjaer, *Product Catalogue- Accelerometer&Conditioning*. 2009.
- [33] Brüel&Kjaer, *Product Catalogue- Analyser Solutions*. 2015.
- [34] Brüel&Kjaer, “Instruction Manuel-Power Amplifier Type 2712.pdf.” 1977.
- [35] P. Avitabile, “Modal Space - In our little world is there any difference between a modal test with a shaker excitation or impact excitation?,” 1998.
- [36] P. Pick, “Lessons Learned in Modal Testing Series,” no. October. pp. 48–56, 2006.
- [37] P. Spalart and S. Allmaras, “A one-equation turbulence model for aerodynamic flows,” *AIAA paper*, no. 92–0439. pp. 5–21, 1992.
- [38] R. K. Duggirala, C. J. Roy, and J. A. Schetz, “Analysis of Interference Drag for Strut-Strut Interaction in Transonic Flow,” *AIAA Journal*, vol. 49, no. 3. pp. 449–462, 2011.
- [39] *ANSYS Fluent User’s Guide: Release 15*. 2013.
- [40] C. Harris, “NASA supercritical airfoils,” *Nasa Tp*. 1990.
- [41] *ANSYS Design Modeler User’s Guide: Release 15*. 2013.
- [42] *ANSYS Meshing User’s Guide: Release 15*. 2013.
- [43] I. J. Keshtiban, F. Belblidia, and M. F. Webster, “Compressible flow solvers for low Mach number flows – a review,” *Technical Report CSR2, Institute of Non-Newtonian Fluid Mechanics, University of Wales*. pp. 1–12, 2004.
- [44] John W. Slater, “RAE 2822 Transonic Airfoil: Study #4,” 2002.
- [45] ANSYS, “Design Exploration User’s Guide,” vol. 15317, no. November. pp. 724–746, 2013.

- [46] B. Alanbay and M. Sahin, “Structural Optimizations of Joined-Wing Kits,” in *CASI AERO*, 2015.
- [47] R. T. Haftka and Z. Gürdal, “Elements of Structural Optimization,” *Elements of Structural Optimization*, vol. 11. p. 481, 1992.
- [48] J. . Anderson, *Aircraft Performance and Design*, 4th editio. McGraw Hill, 1999.
- [49] M. H. Shirk, T. J. Hertz, and T. A. Weisshaar, “Aeroelastic Tailoring — Theory , Practice , and Promise,” *J. Aircr.*, vol. 23, no. 1, 1985.
- [50] “NIST/SEMATECH e-Handbook of Statistical Methods.” [Online]. Available: <http://www.itl.nist.gov/div898/handbook/>. [Accessed: 25-Nov-2015].
- [51] T. D. Canonsburg, “ANSYS Design Exploration,” vol. 15317. pp. 724–746, 2009.
- [52] K. Deb, A. Pratap, S. Agarwal, and T. Meyarivan, “A fast and elitist multiobjective genetic algorithm: NSGA-II,” *IEEE Trans. Evol. Comput.*, vol. 6, no. 2, pp. 182–197, 2002.

APPENDIX A

MESH INDEPENDENCY CHECK FOR FINITE ELEMENT ANALYSIS

Six different mesh densities are used for the finite element model of the joined-wings to ensure that the results are independent from the mesh densities. The first six natural frequencies of the Design Point 1 for different mesh densities and the percentage difference from the highest mesh density are presented in Table A.1 and Table A.2 respectively.

Table A.1. The first six natural frequencies of the Design Point1 for different mesh densities

#	Global Mesh Size (mm)	Node Number	Element Number	Natural Frequencies [Hz]					
				Mode 1	Mode 2	Mode 3	Mode 4	Mode 5	Mode 6
1	10	169542	89144	21.015	21.145	85.184	85.792	185.678	195.384
2	8	185838	98305	20.869	21.001	84.801	85.400	184.996	194.740
3	5	312709	177243	20.874	21.002	84.747	85.338	186.967	196.835
4	4	462653	275231	20.842	20.969	84.617	85.202	187.495	197.441
5	3	873706	551530	20.837	20.965	84.626	85.215	187.489	197.488
6	2	2485227	1673058	20.817	20.945	84.559	85.149	187.380	197.442

Table A.2. Percentage difference from the highest mesh density (i.e. Global mesh size of 2mm)

#	Global Mesh Size (mm)	Node Number	Element Number	Percentage Difference From the Highest Mesh Density					
				Mode 1	Mode 2	Mode 3	Mode 4	Mode 5	Mode 6
1	10	169542	89144	+0.954	+0.957	+0.738	+0.755	-0.909	-1.042
2	8	185838	98305	+0.249	+0.268	+0.286	+0.295	-1.272	-1.368
3	5	312709	177243	+0.277	+0.272	+0.222	+0.221	-0.221	-0.307
4	4	462653	275231	+0.122	+0.116	+0.069	+0.062	+0.061	-0.001
5	3	873706	551530	+0.096	+0.094	+0.079	+0.077	+0.058	+0.024

APPENDIX B

SAMPLING DESIGN AND VERIFICATION POINTS FOR MDO

In the MDO part of the study, FCCCD, BBD, LHS, OSF, Sparse Grid designs are used to generate sampling design points for four input parameters. These sample points are listed in Tables B.1-B.5. In order to assess accuracies of the RS, verification points are generated and used through the goodness of fit studies. These verification points are listed in Table B.6

Table B.1. FCCCD for the MDO of joined-wing

Design Point #	Input Design Variables				Output Design Variables					
	Joint Location (mm)	Aft Wing Sweep (degree)	AOA (degree)	Mach Number	Total Lift (N)	Total Drag (N)	L/D	Tip Deflection (mm)	Equivalent Stress (MPa)	Mass (Kg)
1	550.00	15.00	4.00	0.77	765.94	79.66	9.62	29.83	137.60	2.26
2	350.00	15.00	4.00	0.77	761.96	55.49	13.73	38.49	151.58	2.02
3	750.00	15.00	4.00	0.77	777.63	104.84	7.42	33.56	132.10	2.50
4	550.00	0.00	4.00	0.77	770.69	87.60	8.80	29.51	141.48	2.24
5	550.00	30.00	4.00	0.77	746.36	67.24	11.10	32.01	125.41	2.33
6	550.00	15.00	-2.00	0.77	363.06	99.76	3.64	17.49	79.03	2.26
7	550.00	15.00	10.00	0.77	838.42	101.62	8.25	30.53	141.50	2.26
8	550.00	15.00	4.00	0.60	423.09	31.17	13.57	17.51	80.22	2.26
9	550.00	15.00	4.00	0.95	1121.10	243.16	4.61	49.69	226.68	2.26
10	350.00	0.00	-2.00	0.60	216.69	39.46	5.49	11.74	46.49	2.01
11	750.00	0.00	-2.00	0.60	213.98	64.76	3.30	10.66	45.57	2.47
12	350.00	30.00	-2.00	0.60	187.37	33.86	5.53	11.97	39.58	2.07
13	750.00	30.00	-2.00	0.60	178.40	51.85	3.44	10.14	37.71	2.59
14	350.00	0.00	10.00	0.60	468.16	37.33	12.54	21.12	84.39	2.01
15	750.00	0.00	10.00	0.60	469.57	58.77	7.99	16.90	72.25	2.47
16	350.00	30.00	10.00	0.60	458.15	32.10	14.27	22.96	79.00	2.07
17	750.00	30.00	10.00	0.60	458.31	52.14	8.79	19.71	81.44	2.59
18	350.00	0.00	-2.00	0.95	337.55	197.76	1.71	15.59	64.84	2.01
19	750.00	0.00	-2.00	0.95	397.60	333.53	1.19	21.93	91.73	2.47
20	350.00	30.00	-2.00	0.95	375.88	135.79	2.77	24.80	81.57	2.07
21	750.00	30.00	-2.00	0.95	342.34	209.73	1.63	23.68	79.23	2.59
22	350.00	0.00	10.00	0.95	1586.00	189.09	8.39	81.91	308.52	2.01
23	750.00	0.00	10.00	0.95	1628.20	314.02	5.19	67.38	296.28	2.47
24	350.00	30.00	10.00	0.95	1558.67	154.02	10.12	89.37	288.11	2.07
25	750.00	30.00	10.00	0.95	1605.35	228.10	7.04	78.74	292.62	2.59

Table B.2. BBD for the MDO of the joined-wing

Design Point #	Input Design Variables				Output Design Variables					
	Joint Location (mm)	Aft Wing Sweep (degree)	AOA (degree)	Mach Number	Total Lift (N)	Total Drag (N)	L/D	Tip Deflection (mm)	Equivalent Stress (MPa)	Mass (Kg)
1	550.00	15.00	4.00	0.77	765.94	79.66	9.62	29.83	137.60	2.26
2	350.00	0.00	4.00	0.77	772.05	59.87	12.90	36.51	149.64	2.01
3	750.00	0.00	4.00	0.77	786.78	114.55	6.87	32.15	137.28	2.47
4	350.00	30.00	4.00	0.77	751.60	47.74	15.74	40.25	139.90	2.07
5	750.00	30.00	4.00	0.77	771.55	84.02	9.18	37.65	149.13	2.59
6	550.00	15.00	-2.00	0.60	194.40	48.58	4.00	9.31	41.84	2.26
7	550.00	15.00	10.00	0.60	470.58	46.86	10.04	16.76	77.09	2.26
8	550.00	15.00	-2.00	0.95	355.21	244.71	1.45	17.81	79.75	2.26
9	550.00	15.00	10.00	0.95	1601.45	242.78	6.60	66.18	303.18	2.26
10	350.00	15.00	4.00	0.60	419.43	19.99	20.99	22.35	86.23	2.02
11	750.00	15.00	4.00	0.60	433.03	41.33	10.48	19.65	77.41	2.50
12	350.00	15.00	4.00	0.95	1115.92	186.98	5.97	63.07	240.18	2.02
13	750.00	15.00	4.00	0.95	1167.36	302.72	3.86	55.56	223.96	2.50
14	550.00	0.00	-2.00	0.77	389.01	106.55	3.65	18.76	87.02	2.24
15	550.00	30.00	-2.00	0.77	349.18	84.95	4.11	17.80	69.57	2.33
16	550.00	0.00	10.00	0.77	851.20	107.92	7.89	29.76	143.47	2.24
17	550.00	30.00	10.00	0.77	808.85	91.00	8.89	32.26	127.11	2.33
18	350.00	15.00	-2.00	0.77	370.25	74.36	4.98	22.07	82.93	2.02
19	750.00	15.00	-2.00	0.77	354.37	125.96	2.81	18.24	73.53	2.50
20	350.00	15.00	10.00	0.77	811.67	78.35	10.36	38.49	150.02	2.02
21	750.00	15.00	10.00	0.77	847.37	124.04	6.83	33.49	134.38	2.50
22	550.00	0.00	4.00	0.60	426.75	33.40	12.78	17.30	82.02	2.24
23	550.00	30.00	4.00	0.60	417.46	26.67	15.65	18.98	73.76	2.33
24	550.00	0.00	4.00	0.95	1155.65	265.57	4.35	51.13	239.11	2.24
25	550.00	30.00	4.00	0.95	1100.27	194.77	5.65	52.50	205.04	2.33

Table B.3. LHS for the MDO of the joined-wing

Design Point #	Input Design Variables				Output Design Variables					
	Joint Location (mm)	Aft Wing Sweep (degree)	AOA (degree)	Mach Number	Total Lift (N)	Total Drag (N)	L/D	Tip Deflection (mm)	Equivalent Stress (MPa)	Mass (Kg)
1	550.00	12.60	-1.28	0.76	409.81	94.71	4.33	19.27	88.07	2.25
2	614.00	21.00	5.92	0.75	711.93	76.63	9.29	28.35	119.93	2.36
3	358.00	15.00	7.84	0.66	548.90	37.90	14.48	26.76	104.24	2.03
4	582.00	28.20	4.48	0.73	678.63	57.73	11.75	28.90	114.73	2.36
5	390.00	5.40	1.12	0.87	805.97	125.18	6.44	41.38	174.47	2.06
6	726.00	18.60	0.64	0.90	751.04	201.32	3.73	38.40	151.63	2.48
7	566.00	22.20	6.40	0.89	1003.77	141.55	7.09	40.11	174.51	2.31
8	710.00	7.80	4.96	0.77	782.55	108.52	7.21	31.20	134.73	2.43
9	470.00	23.40	1.60	0.85	813.89	102.04	7.98	39.71	165.82	2.19
10	438.00	6.60	9.76	0.94	1535.85	209.92	7.32	68.41	305.92	2.11
11	502.00	3.00	-1.76	0.62	232.14	52.04	4.46	11.08	50.86	2.19
12	422.00	27.00	3.52	0.79	801.08	62.96	12.72	39.00	153.32	2.15
13	534.00	25.80	2.08	0.71	543.03	50.90	10.67	25.19	103.61	2.28
14	630.00	11.40	8.32	0.64	492.31	53.44	9.21	16.82	76.60	2.35
15	486.00	29.40	0.16	0.92	684.66	144.10	4.75	35.90	140.59	2.24
16	678.00	10.20	6.88	0.72	663.94	82.22	8.08	25.45	112.39	2.40
17	662.00	9.00	3.04	0.93	1014.51	258.66	3.92	44.87	201.50	2.38
18	598.00	16.20	8.80	0.65	548.03	57.24	9.57	20.03	89.87	2.32
19	406.00	1.80	2.56	0.68	534.87	40.56	13.19	25.24	109.70	2.07
20	374.00	19.80	9.28	0.69	617.00	52.96	11.65	28.68	112.05	2.06
21	518.00	17.40	5.44	0.86	972.62	125.07	7.78	38.46	176.05	2.23
22	694.00	24.60	-0.80	0.61	245.17	52.19	4.70	12.86	47.85	2.48
23	742.00	13.80	7.36	0.80	881.51	131.78	6.69	35.75	144.67	2.48
24	454.00	4.20	-0.32	0.83	612.93	114.25	5.36	30.22	134.79	2.13
25	646.00	0.60	4.00	0.82	876.34	125.44	6.99	34.79	160.06	2.35

Table B.4. OSF designs for the MDO of the joined-wing

Design Point #	Input Design Variables				Output Design Variables					
	Joint Location (mm)	Aft Wing Sweep (degree)	AOA (degree)	Mach Number	Total Lift (N)	Total Drag (N)	L/D	Tip Deflection (mm)	Equivalent Stress (MPa)	Mass (Kg)
1	550.00	27.00	-1.28	0.75	387.76	79.56	4.87	19.08	78.81	2.31
2	726.00	25.80	3.04	0.79	776.87	94.67	8.21	37.94	142.03	2.52
3	534.00	4.20	8.32	0.69	624.94	65.56	9.53	22.84	108.03	2.22
4	566.00	29.40	5.44	0.71	616.45	49.33	12.50	26.10	101.78	2.35
5	406.00	12.60	2.08	0.92	851.45	163.67	5.20	43.29	183.21	2.09
6	582.00	15.00	-1.76	0.89	450.75	172.60	2.61	21.98	97.83	2.30
7	646.00	24.60	9.28	0.85	1014.09	140.77	7.20	39.61	158.40	2.42
8	710.00	7.80	4.96	0.66	533.83	58.19	9.17	21.85	93.82	2.43
9	742.00	10.20	1.60	0.86	826.04	177.71	4.65	39.22	161.54	2.47
10	486.00	17.40	9.76	0.77	833.86	91.76	9.09	31.48	142.48	2.19
11	422.00	13.80	0.16	0.62	323.09	40.05	8.07	16.39	69.14	2.11
12	630.00	22.20	3.52	0.94	1059.60	225.09	4.71	48.52	201.49	2.38
13	614.00	6.60	-0.32	0.72	435.72	85.18	5.12	19.87	91.28	2.32
14	694.00	9.00	8.80	0.83	1000.56	152.21	6.57	37.68	167.41	2.41
15	470.00	28.20	4.48	0.90	1016.79	134.77	7.54	47.65	190.22	2.21
16	358.00	23.40	6.40	0.73	685.71	48.98	14.00	34.14	126.32	2.05
17	662.00	18.60	0.64	0.64	358.68	55.42	6.47	16.83	69.80	2.41
18	678.00	19.80	7.84	0.65	526.98	58.54	9.00	20.82	83.99	2.43
19	438.00	1.80	2.56	0.68	537.61	42.95	12.52	24.18	109.46	2.11
20	390.00	21.00	1.12	0.76	608.47	61.41	9.91	32.79	127.96	2.09
21	374.00	5.40	6.88	0.80	860.92	86.21	9.99	39.54	162.21	2.04
22	502.00	16.20	5.92	0.61	451.76	31.24	14.46	18.33	83.31	2.21
23	518.00	11.40	7.36	0.93	1318.84	207.81	6.35	54.38	254.56	2.21
24	454.00	3.00	-0.80	0.82	549.93	110.41	4.98	27.25	120.98	2.13
25	598.00	0.60	4.00	0.87	989.92	165.69	5.97	40.94	191.88	2.29

Table B.5. Space grid designs for the joined-wing

Design Point #	Input Design Variables				Output Design Variables					
	Joint Location (mm)	Aft Wing Sweep (degree)	AOA (degree)	Mach Number	Total Lift (N)	Total Drag (N)	L/D	Tip Deflection (mm)	Equivalent Stress (MPa)	Mass (Kg)
1	550.00	15.00	4.00	0.77	765.94	79.66	9.62	29.83	137.60	2.26
2	350.00	15.00	4.00	0.77	761.96	55.49	13.73	38.49	151.58	2.02
3	750.00	15.00	4.00	0.77	777.63	104.84	7.42	33.56	132.10	2.50
4	550.00	0.00	4.00	0.77	770.69	87.60	8.80	29.51	141.48	2.24
5	550.00	30.00	4.00	0.77	746.36	67.24	11.10	32.01	125.41	2.33
6	550.00	15.00	-2.00	0.77	363.06	99.76	3.64	17.49	79.03	2.26
7	550.00	15.00	10.00	0.77	838.42	101.62	8.25	30.53	141.50	2.26
8	550.00	15.00	4.00	0.60	423.09	31.17	13.57	17.51	80.22	2.26
9	550.00	15.00	4.00	0.95	1121.10	243.16	4.61	49.69	226.68	2.26

Table B.6. Verification points for MDO RS accuracy assessments

Design Point #	Input Design Variables				Output Design Variables					
	Joint Location (mm)	Aft Wing Sweep (degree)	AOA (degree)	Mach Number	Total Lift (N)	Total Drag (N)	L/D	Tip Deflection (mm)	Equivalent Stress (MPa)	Mass (Kg)
1	538.24	0.32	9.84	0.94	1541.82	240.92	6.40	61.53	292.67	2.23
2	543.83	29.28	9.77	0.60	471.70	42.16	11.19	18.23	72.93	2.32
3	744.05	16.57	-1.87	0.62	203.04	62.40	3.25	10.62	41.71	2.50
4	544.55	28.79	-1.48	0.62	219.30	45.56	4.81	11.06	43.80	2.32
5	531.34	29.68	-1.46	0.94	451.15	167.58	2.69	24.27	95.05	2.30
6	370.10	12.70	-1.59	0.93	426.16	169.32	2.52	24.56	94.31	2.04
7	504.80	1.12	-1.25	0.93	469.11	237.50	1.98	21.51	98.98	2.19
8	739.98	13.36	-1.98	0.95	376.99	301.64	1.25	21.56	86.85	2.48
9	513.53	29.25	9.44	0.93	1408.28	168.45	8.36	59.20	240.13	2.28
10	358.61	13.79	9.38	0.94	1467.73	172.19	8.52	74.97	298.96	2.03
11	571.68	29.33	4.04	0.79	800.81	77.40	10.35	34.17	134.70	2.36
12	370.62	15.28	9.90	0.61	477.05	37.09	12.86	21.77	86.79	2.05
13	529.19	14.50	-1.90	0.77	372.47	96.76	3.85	18.15	81.73	2.24
14	365.79	13.52	-1.31	0.62	244.91	39.73	6.16	13.94	54.09	2.04
15	636.11	9.80	1.18	0.87	841.77	145.38	5.79	38.41	173.05	2.35
16	648.93	21.50	0.75	0.72	488.76	75.19	6.50	23.09	93.95	2.40
17	563.83	0.59	-1.12	0.62	262.90	55.13	4.77	12.15	55.96	2.26
18	528.45	16.81	9.06	0.77	798.51	91.93	8.69	29.45	134.42	2.24
19	745.08	17.20	4.11	0.79	822.26	112.08	7.34	35.87	140.34	2.50
20	580.01	14.28	4.13	0.60	428.65	33.58	12.77	17.48	79.55	2.29

APPENDIX C

ACCURACY ASSESSMENTS OF DIFFERENT DOE AND META-MODELLING TYPES

In this part goodness of fit results of standard RS generated on different DOE types without refinement points are given through Table C1-C8.

For all meta-modelling types, FCCCD is used without refinement. As expected, the accuracy of RS created by non-parametric regression and kriging is perfectly good since in these meta-models it is assured that RS certainly passes through design points. Therefore, the accuracy assessments for these meta-modelling algorithms are performed through verification points. The accuracy assessments of different meta-modelling types are given Tables C9-C12.

Table C.1. Accuracy of RS fitted to FCCCD data

	Total Lift	Total Drag	Mass	Tip Deflection	Equivalent Stress
Coefficient of Determination (Best Value = 1)	0.9980	0.9887	1.0000	0.9926	0.9911
Adjusted Coeff of Determination (Best Value = 1)	0.9975	0.9841	1.0000	0.9896	0.9893
Maximum Relative Residual (Best Value = 0%)	12.7954	48.0100	0.0581	29.1751	26.0893
Root Mean Square Error (Best Value = 0)	20.6274	9.3319	0.0003	1.9477	7.9535
Relative Root Mean Square Error (Best Value = 0%)	4.9405	13.7296	0.0145	10.7305	9.2735
Relative Maximum Absolute Error (Best Value = 0%)	11.3205	19.0635	0.6736	19.6770	21.9088
Relative Average Absolute Error (Best Value = 0%)	3.5079	8.7124	0.0919	6.2630	6.9707

Table C.2. Accuracy of RS fitted to FCCCD data for verification points

	Total Lift	Total Drag	Mass	Tip Deflection	Equivalent Stress
Maximum Relative Residual (Best Value = 0%)	9.8668	42.5549	0.7247	27.0757	30.0755
Root Mean Square Error (Best Value = 0)	37.5901	13.1299	0.0079	3.9650	18.3231
Relative Root Mean Square Error (Best Value = 0%)	4.8482	13.9934	0.3654	12.7255	12.8388
Relative Maximum Absolute Error (Best Value = 0%)	25.1814	45.1847	7.9940	49.5000	64.2288
Relative Average Absolute Error (Best Value = 0%)	5.5576	11.3683	3.5821	13.4297	14.9836

Table C.3. Accuracy of RS fitted to BBD data

	Total Lift	Total Drag	Mass	Tip Deflection	Equivalent Stress
Coefficient of Determination (Best Value = 1)	0.9953	0.9978	1.0000	0.9890	0.9819
Adjusted Coeff of Determination (Best Value = 1)	0.9941	0.9967	1.0000	0.9845	0.9771
Maximum Relative Residual (Best Value = 0%)	10.8619	13.3534	0.0595	17.9877	14.0785
Root Mean Square Error (Best Value = 0)	23.1059	3.6838	0.0004	1.6103	8.6798
Relative Root Mean Square Error (Best Value = 0%)	4.1907	5.3457	0.0175	7.6133	7.2063
Relative Maximum Absolute Error (Best Value = 0%)	14.8454	11.2218	0.8511	20.2367	29.9600
Relative Average Absolute Error (Best Value = 0%)	5.1811	3.4715	0.1699	8.5754	10.9144

Table C.4. Accuracy of RS fitted to BBD data for verification points

	Total Lift	Total Drag	Mass	Tip Deflection	Equivalent Stress
Maximum Relative Residual (Best Value = 0%)	13.8467	16.5402	0.6440	29.9500	21.6691
Root Mean Square Error (Best Value = 0)	37.0312	13.3646	0.0071	3.5703	13.4695
Relative Root Mean Square Error (Best Value = 0%)	6.3456	9.8834	0.3254	14.9669	10.4259
Relative Maximum Absolute Error (Best Value = 0%)	28.9832	38.4485	8.2741	54.4359	63.4363
Relative Average Absolute Error (Best Value = 0%)	7.2808	12.5991	3.6927	18.2479	12.6856

Table C.5. Accuracy of RS fitted to LHS data

	Total Lift	Total Drag	Mass	Tip Deflection	Equivalent Stress
Coefficient of Determination (Best Value = 1)	0.9719	0.9974	1.0000	0.9843	0.9819
Adjusted Coeff of Determination (Best Value = 1)	0.9663	0.9956	1.0000	0.9730	0.9729
Maximum Relative Residual (Best Value = 0%)	12.2209	5.5710	0.0581	10.4100	11.0105
Root Mean Square Error (Best Value = 0)	44.1634	2.8371	0.0005	1.4644	6.9792
Relative Root Mean Square Error (Best Value = 0%)	5.7220	2.6003	0.0227	4.2641	5.2132
Relative Maximum Absolute Error (Best Value = 0%)	45.6002	14.0707	0.9603	33.6124	29.9367
Relative Average Absolute Error (Best Value = 0%)	12.7931	3.7165	0.2690	8.7710	10.2046

Table C.6. Accuracy of RS fitted to LHS data for verification points

	Total Lift	Total Drag	Mass	Tip Deflection	Equivalent Stress
Maximum Relative Residual (Best Value = 0%)	126.1133	59.3429	1.8049	117.4972	104.4439
Root Mean Square Error (Best Value = 0)	199.5847	40.1363	0.0167	12.1983	40.7619
Relative Root Mean Square Error (Best Value = 0%)	49.6315	22.2490	0.7609	53.3190	43.2604
Relative Maximum Absolute Error (Best Value = 0%)	140.1659	209.7091	26.0718	196.1943	154.1438
Relative Average Absolute Error (Best Value = 0%)	42.0244	31.9476	9.3380	63.8538	45.2336

Table C.7. Accuracy of RS fitted to OSF data

	Total Lift	Total Drag	Mass	Tip Deflection	Equivalent Stress
Coefficient of Determination (Best Value = 1)	0.9858	0.9981	1.0000	0.9865	0.9789
Adjusted Coeff of Determination (Best Value = 1)	0.9829	0.9974	1.0000	0.9820	0.9702
Maximum Relative Residual (Best Value = 0%)	8.1514	7.9825	0.0740	9.1827	10.7104
Root Mean Square Error (Best Value = 0)	30.6450	2.4090	0.0007	1.2645	6.8198
Relative Root Mean Square Error (Best Value = 0%)	4.2975	3.3382	0.0327	4.2379	5.0916
Relative Maximum Absolute Error (Best Value = 0%)	24.5685	11.9226	1.1903	25.1626	36.5635
Relative Average Absolute Error (Best Value = 0%)	9.8579	3.2148	0.4032	9.5689	11.1843

Table C.8. Accuracy of RS fitted to OSF data for verification points

	Total Lift	Total Drag	Mass	Tip Deflection	Equivalent Stress
Maximum Relative Residual (Best Value = 0%)	34.8586	54.8277	0.1222	35.3562	34.2359
Root Mean Square Error (Best Value = 0)	85.6788	16.2506	0.0012	6.1445	27.5126
Relative Root Mean Square Error (Best Value = 0%)	15.6642	20.0150	0.0514	18.8900	17.2291
Relative Maximum Absolute Error (Best Value = 0%)	54.1153	46.2357	2.1307	128.2414	116.4585
Relative Average Absolute Error (Best Value = 0%)	19.6967	18.9700	0.6298	30.3509	29.7055

Table C.9. Accuracy of RS created by neural network

	Total Lift	Total Drag	Mass	Tip Deflection	Equivalent Stress
Coefficient of Determination (Best Value = 1)	0.6200	0.9419	0.9927	0.6041	0.6114
Adjusted Coeff of Determination (Best Value = 1)	199.1717	37.2823	1.8251	189.2941	235.2179
Maximum Relative Residual (Best Value = 0%)	283.5111	21.1942	0.0181	14.2506	52.5902
Root Mean Square Error (Best Value = 0)	71.4556	16.1034	0.7477	51.9740	63.8159
Relative Root Mean Square Error (Best Value = 0%)	143.2326	58.5585	20.0540	146.3646	177.1339
Relative Maximum Absolute Error (Best Value = 0%)	39.2802	17.5933	5.9483	40.0608	31.5990
Relative Average Absolute Error (Best Value = 0%)	0.6200	0.9419	0.9927	0.6041	0.6114

Table C.10. Accuracy of RS created by neural network for verification points

	Total Lift	Total Drag	Mass	Tip Deflection	Equivalent Stress
Maximum Relative Residual (Best Value = 0%)	162.5984	33.3123	2.1694	95.0902	115.3989
Root Mean Square Error (Best Value = 0)	258.3021	17.7633	0.0225	10.8366	45.4519
Relative Root Mean Square Error (Best Value = 0%)	58.5672	14.5372	0.9729	42.5305	46.3396
Relative Maximum Absolute Error (Best Value = 0%)	138.8897	50.9260	25.5537	102.3721	132.7827
Relative Average Absolute Error (Best Value = 0%)	38.2577	15.1266	9.1926	36.5244	34.3917

Table C.11. Accuracy of RS created by non-parametric regression for verification points

	Total Lift	Total Drag	Mass	Tip Deflection	Equivalent Stress
Maximum Relative Residual (Best Value = 0%)	18.3940	56.5465	2.6467	34.1411	24.0738
Root Mean Square Error (Best Value = 0)	53.5712	20.9430	0.0224	5.7140	13.1336
Relative Root Mean Square Error (Best Value = 0%)	7.6802	18.9585	0.9582	12.5412	9.0449
Relative Maximum Absolute Error (Best Value = 0%)	33.3687	97.8883	34.2589	97.2708	49.7925
Relative Average Absolute Error (Best Value = 0%)	8.2146	13.7055	9.3463	15.5161	9.4491

Table C.12. Accuracy of RS created by kriging for verification points

	Total Lift	Total Drag	Mass	Tip Deflection	Equivalent Stress
Maximum Relative Residual (Best Value = 0%)	18.0648	26.1757	0.3751	35.5896	20.9209
Root Mean Square Error (Best Value = 0)	41.4455	11.2304	0.0043	4.6687	11.8596
Relative Root Mean Square Error (Best Value = 0%)	5.5180	10.8791	0.1951	15.6711	8.1069
Relative Maximum Absolute Error (Best Value = 0%)	34.4551	45.3130	4.8012	70.0701	44.6784
Relative Average Absolute Error (Best Value = 0%)	5.6402	8.5641	1.5355	15.0785	9.1994

APPENDIX D

REFINEMENT POINTS

Table D.1. Refinement design points for FCCCD

Design Point #	Input Design Variables				Output Design Variables					
	Joint Location (mm)	Aft Wing Sweep (degree)	AOA (degree)	Mach Number	Total Lift (N)	Total Drag (N)	L/D	Tip Deflection (mm)	Equivalent Stress (MPa)	Mass (Kg)
1	350.00	0.00	10.00	0.84	987.66	107.76	9.17	44.63	179.78	2.01
2	509.38	0.00	-2.00	0.95	371.28	255.89	1.45	16.91	79.30	2.19
3	350.00	0.00	1.58	0.95	872.95	202.28	4.32	47.67	186.91	2.01
4	750.00	30.00	-2.00	0.78	350.24	103.94	3.37	19.93	72.29	2.59
5	350.00	30.00	-2.00	0.69	261.88	47.64	5.50	16.63	55.04	2.07
6	750.00	30.00	10.00	0.85	1075.15	149.49	7.19	47.78	190.90	2.59
7	750.00	0.00	3.94	0.68	575.57	69.16	8.32	24.78	105.07	2.47
8	750.00	0.00	-2.00	0.86	436.73	197.98	2.21	22.78	95.42	2.47
9	350.00	30.00	-2.00	0.84	433.94	85.91	5.05	28.12	92.75	2.07
10	522.60	30.00	10.00	0.69	630.08	61.92	10.18	24.91	99.41	2.30
11	350.00	0.00	4.14	0.67	550.32	33.35	16.50	26.84	108.34	2.01
12	750.00	30.00	4.00	0.60	429.50	34.49	12.45	21.73	83.54	2.59
13	350.00	30.00	4.60	0.89	1008.32	107.34	9.39	56.28	194.34	2.07
14	750.00	0.00	4.03	0.95	1182.22	332.64	3.55	54.63	235.02	2.47
15	565.26	0.00	-2.00	0.68	291.44	73.66	3.96	13.74	63.48	2.26
16	350.00	0.00	-2.00	0.79	422.67	85.49	4.94	23.44	92.58	2.01
17	750.00	30.00	3.11	0.89	925.54	155.88	5.94	49.83	186.12	2.59
18	350.00	30.00	4.00	0.60	417.58	17.04	24.51	23.66	80.63	2.07
19	750.00	0.00	10.00	0.76	839.25	122.45	6.85	31.24	136.08	2.47
20	350.00	0.00	7.63	0.60	417.99	28.87	14.48	19.26	77.03	2.01
21	750.00	30.00	7.59	0.95	1446.91	231.78	6.24	74.50	275.16	2.59
22	350.00	13.67	10.00	0.69	630.94	54.89	11.49	29.72	115.81	2.02
23	750.00	18.38	8.89	0.69	620.33	81.93	7.57	24.63	96.92	2.51
24	590.32	0.00	0.90	0.60	340.95	45.10	7.56	15.05	69.60	2.29
25	350.00	0.00	6.92	0.95	1416.12	199.09	7.11	76.04	296.96	2.01
26	750.00	30.00	6.91	0.6	445.42	38.51	11.57	20.89	82.88	2.59
27	542.70	17.30	1.26	0.80	663.17	89.14	7.44	30.21	134.12	2.26
28	550.00	30.00	10.00	0.95	1567.26	193.35	8.11	69.69	275.58	2.33
29	550.28	0.00	10.00	0.60	474.77	49.59	9.57	16.18	77.14	2.24
30	750.00	0.00	0.64	0.95	776.08	335.24	2.32	37.47	159.90	2.47
31	750.00	14.39	-0.61	0.65	306.92	71.00	4.32	15.04	59.57	2.49
32	350.00	30.00	0.23	0.60	292.89	29.50	9.93	18.04	60.16	2.07
33	511.83	0.00	10.00	0.89	1217.70	175.63	6.93	43.44	210.62	2.20
34	350.00	30.00	10.00	0.81	897.87	82.11	10.94	45.17	155.93	2.07
35	620.49	30.00	-2.00	0.60	188.86	46.43	4.07	9.78	37.09	2.42
36	654.16	0.00	10.00	0.60	474.95	55.55	8.55	16.32	75.25	2.36
37	632.78	0.00	-2.00	0.95	386.15	299.33	1.29	19.48	87.79	2.33
38	519.68	30.00	-2.00	0.88	451.19	124.12	3.63	24.11	94.01	2.29
39	472.80	0.00	-2.00	0.60	216.49	47.17	4.59	10.29	47.24	2.15
40	652.69	0.00	10.00	0.91	1355.66	230.39	5.88	49.53	233.22	2.36
41	350.00	0.00	2.91	0.86	927.55	107.63	8.62	47.30	191.78	2.01
42	750.00	0.00	6.46	0.85	997.13	169.62	5.88	40.47	174.57	2.47
43	350.00	30.00	4.46	0.69	579.80	30.41	19.06	31.86	109.18	2.07
44	750.00	30.00	0.10	0.72	444.72	78.81	5.64	24.35	90.41	2.59
45	706.26	0.00	10.00	0.65	568.05	72.89	7.79	20.08	89.74	2.42
46	350.00	0.00	0.53	0.73	540.78	57.30	9.44	28.69	114.19	2.01
47	350.00	30.00	10.00	0.74	714.09	61.36	11.64	36.19	124.15	2.07

Table D.2. Refinement design points for BBD

Design Point #	Input Design Variables				Output Design Variables					
	Joint Location (mm)	Aft Wing Sweep (degree)	AOA (degree)	Mach Number	Total Lift (N)	Total Drag (N)	L/D	Tip Deflection (mm)	Equivalent Stress (MPa)	Mass (Kg)
1	350.00	30.00	10.00	0.65	545.45	42.32	12.89	27.42	94.42	2.07
2	750.00	0.00	-0.07	0.95	675.12	333.52	2.02	33.20	141.09	2.47
3	750.00	30.00	7.13	0.60	444.14	39.86	11.14	20.76	82.22	2.59
4	350.00	30.00	-2.00	0.66	239.59	43.18	5.55	15.20	50.42	2.07
5	750.00	30.00	8.08	0.95	1485.38	229.92	6.46	75.88	280.18	2.59
6	493.71	15.14	4.12	0.84	912.08	109.18	8.35	38.72	176.57	2.19
7	350.00	0.00	10.00	0.89	1199.90	135.39	8.86	54.45	221.33	2.01
8	350.00	30.00	-2.00	0.90	440.29	109.59	4.02	29.11	95.66	2.07
9	750.00	0.00	0.48	0.60	274.83	58.15	4.73	12.97	55.14	2.47
10	536.60	6.89	4.78	0.72	643.17	61.94	10.38	24.99	118.58	2.23
11	750.00	0.00	10.00	0.71	696.71	96.97	7.18	25.69	111.37	2.47
12	350.00	0.00	-2.00	0.84	459.89	105.01	4.38	26.42	102.61	2.01
13	750.00	30.00	-2.00	0.71	276.60	81.50	3.39	15.76	57.56	2.59
14	750.00	30.00	10.00	0.84	1023.45	140.91	7.26	45.48	182.13	2.59
15	350.00	0.00	1.98	0.66	484.64	35.22	13.76	25.21	100.55	2.01
16	750.00	30.00	1.08	0.81	711.71	108.48	6.56	39.05	144.67	2.59
17	750.00	30.00	5.28	0.89	1052.88	166.16	6.34	53.81	204.68	2.59
18	350.00	2.58	7.00	0.65	541.38	36.73	14.74	26.22	103.05	2.01
19	350.00	24.12	1.70	0.91	845.12	129.56	6.52	49.34	178.64	2.05
20	639.06	7.62	7.10	0.81	887.67	124.17	7.15	32.76	150.88	2.35
21	750.00	5.47	1.06	0.74	555.92	101.55	5.47	26.02	108.88	2.47
22	750.00	0.00	0.24	0.87	723.24	210.24	3.44	35.05	148.24	2.47
23	350.00	30.00	8.33	0.73	688.27	53.41	12.89	35.77	122.11	2.07
24	750.00	30.00	4.52	0.67	547.26	48.87	11.20	27.08	105.13	2.59
25	350.00	30.00	7.19	0.91	1198.15	123.91	9.67	64.51	225.11	2.07
26	350.00	30.00	7.27	0.86	974.47	92.50	10.53	50.64	175.47	2.07
27	350.00	23.00	0.89	0.70	474.11	44.99	10.54	27.81	100.26	2.04
28	750.00	0.00	-2.00	0.64	241.88	75.39	3.21	12.06	51.45	2.47
29	750.00	23.46	7.30	0.69	603.30	73.01	8.26	26.27	101.60	2.54
30	750.00	0.00	6.74	0.76	786.78	109.54	7.18	30.99	132.99	2.47
31	350.00	0.00	2.89	0.88	941.71	118.11	7.97	47.88	194.41	2.01
32	750.00	0.00	10.00	0.63	535.79	70.58	7.59	19.25	82.79	2.47
33	350.00	30.00	-2.00	0.74	315.02	57.70	5.46	20.00	66.43	2.07
34	350.00	23.66	10.00	0.81	932.85	90.27	10.33	44.62	165.75	2.05
35	350.00	20.94	0.97	0.78	633.33	61.41	10.31	37.17	134.94	2.04
36	750.00	30.00	2.11	0.63	415.24	46.21	8.99	22.00	83.03	2.59
37	750.00	24.94	10.00	0.91	1363.12	206.60	6.60	59.42	228.96	2.55
38	750.00	0.00	-2.00	0.92	426.06	292.35	1.46	22.95	95.74	2.47
39	750.00	0.00	-2.00	0.81	405.57	160.33	2.53	20.98	88.43	2.47
40	750.00	0.00	-0.40	0.68	383.87	87.64	4.38	18.18	77.45	2.47

Table continues in the next page

Design Point #	Input Design Variables				Output Design Variables					
	Joint Location (mm)	Aft Wing Sweep (degree)	AOA (degree)	Mach Number	Total Lift (N)	Total Drag (N)	L/D	Tip Deflection (mm)	Equivalent Stress (MPa)	Mass (Kg)
41	750.00	30.00	10.00	0.74	726.31	94.33	7.70	31.86	129.17	2.59
42	350.00	30.00	5.76	0.63	485.14	21.62	22.44	26.17	90.04	2.07
43	350.00	30.00	3.26	0.74	665.68	37.42	17.79	37.19	128.54	2.07
44	750.00	0.00	8.11	0.87	1140.26	195.70	5.83	45.80	199.03	2.47
45	350.00	30.00	-0.36	0.62	290.46	34.30	8.47	17.99	60.07	2.07
46	750.00	30.00	0.15	0.84	669.53	132.32	5.06	37.66	137.46	2.59
47	350.00	0.00	-2.00	0.70	309.32	57.83	5.35	16.71	66.23	2.01
48	350.00	0.00	3.14	0.81	868.92	74.00	11.74	43.00	175.79	2.01
49	350.00	0.00	10.00	0.62	502.44	42.01	11.96	22.52	90.31	2.01
50	750.00	0.00	5.18	0.92	1200.48	276.37	4.34	53.46	230.06	2.47
51	350.00	30.00	4.78	0.69	580.06	29.93	19.38	31.63	108.86	2.07
52	350.00	30.00	-1.60	0.81	446.31	75.99	5.87	28.33	94.29	2.07
53	350.00	0.00	-2.00	0.60	216.69	39.46	5.49	11.74	46.49	2.01
54	750.00	30.00	-2.00	0.87	450.77	149.70	3.01	26.35	94.45	2.59
55	750.00	30.00	10.00	0.68	596.08	72.76	8.19	25.92	106.22	2.59
56	750.00	30.00	6.53	0.83	906.92	124.33	7.29	42.57	168.84	2.59
57	750.00	0.00	2.95	0.69	548.91	73.67	7.45	24.79	105.22	2.47
58	750.00	30.00	-2.00	0.95	342.35	209.73	1.63	23.68	79.23	2.59
59	750.00	0.00	8.52	0.95	1535.23	312.47	4.91	64.52	282.40	2.47

Table D.3. Refinement design points for LHS

Design Point #	Input Design Variables				Output Design Variables					
	Joint Location (mm)	Aft Wing Sweep (degree)	AOA (degree)	Mach Number	Total Lift (N)	Total Drag (N)	L/D	Tip Deflection (mm)	Equivalent Stress (MPa)	Mass (Kg)
1	350.00	30.00	-2.00	0.60	187.38	33.86	5.53	11.97	39.58	2.07
2	350.00	0.00	10.00	0.60	468.16	37.33	12.54	21.12	84.39	2.01
3	750.00	30.00	10.00	0.60	458.31	52.14	8.79	19.71	81.44	2.59
4	750.00	0.00	-2.00	0.95	397.60	333.53	1.19	21.93	91.73	2.47
5	750.00	30.00	10.00	0.95	1605.35	228.10	7.04	78.74	292.62	2.59
6	750.00	30.00	-2.00	0.80	373.39	112.55	3.32	21.27	77.04	2.59
7	350.00	30.00	8.23	0.95	1471.09	161.10	9.13	86.90	280.88	2.07
8	750.00	0.00	1.65	0.60	373.70	52.79	7.08	17.03	72.17	2.47
9	350.00	0.00	6.18	0.95	1341.12	196.52	6.82	71.23	280.31	2.01
10	350.00	20.51	-2.00	0.95	352.82	162.56	2.17	21.35	76.49	2.04
11	750.00	0.00	10.00	0.77	882.67	129.79	6.80	33.35	145.45	2.47
12	350.00	0.00	8.60	0.95	1515.73	192.80	7.86	79.41	299.04	2.01
13	350.00	16.14	4.58	0.95	1176.95	181.81	6.47	67.37	252.41	2.03
14	529.92	30.00	7.51	0.78	785.59	80.31	9.78	31.87	126.48	2.30
15	750.00	30.00	3.18	0.95	1059.49	232.80	4.55	59.46	213.89	2.59
16	350.00	30.00	5.68	0.60	441.42	17.85	24.73	23.98	82.43	2.07
17	350.00	0.00	-2.00	0.80	432.77	89.05	4.86	24.26	95.39	2.01
18	350.00	17.49	0.00	0.60	289.30	32.60	8.88	16.89	62.29	2.03
19	510.20	0.00	5.24	0.60	446.13	32.10	13.90	17.53	83.37	2.19
20	750.00	0.00	8.22	0.95	1511.48	311.62	4.85	63.72	278.63	2.47
21	350.00	0.00	10.00	0.78	833.77	86.92	9.59	37.32	150.24	2.01
22	750.00	0.00	-2.00	0.75	345.69	120.68	2.86	17.52	74.52	2.47
23	350.00	0.00	-2.00	0.60	216.69	39.46	5.49	11.74	46.49	2.01
24	750.00	30.00	-2.00	0.95	342.35	209.73	1.63	23.68	79.23	2.59
25	350.00	0.00	-2.00	0.95	337.55	197.76	1.71	15.59	64.84	2.01
26	350.00	30.00	-2.00	0.78	363.91	68.66	5.30	23.18	76.98	2.07
27	750.00	0.00	10.00	0.60	469.57	58.77	7.99	16.90	72.25	2.47
28	350.00	20.32	10.00	0.84	1019.29	104.50	9.75	48.80	185.45	2.04
29	750.00	30.00	10.00	0.75	758.12	98.53	7.69	33.43	135.25	2.59
30	750.00	19.22	4.62	0.60	432.26	41.31	10.46	19.70	74.46	2.51
31	750.00	13.48	-2.00	0.67	240.40	78.44	3.06	12.42	50.90	2.49
32	350.00	30.00	10.00	0.60	458.15	32.10	14.27	22.96	79.00	2.07
33	350.00	15.86	-2.00	0.71	303.13	57.41	5.28	18.07	67.45	2.03
34	750.00	14.95	10.00	0.95	1629.48	295.14	5.52	69.08	283.46	2.50
35	573.97	12.69	-2.00	0.95	357.25	260.16	1.37	17.88	80.83	2.28
36	570.82	0.00	10.00	0.86	1137.83	164.08	6.93	39.71	191.68	2.26
37	750.00	30.00	10.00	0.85	1060.73	147.19	7.21	47.14	188.44	2.59
38	350.00	0.00	4.07	0.78	784.88	61.98	12.66	37.11	152.10	2.01
39	750.00	0.00	3.67	0.69	587.53	72.05	8.15	25.69	108.83	2.47
40	750.00	30.00	3.52	0.60	414.23	34.69	11.94	21.30	81.18	2.59

Table continues in the next page

Design Point #	Input Design Variables				Output Design Variables					
	Joint Location (mm)	Aft Wing Sweep (degree)	AOA (degree)	Mach Number	Total Lift (N)	Total Drag (N)	L/D	Tip Deflection (mm)	Equivalent Stress (MPa)	Mass (Kg)
41	750.00	30.00	1.42	0.77	642.73	88.41	7.27	34.83	129.79	2.59
42	750.00	0.00	-2.00	0.85	423.75	189.63	2.23	22.26	93.33	2.47
43	350.00	30.00	10.00	0.90	1212.47	120.79	10.04	61.07	214.05	2.07
44	530.73	0.00	10.00	0.69	647.72	73.31	8.84	22.61	108.16	2.22
45	750.00	30.00	5.07	0.66	531.67	46.48	11.44	25.86	100.95	2.59
46	350.00	30.00	-2.00	0.87	451.11	97.59	4.62	29.67	97.67	2.07
47	750.00	30.00	1.18	0.65	404.08	54.83	7.37	21.75	81.57	2.59
48	350.00	30.00	10.00	0.73	706.44	60.91	11.60	35.67	122.91	2.07
49	350.00	30.00	-2.00	0.66	237.18	42.69	5.56	15.06	49.93	2.07

Table D.4. Refinement design points for OSF

Design Point #	Input Design Variables				Output Design Variables					
	Joint Location (mm)	Aft Wing Sweep (degree)	AOA (degree)	Mach Number	Total Lift (N)	Total Drag (N)	L/D	Tip Deflection (mm)	Equivalent Stress (MPa)	Mass (Kg)
1	750.00	30.00	-2.00	0.95	342.35	209.73	1.63	23.68	79.23	2.59
2	750.00	0.00	-2.00	0.60	213.98	64.76	3.30	10.66	45.57	2.47
3	750.00	0.00	10.00	0.60	469.57	58.77	7.99	16.90	72.25	2.47
4	750.00	0.00	10.00	0.95	1628.20	314.02	5.19	67.38	296.28	2.47
5	350.00	30.00	10.00	0.60	458.15	32.10	14.27	22.96	79.00	2.07
6	350.00	0.00	-2.00	0.60	216.69	39.46	5.49	11.74	46.49	2.01
7	750.00	30.00	-2.00	0.60	178.40	51.85	3.44	10.14	37.71	2.59
8	350.00	30.00	-2.00	0.95	375.88	135.79	2.77	24.80	81.57	2.07
9	350.00	0.00	-2.00	0.95	337.55	197.76	1.71	15.59	64.84	2.01
10	637.80	30.00	10.00	0.95	1621.90	234.58	6.91	77.09	288.76	2.44
11	350.00	0.00	10.00	0.91	1185.81	133.99	8.85	55.03	220.56	2.01
12	750.00	30.00	10.00	0.91	1315.68	185.85	7.08	59.96	237.03	2.59
13	350.00	30.00	-2.00	0.84	433.04	83.09	5.21	27.79	91.85	2.07
14	750.00	0.00	-2.00	0.77	364.00	133.72	2.72	18.58	78.60	2.47
15	750.00	30.00	10.00	0.72	685.38	86.99	7.88	29.99	122.28	2.59
16	350.00	30.00	10.00	0.67	573.16	45.23	12.67	28.98	99.21	2.07
17	350.00	0.00	-2.00	0.74	358.42	69.05	5.19	19.50	77.28	2.01
18	350.00	0.00	10.00	0.60	468.16	37.33	12.54	21.12	84.39	2.01
19	350.00	30.00	-2.00	0.68	251.88	45.54	5.53	15.98	52.92	2.07
20	750.00	0.00	-2.00	0.95	397.60	333.53	1.19	21.93	91.73	2.47
21	350.00	30.00	10.00	0.95	1558.67	154.02	10.12	89.37	288.11	2.07
22	750.00	0.00	10.00	0.74	786.50	113.10	6.95	29.12	126.64	2.47
23	750.00	30.00	-2.00	0.71	274.64	80.90	3.39	15.64	57.16	2.59
24	350.00	30.00	10.00	0.83	959.00	91.71	10.46	48.26	166.78	2.07
26	750.00	30.00	10.00	0.60	458.31	52.14	8.79	19.71	81.44	2.59
27	750.00	30.00	-2.00	0.84	427.04	133.62	3.20	24.48	88.45	2.59
28	350.00	30.00	3.15	0.60	401.45	18.32	21.92	23.59	79.49	2.07

Table D.5. Refinement design points for Sparse Grid

Design Point #	Input Design Variables				Output Design Variables					
	Joint Location (mm)	Aft Wing Sweep (degree)	AOA (degree)	Mach Number	Total Lift (N)	Total Drag (N)	L/D	Tip Deflection (mm)	Equivalent Stress (MPa)	Mass (Kg)
1	350.00	15.00	4.00	0.95	1115.92	186.98	5.97	63.07	240.18	2.02
2	750.00	15.00	4.00	0.95	1167.36	302.72	3.86	55.56	223.96	2.50
3	550.00	0.00	4.00	0.95	1155.65	265.57	4.35	51.13	239.11	2.24
4	550.00	30.00	4.00	0.95	1100.27	194.77	5.65	52.50	205.04	2.33
5	550.00	15.00	-2.00	0.95	355.21	244.71	1.45	17.81	79.75	2.26
6	550.00	15.00	10.00	0.95	1601.45	242.78	6.60	66.18	303.18	2.26
7	550.00	15.00	4.00	0.86	955.12	134.17	7.12	39.78	182.69	2.26
8	450.00	15.00	4.00	0.77	764.92	68.97	11.09	32.75	145.60	2.14
9	350.00	0.00	4.00	0.77	772.05	59.87	12.90	36.51	149.64	2.01
10	350.00	30.00	4.00	0.77	751.60	47.74	15.74	40.25	139.90	2.07
11	350.00	15.00	-2.00	0.77	370.25	74.36	4.98	22.07	82.93	2.02
12	350.00	15.00	10.00	0.77	811.67	78.35	10.36	38.49	150.02	2.02
13	350.00	15.00	4.00	0.60	419.43	19.99	20.99	22.35	86.23	2.02
14	650.00	15.00	4.00	0.77	768.34	92.11	8.34	31.41	135.80	2.38
15	750.00	0.00	4.00	0.77	786.78	114.55	6.87	32.15	137.28	2.47
16	750.00	30.00	4.00	0.77	771.55	84.02	9.18	37.65	149.13	2.59
17	750.00	15.00	-2.00	0.77	354.37	125.96	2.81	18.24	73.53	2.50
18	750.00	15.00	10.00	0.77	847.37	124.04	6.83	33.49	134.38	2.50
19	750.00	15.00	4.00	0.60	433.03	41.33	10.48	19.65	77.41	2.50
20	550.00	0.00	-2.00	0.77	389.01	106.55	3.65	18.76	87.02	2.24
21	550.00	30.00	-2.00	0.77	349.18	84.95	4.11	17.80	69.57	2.33
22	550.00	15.00	1.00	0.77	633.60	87.99	7.20	28.69	129.46	2.26
23	550.00	15.00	-2.00	0.60	194.40	48.58	4.00	9.31	41.84	2.26
24	550.00	0.00	4.00	0.60	426.75	33.40	12.78	17.30	82.02	2.24
25	550.00	30.00	4.00	0.60	417.46	26.67	15.65	18.98	73.76	2.33
26	550.00	15.00	10.00	0.60	470.58	46.86	10.04	16.76	77.09	2.26
27	550.00	15.00	4.00	0.69	575.99	49.57	11.62	23.38	106.87	2.26
28	550.00	0.00	10.00	0.77	851.20	107.92	7.89	29.76	143.47	2.24
29	550.00	30.00	10.00	0.77	808.85	91.00	8.89	32.26	127.11	2.33
30	550.00	15.00	7.00	0.77	785.95	89.32	8.80	29.36	135.28	2.26
31	550.00	22.50	4.00	0.77	745.41	75.78	9.84	30.37	131.21	2.29
32	550.00	7.50	4.00	0.77	771.26	85.44	9.03	29.87	142.74	2.25
33	350.00	15.00	-2.00	0.95	341.32	175.51	1.94	19.52	73.51	2.02
34	750.00	15.00	-2.00	0.95	356.85	299.13	1.19	21.44	84.98	2.50
35	550.00	0.00	-2.00	0.95	361.78	266.95	1.36	16.61	77.90	2.24
36	550.00	30.00	-2.00	0.95	359.02	179.04	2.01	20.51	79.51	2.33
37	550.00	15.00	1.00	0.95	800.99	244.57	3.28	37.43	168.90	2.26
38	550.00	15.00	-2.00	0.86	432.88	146.93	2.95	21.14	94.55	2.26
39	450.00	15.00	4.00	0.95	1128.48	214.16	5.27	54.33	235.22	2.14
40	350.00	0.00	4.00	0.95	1156.71	202.80	5.70	62.62	245.73	2.01

Table continues in the next page

Design Point #	Input Design Variables				Output Design Variables					
	Joint Location (mm)	Aft Wing Sweep (degree)	AOA (degree)	Mach Number	Total Lift (N)	Total Drag (N)	L/D	Tip Deflection (mm)	Equivalent Stress (MPa)	Mass (Kg)
41	350.00	30.00	4.00	0.95	1103.74	157.42	7.01	66.15	223.01	2.07
42	350.00	15.00	10.00	0.95	1530.58	176.94	8.65	80.66	301.38	2.02
43	350.00	15.00	4.00	0.86	942.63	98.68	9.55	49.35	193.53	2.02
44	450.00	15.00	-2.00	0.77	367.68	86.94	4.23	18.84	80.83	2.14
45	350.00	0.00	-2.00	0.77	399.26	79.55	5.02	22.12	87.32	2.01
46	350.00	30.00	-2.00	0.77	350.72	66.54	5.27	22.39	74.09	2.07
47	350.00	15.00	1.00	0.77	631.77	63.29	9.98	36.23	137.76	2.02
48	350.00	15.00	-2.00	0.60	194.35	36.78	5.28	11.57	43.28	2.02
49	450.00	15.00	-2.00	0.95	353.15	209.88	1.68	17.93	76.98	2.14
50	350.00	0.00	-2.00	0.95	337.55	197.76	1.71	15.59	64.84	2.01
51	350.00	30.00	-2.00	0.95	375.88	135.79	2.77	24.80	81.57	2.07
52	350.00	15.00	1.00	0.95	787.15	178.11	4.42	46.60	174.95	2.02
53	350.00	15.00	-2.00	0.86	439.68	107.66	4.08	27.38	100.77	2.02
54	750.00	15.00	10.00	0.95	1626.93	294.84	5.52	69.05	283.46	2.50
55	550.00	0.00	10.00	0.95	1599.57	254.08	6.30	65.49	304.35	2.24
56	550.00	30.00	10.00	0.95	1562.53	195.55	7.99	69.26	273.99	2.33
57	550.00	15.00	7.00	0.95	1422.96	247.19	5.76	61.52	279.96	2.26
58	550.00	15.00	10.00	0.86	1114.30	150.85	7.39	40.31	188.99	2.26
59	750.00	30.00	4.00	0.95	1131.95	229.29	4.94	61.85	225.65	2.59
60	550.00	22.50	4.00	0.95	1100.07	214.7796	5.12	49.71	214.11	2.29
61	550.00	30.00	4.00	0.86	914.37	112.11238	8.16	41.55	161.81	2.33
62	750.00	30.00	-2.00	0.77	348.03	103.83739	3.35	19.81	71.81	2.59
63	550.00	22.50	-2.00	0.77	349.42	94.355619	3.70	17.27	73.41	2.29
64	550.00	30.00	1.00	0.77	614.03	72.979128	8.41	29.98	116.15	2.33
65	550.00	30.00	-2.00	0.60	178.86	42.582975	4.20	9.24	35.43	2.33
66	750.00	30.00	-2.00	0.95	342.35	209.72526	1.63	23.68	79.23	2.59
67	550.00	22.50	-2.00	0.95	338.20	207.91048	1.63	18.65	77.68	2.29
68	550.00	30.00	1.00	0.95	771.15	187.64699	4.11	38.58	150.97	2.33
69	550.00	30.00	-2.00	0.86	446.23	120.57127	3.70	23.17	90.68	2.33
70	650.00	15.00	4.00	0.95	1125.84	275.15124	4.09	50.01	219.06	2.38
71	750.00	0.00	4.00	0.95	1177.08	331.04647	3.56	54.46	234.25	2.47
72	750.00	15.00	4.00	0.86	970.11	169.46629	5.72	44.23	175.82	2.50
73	650.00	15.00	-2.00	0.77	364.66	111.56583	3.27	17.78	77.54	2.38
74	750.00	0.00	-2.00	0.77	368.20	135.9653	2.71	19.02	80.53	2.47
75	750.00	15.00	1.00	0.77	636.89	113.87902	5.59	30.60	121.05	2.50
76	750.00	15.00	-2.00	0.60	194.30	59.602432	3.26	10.05	40.11	2.50
77	650.00	15.00	-2.00	0.95	374.02	267.0514	1.40	19.89	85.94	2.38
78	750.00	0.00	-2.00	0.95	397.60	333.52827	1.19	21.93	91.73	2.47
79	750.00	15.00	1.00	0.95	808.29	301.27796	2.68	41.07	164.61	2.50
80	750.00	15.00	-2.00	0.86	421.70	183.00195	2.30	22.34	88.57	2.50

Table continues in the next page

Design Point #	Input Design Variables				Output Design Variables					
	Joint Location (mm)	Aft Wing Sweep (degree)	AOA (degree)	Mach Number	Total Lift (N)	Total Drag (N)	L/D	Tip Deflection (mm)	Equivalent Stress (MPa)	Mass (Kg)
81	550.00	0.00	-2.00	0.60	207.81	51.34642	4.05	9.86	45.72	2.24
82	550.00	15.00	1.00	0.60	332.18	40.88389	8.13	14.95	67.42	2.26
83	550.00	15.00	-2.00	0.69	275.79	70.078383	3.94	13.14	59.39	2.26
84	450.00	15.00	10.00	0.77	841.45	89.281283	9.42	33.01	146.76	2.14
85	350.00	0.00	10.00	0.77	822.43	85.00819	9.67	36.85	148.29	2.01
86	350.00	30.00	10.00	0.77	801.53	71.483169	11.21	40.59	139.65	2.07
87	350.00	15.00	7.00	0.77	785.55	68.143893	11.53	38.35	148.76	2.02
88	350.00	15.00	10.00	0.60	466.17	34.990979	13.32	22.37	86.18	2.02
89	450.00	15.00	10.00	0.95	1605.70	210.53214	7.63	73.88	294.68	2.14
90	350.00	0.00	10.00	0.95	1586.00	189.08586	8.39	81.91	308.52	2.01
91	350.00	30.00	10.00	0.95	1558.67	154.02495	10.12	89.37	288.11	2.07
92	350.00	15.00	7.00	0.95	1395.01	187.77399	7.43	79.41	299.19	2.02
93	350.00	15.00	10.00	0.86	1083.38	116.57605	9.29	51.44	201.61	2.02
94	650.00	30.00	4.00	0.77	761.03	75.520026	10.08	34.16	130.10	2.46
95	750.00	22.50	4.00	0.77	768.77	96.000949	8.01	35.19	134.86	2.53
96	750.00	30.00	10.00	0.77	831.75	109.86478	7.57	36.61	147.49	2.59
97	750.00	30.00	4.00	0.60	426.94	34.40241	12.41	21.53	82.75	2.59
98	650.00	30.00	4.00	0.95	1102.00	214.02288	5.15	54.73	198.96	2.46
99	750.00	22.50	4.00	0.95	1153.54	259.19337	4.45	58.12	214.78	2.53
100	750.00	30.00	10.00	0.95	1605.35	228.09776	7.04	78.74	292.62	2.59
101	750.00	30.00	4.00	0.86	937.45	137.62455	6.81	48.69	185.15	2.59
102	650.00	30.00	-2.00	0.77	348.91	95.117213	3.67	18.27	68.11	2.46
103	750.00	22.50	-2.00	0.77	354.52	116.9406	3.03	18.79	70.26	2.53
104	750.00	30.00	1.00	0.77	619.56	92.220475	6.72	33.55	124.93	2.59
105	750.00	30.00	-2.00	0.60	178.40	51.849557	3.44	10.14	37.71	2.59
106	650.00	30.00	-2.00	0.95	368.19	195.5636	1.88	22.61	83.42	2.46
107	750.00	22.50	-2.00	0.95	355.24	246.6364	1.44	22.69	83.39	2.53
108	750.00	30.00	1.00	0.95	792.54	219.35498	3.61	46.06	163.65	2.59
109	750.00	30.00	-2.00	0.86	449.33	147.38519	3.05	26.09	93.75	2.59

APPENDIX E

ACCURACY ASSESSMENTS OF DIFFERENT META-MODELLING TYPES USING REFINED FCCCD

For all meta-modelling types, FCCCD is used with refinement. The accuracy assessments of different meta-modelling types are given Tables E1-E5.

Table E.1. Accuracy of refined RS created by standard RS for verification points

	Total Lift	Total Drag	Mass	Tip Deflection	Equivalent Stress
Maximum Relative Residual (Best Value = 0%)	15.3251	22.6305	0.1203	15.0477	25.0503
Root Mean Square Error (Best Value = 0)	32.3464	8.9661	0.0017	2.4454	12.0875
Relative Root Mean Square Error (Best Value = 0%)	7.5890	7.4010	0.0732	7.9799	10.2366
Relative Maximum Absolute Error (Best Value = 0%)	16.7594	39.5918	1.4999	44.5471	40.2704
Relative Average Absolute Error (Best Value = 0%)	7.0533	6.5951	0.7586	9.1938	13.0603

Table E.2. Accuracy of refined RS created by neural network for verification points

	Total Lift	Total Drag	Mass	Tip Deflection	Equivalent Stress
Maximum Relative Residual (Best Value = 0%)	9.8868	114.5189	0.1173	35.5666	13.2979
Root Mean Square Error (Best Value = 0)	24.3909	17.6752	0.0014	4.8468	9.6950
Relative Root Mean Square Error (Best Value = 0%)	4.3145	32.5787	0.0626	15.4990	6.3592
Relative Maximum Absolute Error (Best Value = 0%)	14.8135	54.7722	1.2675	89.1040	40.7208
Relative Average Absolute Error (Best Value = 0%)	5.0062	15.6540	0.5765	18.9215	9.5516

Table E.3. Accuracy of refined RS created by non-parametric regression for verification points

	Total Lift	Total Drag	Mass	Tip Deflection	Equivalent Stress
Maximum Relative Residual (Best Value = 0%)	9.0757	32.1846	1.7096	14.8051	13.9431
Root Mean Square Error (Best Value = 0)	42.5015	13.2446	0.0155	2.9957	12.0602
Relative Root Mean Square Error (Best Value = 0%)	4.8363	9.8334	0.6593	7.2758	6.5574
Relative Maximum Absolute Error (Best Value = 0%)	32.3210	56.3065	20.6762	45.7316	54.3913
Relative Average Absolute Error (Best Value = 0%)	6.6640	9.2239	5.7318	10.0707	9.8875

Table E.4. Accuracy of refined RS created by kriging for verification points

	Total Lift	Total Drag	Mass	Tip Deflection	Equivalent Stress
Maximum Relative Residual (Best Value = 0%)	4.8138	17.2040	0.0708	42.0068	12.6409
Root Mean Square Error (Best Value = 0)	13.4530	7.5691	0.0005	3.1359	8.9134
Relative Root Mean Square Error (Best Value = 0%)	2.2093	5.0082	0.0247	14.4603	6.3958
Relative Maximum Absolute Error (Best Value = 0%)	9.6000	32.1405	0.6655	58.9324	46.4546
Relative Average Absolute Error (Best Value = 0%)	2.6153	5.3826	0.1793	11.6834	8.7196

Comparison of different DOE types with refinement:

To investigate effects of selected DOE types with refinement, FCCCD, BBD, LHS and OSF DOE data are used by applying Kriging algorithm with auto-refinement option. The accuracy assessments of RS constructed on different DOE types are given Tables E5-E9.

Table E.5. Accuracy of the created RS using BBD and kriging for verification points

	Total Lift	Total Drag	Mass	Tip Deflection	Equivalent Stress
Maximum Relative Residual (Best Value = 0%)	7.4312	19.4917	0.0754	21.9901	17.6104
Root Mean Square Error (Best Value = 0)	17.3818	8.2535	0.0006	2.2897	8.9672
Relative Root Mean Square Error (Best Value = 0%)	2.8439	7.4125	0.0259	7.8097	8.2787
Relative Maximum Absolute Error (Best Value = 0%)	12.9537	37.5517	0.7338	46.5246	35.5949
Relative Average Absolute Error (Best Value = 0%)	3.4945	6.5274	0.2008	9.0546	11.3446

Table E.6. Accuracy of the created RS using LHS and kriging for verification points

	Total Lift	Total Drag	Mass	Tip Deflection	Equivalent Stress
Maximum Relative Residual (Best Value = 0%)	7.3244	10.4576	0.0919	16.8554	17.1368
Root Mean Square Error (Best Value = 0)	25.1531	3.3079	0.0009	2.2999	9.2353
Relative Root Mean Square Error (Best Value = 0%)	3.5448	4.8160	0.0391	6.7098	6.6558
Relative Maximum Absolute Error (Best Value = 0%)	22.2885	9.3889	1.1683	40.8598	36.8627
Relative Average Absolute Error (Best Value = 0%)	4.8172	3.6316	0.3337	9.0788	10.7096

Table E.7. Accuracy of the created RS using OSF and kriging for verification points

	Total Lift	Total Drag	Mass	Tip Deflection	Equivalent Stress
Maximum Relative Residual (Best Value = 0%)	7.1013	28.5815	0.1440	18.3125	10.7353
Root Mean Square Error (Best Value = 0)	23.5924	10.8604	0.0017	2.9472	10.6276
Relative Root Mean Square Error (Best Value = 0%)	3.4523	10.2867	0.0740	6.7060	6.0118
Relative Maximum Absolute Error (Best Value = 0%)	14.5820	41.7112	1.9149	63.4046	41.4410
Relative Average Absolute Error (Best Value = 0%)	4.7151	9.7751	0.6066	9.7381	10.6779

Table E.8. Accuracy of the created RS using FCCCD and kriging for verification points

	Total Lift	Total Drag	Mass	Tip Deflection	Equivalent Stress
Maximum Relative Residual (Best Value = 0%)	4.8138	17.2040	0.0708	42.0068	12.6409
Root Mean Square Error (Best Value = 0)	13.4530	7.5691	0.0005	3.1359	8.9134
Relative Root Mean Square Error (Best Value = 0%)	2.2093	5.0082	0.0247	14.4603	6.3958
Relative Maximum Absolute Error (Best Value = 0%)	9.6000	32.1405	0.6655	58.9324	46.4546
Relative Average Absolute Error (Best Value = 0%)	2.6153	5.3826	0.1793	11.6834	8.7196

Table E.9. Accuracy of the created RS using sparse grid with auto-refinement for verification points

	Total Lift	Total Drag	Mass	Tip Deflection	Equivalent Stress
Maximum Relative Residual (Best Value = 0%)	6.6765	22.1608	0.0776	12.4907	7.2878
Root Mean Square Error (Best Value = 0)	19.3037	8.3032	0.0008	1.9212	5.1924
Relative Root Mean Square Error (Best Value = 0%)	2.6287	5.4620	0.0327	3.9364	3.0511
Relative Maximum Absolute Error (Best Value = 0%)	14.4136	40.8268	1.0463	40.3030	17.7154
Relative Average Absolute Error (Best Value = 0%)	3.2985	5.0803	0.3195	5.2489	4.4162

APPENDIX F

VERIFICATION POINTS FOR MODAL ANALYSES RS

In order to assess accuracies of the RS, verification points are generated and used through the goodness of fit studies. These verification points are listed in Table F.1

Table F.1. Verification points for RS of modal analyses

Design Point #	Input Design Variables		Output Design Variables			
	Joint Location (mm)	Aft Wing Sweep (degree)	1 st Mode [Hz]	2 nd Mode [Hz]	3 rd Mode [Hz]	4 th Mode [Hz]
1	505.56	1.67	22.84	22.97	86.94	87.24
2	638.89	3.89	21.23	21.35	94.79	95.26
3	372.22	0.56	21.42	21.52	83.63	83.91
4	594.44	5.00	21.96	22.09	94.39	94.99
5	416.67	8.33	22.15	22.26	81.56	81.78
6	727.78	2.78	19.43	19.54	84.50	84.72
7	550.00	9.44	22.41	22.53	89.53	90.33
8	683.33	7.22	20.27	20.37	90.39	90.76